THESIS

THE DIURNAL CYCLE OF CONVECTION OVER THE NORTHERN SOUTH CHINA SEA DURING THE SOUTH CHINA SEA MONSOON EXPERIMENT

Submitted by

Steven Aves

Atmospheric Science Department

In partial fulfillment of the requirements

For the Degree of Master of Science

Colorado State University

Fort Collins, Colorado

Summer 2006

COLORADO STATE UNIVERSITY

MONTH DAY, 2006

WE HEREBY RECOMMEND THAT THE THESIS PREPARED UNDER OUR SUPERVISION BY STEVEN AVES ENTITLED THE DIURNAL CYCLE OF CONVECTION OVER THE NORTHERN SOUTH CHINA SEA DURING THE SOUTH CHINA SEA MONSOON EXPERIMENT BE ACCEPTED AS FULFILLING IN PART REQUIREMENTS FOR THE DIGREE OF MASTER OF SCIENCE.

Committee on Graduate Work

_____

_____

_____

Adviser

~~**Department Head/Director**~~ _____

ABSTRACT OF THESIS

THE DIURNAL CYCLE OF CONVECTION OVER THE NORTHERN SOUTH CHINA SEA DURING THE SOUTH CHINA SEA MONSOON EXPERIMENT

The diurnal cycle of convection over the northern South China Sea (SCS) during the onset of the summer monsoon is documented using satellite, radar, and sounding data from the May-June 1998 South China Sea Monsoon Experiment (SCSMEX). The onset occurred around 15 May, with significant convective activity over the SCS region over a ~30-day period.

In a general sense, an afternoon maximum of convective activity was found over the SCS region during May-June 1998. This was true considering both indirect measures, such as infrared brightness temperatures and areal cold (< 208 K) convective cloud coverage, as well as direct measures, such as radar reflectivities from the Bureau of Meteorology Research Centre (BMRC) radar data. These results are consistent with past satellite-based studies of convection over the region. Comparisons between convective activity in1998 and 2000 hint at a dependence of the diurnal cycle on the El Niño oscillation, which may act to suppress convection over the central SCS as is suggested in 1998.

Importantly, the diurnal cycle of convection over the northern SCS can only be fully explained within the context of diurnally propagating convection from the southeastern China coastline. In particular, convection initiated just offshore near sunrise and

propagated southeastward past Dongsha Island in the early afternoon, finally dissipating about 500 km offshore in the late evening. Several factors lend to the robustness of this propagation signal. It was found with analyses of both satellite and radar data, and still evident when considering subdivided periods of May-June 1998. Finally, it was even evident in 2000, a less-favorable year for convection over the northern SCS. The implied propagation speed, around 10-12 m s^{-1}, is too fast to be caused by advective or gravity current processes, so it is speculated that gravity wave dynamics may be responsible for its existence.

Steven Aves
Atmospheric Scinence Department
Colorado State University
Fort Collins, CO 80523
Summer 2006

Chapter 1: Introduction

a. Background

1) The Asian monsoon

A monsoon is, by definition, a reversal of wind with the changing of seasons (Ramage, 1971; Lau and Li 1984). The sensible weather of Southeast Asia is very much defined by the monsoon flow. During summer, a large portion of this region is under the influence of southwesterly surface winds. These winds support a relatively hot and humid climate and are responsible for the heavy rains that fall throughout the summer months. During the winter, the prevailing surface wind direction over the same region is northeasterly, emanating from a huge, persistent anticyclonic circulation over Siberia. This flow advects a cold, dry continental air mass throughout a large portion of the Asian land mass. The importance of this monsoon circulation cannot be overstated. Billions of people depend on the flow pattern and its advection of tropical moisture to bring about the "rainy season" during the peak period of agricultural production, and the extreme climate disasters in the region are dictated by the great interannual and intraseasonal variability of the monsoon itself (Ding and Liu 2001).

The onset of the East Asian monsoon is concurrent with a reversal of the temperature gradient south of the Tibetan Plateau (Flohn 1957, Yanai et al. 1992, Li and Yanai 1996). This reversal is chiefly the result of large temperature increases over the Plateau region (Li and Yanai 1996).

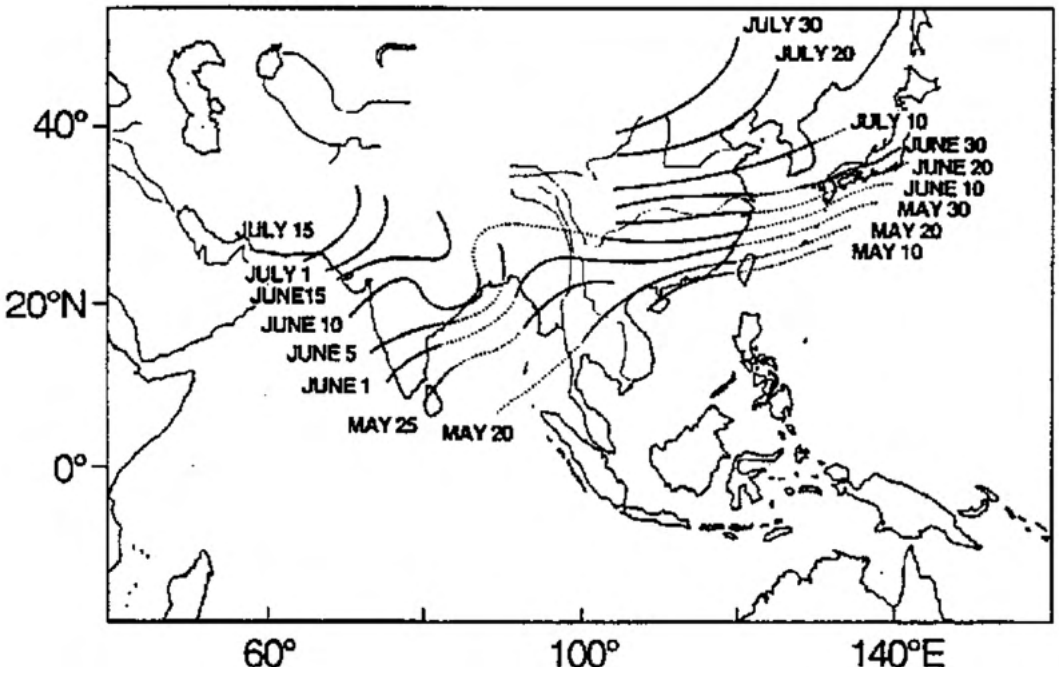

Figure 1.1 Mean onset date of the Asian summer monsoon (taken from Tao and Chen 1987).

More specifically, sensible heat flux over the semi-arid western regions of the plateau, along with latent heat release above the Himalayan Mountains are responsible for the strong tropospheric heat source that maintains the large-scale monsoon system (Lau and Li 1984). In a time-mean sense, the upward branch of the Hadley circulation is concurrent with the Tibetan heat source, with poleward low-level flow and equatorward return flow aloft. More specifically, the low-level circulation is characterized by strong cross-equatorial flows (from the southern to the northern hemisphere) near the eastern Africa coastline and the maritime continent, and southwesterly flow across southeastern Asia. This flow is driven by a monsoon low that develops in the vicinity of India and Pakistan, and by the strengthening of the semi-permanent western Pacific high-pressure system (Wai et ai. 1996, Lau et al. 2000). Meanwhile, an intense anticyclonic circulation centered over the Tibetan plateau dominates the upper tropospheric flow over the region, with divergence prevalent in the Bay of Bengal and the South China Sea.

Although the Asian summer monsoon is an annual event, it is by no means temporally regular or spatially static throughout the course of the season. As suggested earlier, there are great intraseasonal and interannual variations in the onset and maintenance of the monsoon circulation. Figure 1.1, taken from Tao and Chen (1987), depicts geographically the average date of onset for the Asian monsoon system. In a general sense, the summer monsoon begins in May, spreads north- and northwestward through the months of June and July, and starts a southward retreat in August. The earliest onset is generally accepted to occur in the South China Sea during early-mid May (Chang and Chen 1995, Johnson and Ciesielski 2002). During this time, the sea surface temperatures in the region are increasing, which results in greater potential instability for convective development. However, it is suggested that the onset is a hybrid of tropical and mid-latitude influences, as it can often be traced to a southward intrusion of cold air. The South China Sea would be the preferred location of a hybrid monsoon onset because the raised terrain of the Tibetan Plateau does not block the southward advance of cold air at these longitudes. In contrast, over the Indian subcontinent of the Bay of Bengal, it acts as a barrier that prevents midlatitude systems from reaching areas to its south. Thus, the South China Sea is the westernmost tropical region in the Southeast Asian monsoon system where lower-tropospheric midlatitude disturbances can penetrate into the subtropics (Chang and Chen 1995). Recently, Ding and Liu (2001) found evidence that a cold air intrusion was concurrent with the onset of monsoon convection over the South China Sea in 1998, further strengthening the argument of a hybrid onset.

Immediately after the onset of the monsoon over the South China Sea, heavy convective rainfall develops in a SW-NE oriented quasi-stationary frontal zone. This front is characterized by a mixture of midlatitude frontal and ITCZ-like properties, with a relatively small temperature gradient, but high moisture and equivalent potential temperature gradients and strong low-level

convergence (Lau and Li 1984, Chang and Chen 1995, Johnson et al. 1993). During this first quasi-stationary stage of the East Asian monsoon trough, the maximum band of precipitation is along and nearly parallel to the southern China coastline (Johnson et al. 1993). This location is on the north side of an eastward-retreating Western Pacific subtropical ridge in the moisture-rich southwesterly monsoon flow.

The monsoon front progresses to the north throughout the summer season, but this propagation often happens in a discontinuous fashion (Tao and Ding 1981, Ding and Liu 2001). It is typical for the front to go through three or so quasi-stationary stages, with two sudden northward surges. As the convergence zone jumps into China's Yangtze River valley in June, the front (and the time period of its residence) is referred to as "Mei-Yu" (plum rain); in Japan it is known as the "Baiu" front/period. The front jumps northward again in July to cover the Yellow River basin of northern China, the Yellow Sea, and the southern Sea of Japan. Severe flooding events can occur when the convergence zone remains stationary over a given region for too long a time, with repeated convective events depositing copious amounts of precipitation. Conversely, drought conditions occur when the band of convection doesn't remain long enough over a region, or in the case of northern latitudes, if the moist southwesterly flow doesn't penetrate northward enough during a weak monsoon year. Little is understood about the mechanisms responsible for transitions; it is possible that midlatitude influences play some part in the northward progression of the monsoon front (Chang and Chen 1995), or that some other non-linear aspect of the monsoon system causes transition into preferred "equilibrium states" (Lau and Li 1984).

2) The diurnal cycle of convection: a traditional view

In addition to the yearly seasonal solar cycle that causes monsoon circulations, earth's rotation about its axis results in another set of regular sun cycles. The basic diurnal cycle of convection can be broadly summarized as tending to follow the sun, with a lag caused by the thermal inertia of the land surface and atmospheric boundary layer. Over large land masses, the convective diurnal cycle is well understood. During the daylight hours the land surface is heated by solar insolation, which in turns heats the atmospheric boundary layer through surface fluxes and convective mixing. In the absence of other dynamical considerations, the maximum of convective activity occurs at the time of maximum boundary layer heating in the afternoon and early evening, when the vertical atmospheric column is most conditionally unstable. This fact has been proven by a number of studies using composite time series of infrared radiances measured by satellites (Yang and Slingo 2001), indices based on such infrared radiances (Hendon and Woodberry 1993, Nitta and Sekine 1994), and measures of the percent of high cloudiness (Zuidema 2003) and estimated rainfall (Lim and Suh 2000). However, there are caveats to this general rule; early morning maxima are possible over land in the presence of circulations induced by coastline proximity or topographical effects, or through the propagation of organized mesoscale convective systems (e.g. Houze et al 1981).

Similar to land masses, oceanic convection also exhibits a prominent diurnal cycle. Satellite and surface observations show a strong diurnal oscillation of precipitation in the summer hemisphere of many tropical oceanic regions (e.g. Hamilton 1981). Although the amplitudes of the oceanic diurnal convective cycle are smaller than those found over land, they are certainly not negligible. Power spectra of continuous infrared radiances often show marginally significant diurnal peaks (e.g. Hendon and Woodberry 1993), but regional measures of the areal extent of

high cloudiness show diurnal variations that are much more significant (e.g. Hall and Vonder Haar 1999).

A striking difference between the diurnal cycles of convection over land and sea can be found in the phase of the maximum of convective activity. Most global studies have found an early morning maximum of convection over ocean waters, using an array of techniques that varied widely on their direct or indirect diagnoses of convective activity. Gray and Jacobson (1977) utilized rainfall records from several tropical western Pacific islands in tandem with ship reports to show a prevalent early morning (0300-0600 local time) maximum of both rainfall accumulation and thunderstorm occurrence. The diurnal cycle was most noticeable in the heaviest rainfall intensities (rainfall rates > 25 mm h^{-1}), with a nearly 2:1 preference for early morning versus evening occurrence. Fu et al. (1990) adopted a hybrid technique involving both infrared radiance and visible light reflectance to better focus on convective cloud elements. They found an early morning maximum of the occurrence of such deep convective cloud elements in the Indonesian and Pacific regions covered in the study, with a relative amplitude of 20%-40% of the mean. Hendon and Woodberry (1993) developed an index of convective activity based on infrared radiance to illustrate that convective activity was systematically most prevalent around 0600 local time throughout all of the tropical oceanic regions. Mapes and Houze (1993) used a cloud tracking algorithm to determine the life cycle of cold convective clouds over the Pacific and Indian oceans. They found that the largest cold cloud shields tended to occur most often in the early morning hours with a 2:1 preference over the evening hours, and that this variation determined the overall diurnal cycle of cold convective cloudiness. As a final example, Janowiak et al. (1994) used coarse 3-hourly fields of the fractional occurrence of high cloudiness to show that the coldest cloud tops, in terms of infrared radiance, were most prevalent globally over open oceanic regions during the early morning hours.

This early morning maximum of oceanic convective activity, while documented by a multitude of studies, is not necessarily intuitive and in fact is still poorly understood. The argument used to explain the diurnal cycle over land cannot be precisely applied to oceanic convection, as the phase of convective activity does not correspond to the time of maximum solar and surface forcing (except for the somewhat rare circumstance of calm ocean conditions). Compounding the problem, direct measures of convective activity (i.e. rainfall accumulation) are difficult to achieve over the ocean, as only a sparse data network of island stations and ship and buoy reports is available. Studies of convection based on remote sensing techniques offer better spatial resolution, but use indirect measures of convective activity that may introduce lags or non-convective elements into the analysis (the TRMM precipitation radar is a notable exception). Perhaps most importantly, a lack of three-dimensional sensible weather observations makes the determination of the physical process controlling the oceanic convective diurnal cycle nearly impossible.

The lack of a definitive data set has led to several theories that attempt to explain the diurnal cycle of convection over open ocean waters. These theories can be subdivided according to the proposed mechanisms involved in the process.

Direct radiation-convection interactions. This mechanism was proposed at least as early as Kraus (1963), which inferred an early morning maximum of precipitation from ship reports. To explain this, Kraus (1963) speculated that during the day, the absorption of solar radiation in the upper portion of existing convective clouds heats the atmosphere at cloud-top level, which has the effect of stabilizing the layer. During the night, longwave cooling dominates the radiative balance at the cloud top level, thereby cooling and destabilizing the layer and promoting convective development. More recently, Randall et al. (1991) used a general circulation model to

simulate the diurnal cycle of precipitation. They found that executing the model with diurnally varying solar insolation produced a diurnal cycle of precipitation with an amplitude of 1 mm day^{-1} and a maximum around 0600 local time. However, when only average solar insolation was applied to the model, the diurnal cycle was greatly reduced and had the opposite phase, which was deemed to be a response to a sinusoidal divergence field forcing imparted on the model. Temperature anomalies in the simulated upper troposphere were related to the absorption of solar radiation by clouds at that level. Realizing this, Randall et al. (1991) concluded that the stabilization due to absorption of radiation by clouds tends to modulate convective development so much that radiative processes can account qualitatively for the observed oceanic diurnal cycle of precipitation.

Radiation-dynamics-convection interactions. Gray and Jacobson (1977) proposed a mechanism to explain both the early morning maximum in tropical island precipitation records, and the early morning maximum of low-level convergence indicated by the composite divergence profiles found in tropical cloud clusters. Their explanation is based on the differences between the radiation balance of the "cloudy" atmosphere (or that associated with convection) and the surrounding clear atmosphere. In their theory, the clear atmosphere surrounding organized cloudy regions adjusts to larger radiational cooling at night through extra subsidence. This accordingly increases low-level convergence into adjacent cloud regions, increasing upward motion and favoring convective development. Their theory also suggests that cirrus shields in the upper levels of cloudy regions cool more at night and less during the day than their surrounding cloud free regions. This would act in concert with lower levels to alter the vertical convergence profiles such that more moisture convergence occurs in the morning.

Thermodynamic processes. Chen and Houze (1997) contended that both of the mechanisms of Gray and Jacobson (1977) and Randall et al. (1991) required the pre-existence of large cloud

systems and did not aid in understanding the initiation and development of convective systems. In their study of convective systems in the western Pacific, Chen and Houze (1997) reported a 10:1 ratio in morning versus afternoon areal extent of the largest cold cloud clusters, with a maximum around 0400 LT. Using a tracking algorithm, they determined that these large cloud clusters tended to initiate in the afternoon, which coincided with the time of maximum solar heating. Surface data from buoys in the study region revealed an afternoon maximum in surface temperature, sea surface temperature, and equivalent potential temperature. Thus, they postulated that the diurnal cycle of convection is partially a result of the life cycle of oceanic mesoscale convective systems, which preferentially develop in the afternoon when surface conditions are most favorable, and require 6-12 hrs to reach their maximum size in the early morning hours. This mechanism is only likely to influence convective development in regions of light surface winds, as vertical mixing of the near-surface ocean waters in windy regions would reduce the effects of solar heating.

Naturally, it is possible that a combination of two or more of the above mechanisms may be operating in some circumstances.

3) The diurnal cycle of convection: regional and recent insights

While global studies of convection tend to agree on an early morning maximum of oceanic convective activity, regional studies have shown that this is not true everywhere. For example, McGarry and Reed (1978) and Reed and Jaffe (1981) discussed the convective diurnal cycle over the GATE ship array in the eastern Atlantic. They studied ship reports and percent coverage of bright cloudiness to establish an early afternoon maximum of convective activity several hundred kilometers from the West African coast. This was apparently related to the formation of

organized squall lines and their westward propagation from Africa. Over the South China Sea region of interest, recent studies have also shown an early afternoon convective maximum. Nitta and Sekine (1994) examined 9 years of infrared radiance data and found the phase of maximum convective activity was between 1000 and 1500 LT throughout the South China Sea during the summer monsoon months, but no explanation was offered. Ohsawa et al. (2001) used a more sensitive two-channel radiance technique to focus on deep convection, and discovered 75% of the sea grid points in their domain had maximum convective activity between 1100 and 1700 LT. They speculated that the early afternoon convective maximum over the sea coincided with the most favorable lower-atmospheric conditions for convective development. This argument was similar to that offered by Chen and Houze (1997), with a direct (rather than delayed) relationship between convective activity and favorable thermodynamics. Even some global studies of convection have shown an early afternoon maximum of convective activity over the South China Sea region (e.g. Yang and Slingo 2001).

When considering the diurnal cycle over the South China Sea region, it is important to consider the possible effects that adjacent land masses may have on convective development. Houze et al. (1981) provides an excellent documentation of the behavior of convection in the vicinity of Borneo in the southern South China Sea (Figure 1.2). They used satellite, radar, and pibal data to document the diurnal cycle in their coastal region. In their region, convective initiation typically occurred just off the coast around midnight, which was suggested to coincide with the commencement of an offshore low-level wind. The convection often developed into an organized MCS, reaching a maximum size around 0800 LT. After this time, the MCS propagated away from the coastline and dissipated during the day. Houze et al. (1981) hypothesized that the convective development was caused by the low-level convergence of a land breeze and the low-level monsoon flow.

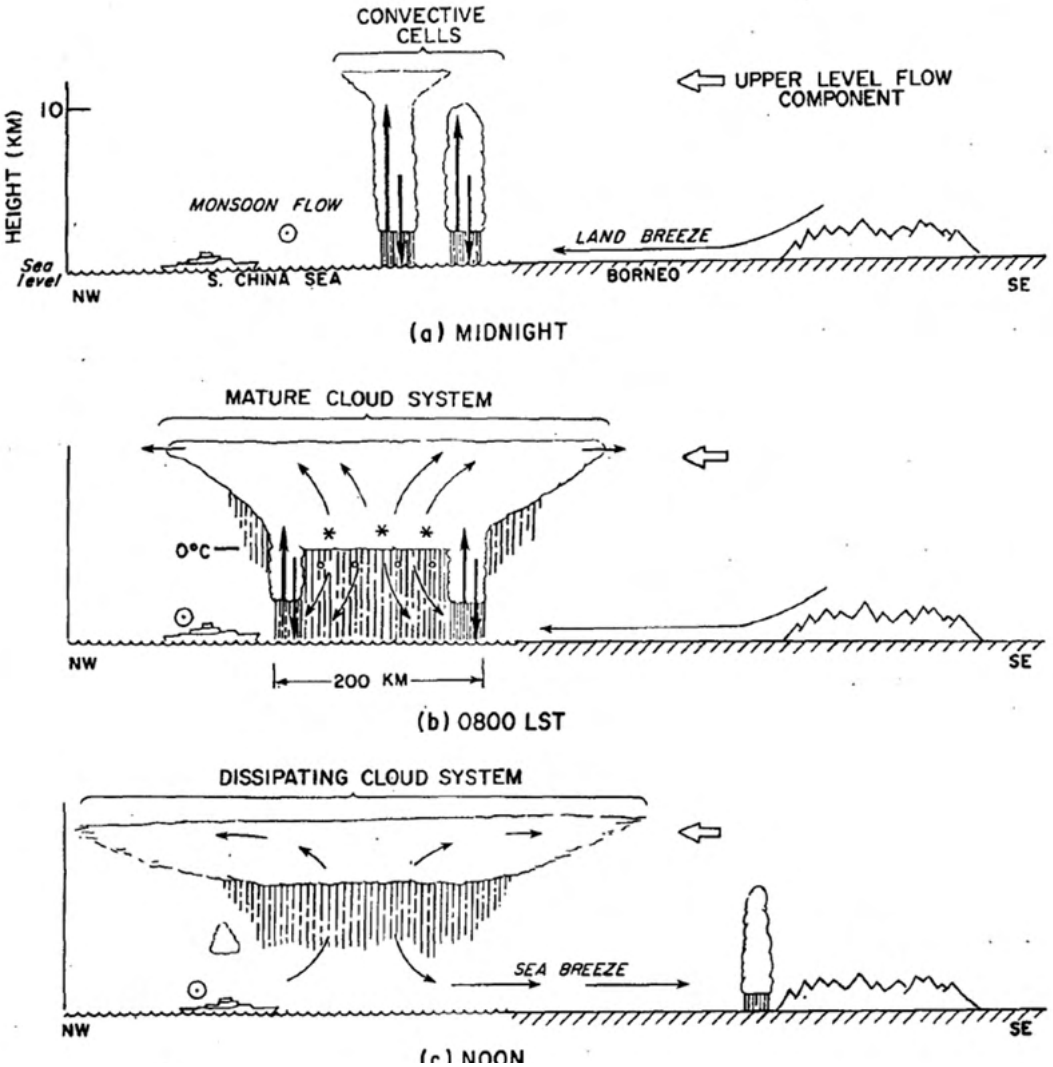

Figure 1.2 Schematic depicting the life cycle of diurnally generated convective systems off the coast of Borneo (adapted from Houze et al. 1981). It was suggested that the cloud systems initiated around midnight by the convergence between a low level land breeze and the mean monsoon flow (a). These cloud systems grew to maximum size by 0800 LT (b), and decayed later in the day as the low-level convergence ceased (c).

More recent studies of oceanic convection, aided by data with higher spatial and temporal resolution, have illuminated the possibility of a different mechanism that may affect the diurnal cycle near coastlines. Yang and Slingo (2001) highlighted the Bay of Bengal in their global study of the diurnal cycle of convection. They found an extremely coherent variation of the phase of maximum convective activity across the bay, with lines of equal phase being roughly parallel to the northeast coast of India. These phase lines spread southeastward across nearly the entire bay,

with an inferred propagation speed between 15-20 m s^{-1}. This agreed with the coherent disturbances that were observed to propagate rapidly southward over the bay during the Joint Air-Sea Monsoon Interaction Experiment (Webster et al. 2002), and it was suggested that the disturbances were responsible for the propagation signal. Yang and Slingo (2001) also commented on the parallel nature of the lines of constant phase to the coastline, speculating that the coherent diurnal variation was somehow triggered by a diurnal cycle over land; gravity waves were forwarded as a possible mechanism. Zuidema (2003) also found evidence of a propagation signal, though less extensive, emanating from the northwest portion of the Bay of Bengal when studying convective high cloudiness. The time of convective maximum increased from 0600 to 1200 LT with increasing distance from the Indian coastline. In another study, Liberti et al. (2001) focused on radiance time series to determine the diurnal cycle over the TOGA-COARE intensive flux array region. In the Papua New Guinea area, they found a phase opposition of maximum convective activity between land (afternoon) and nearby coastal waters (early morning). Additionally, a propagation signal was found to exist out to 700 km from the coast as cloud systems preferentially formed along the coastline and move seaward with increasing time. The inferred propagation speed in the Liberti et al. (2001) study was around 15 m s^{-1}, similar to that found by Yang and Slingo (2001).

One of the most compelling recent studies on the subject of convective activity near coastlines was produced by Mapes et al. (2003a, 2003b). GOES Precipitation Index data was combined with the results of numerical model simulations to examine the diurnal cycle of convection off the northwest coast of South America, in the Panama Bight. Again, a coherent variation in the phase of maximum convective activity was found over the ocean waters, with an inferred propagation speed of around 15 m s^{-1}. Mapes et al. (2003b) contended that the Houze et al. (1981) analysis is not necessarily the complete story of nocturnal convection in coastal areas. This conclusion was reached considering several factors. First, convective initiation preceded the

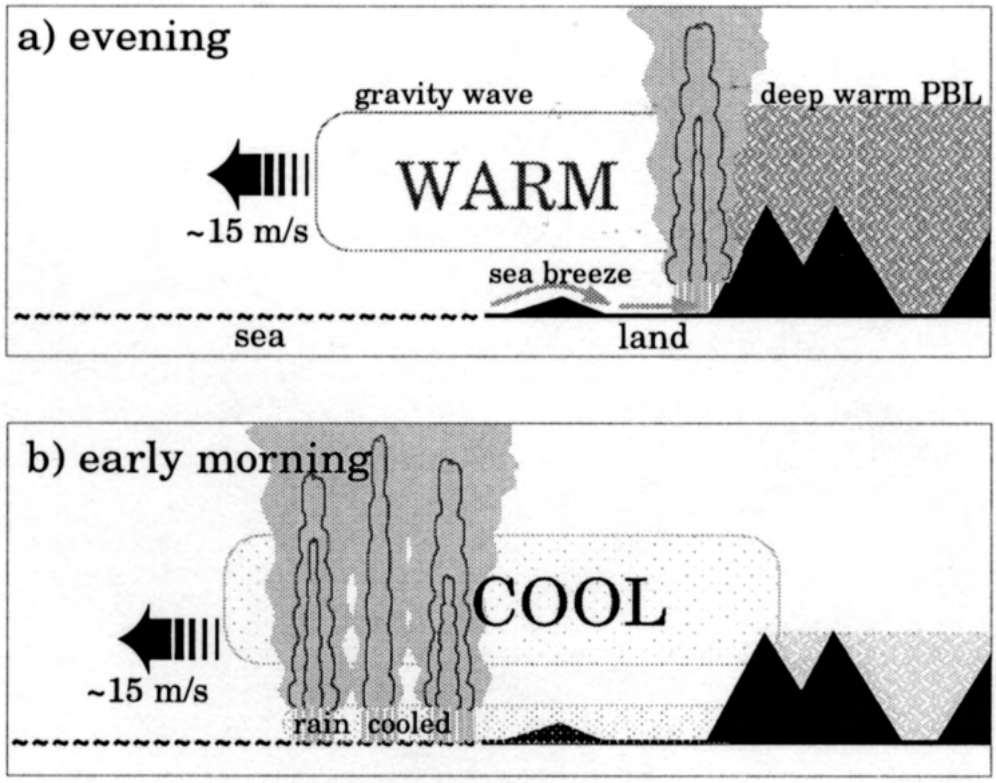

Figure 1.3 Schematic diagram representing the propagation of a thermally forced gravity wave by heating over elevated terrain. The cold anomalies caused by such gravity waves were suspected to be responsible for the initiation of offshore nocturnal convection (adapted from Mapes et al. 2003b).

commencement of off-shore wind by a few hours, so convergence couldn't have been the key player in convective development. Second, the land breeze is usually weaker than the sea breeze, but the oceanic convective response was stronger than that on land in the Houze et al. (1981) study. Finally, the land breeze and monsoon flow in the vicinity of Borneo weren't perpendicular, but rather orthogonal, and Ohsawa et al. (2001) showed that the same convective cycle exists in the Houze et al. (1981) study region even during the non-monsoon months.

Instead of the low-level convergence argument of Houze et al. (1981), Mapes et al. (2003b) advocated gravity waves as the mechanism responsible for controlling the diurnal cycle in their study region (Figure 1.3). In the model environment, variations of thermodynamic variables

seemed to be responsible for convective initiation. A diurnal cycle of buoyancy was found around the 800 mb level, which was directly related to the amount of convective inhibition in the vertical stability profile. Temperature anomalies at this level were simulated as propagating away from the elevated terrain of the nearby Andes Mountains, and the arrival of the cool phase corresponded with convective initiation. The propagation speed of the temperature anomalies was consistent with theory for a linear hydrostatic gravity wave in a resting atmosphere, whose speed is given by the vertical wavelength divided by the Brunt-Väisälä period, Doppler-shifted by the mean background flow.

b. Motivation and Problem Statement

Many motivating factors exist pertaining to the study of diurnal convection in the South China Sea region. First and foremost, although the diurnal cycle of oceanic convection has been well documented, it is still poorly understood. There are several competing hypotheses to explain the forces controlling convective processes over open ocean waters, and it has been difficult to provide evidence to prove or discredit any of them. Fully understanding the diurnal cycle of convection is an important step in understanding the role of convection in climate, so it is important to better determine what atmospheric processes could be controlling convective development.

The South China Sea Monsoon Experiment (SCSMEX, Chapter 2) provides an excellent source of data for studies of the Southeast Asian monsoon region. Additionally, it is necessary to understand the diurnal cycle of convection in the region to get a more complete picture of the multiple processes active in the monsoon system. The wealth of high-resolution satellite and atmospheric sounding data can be combined with radar observations taken from the C-band

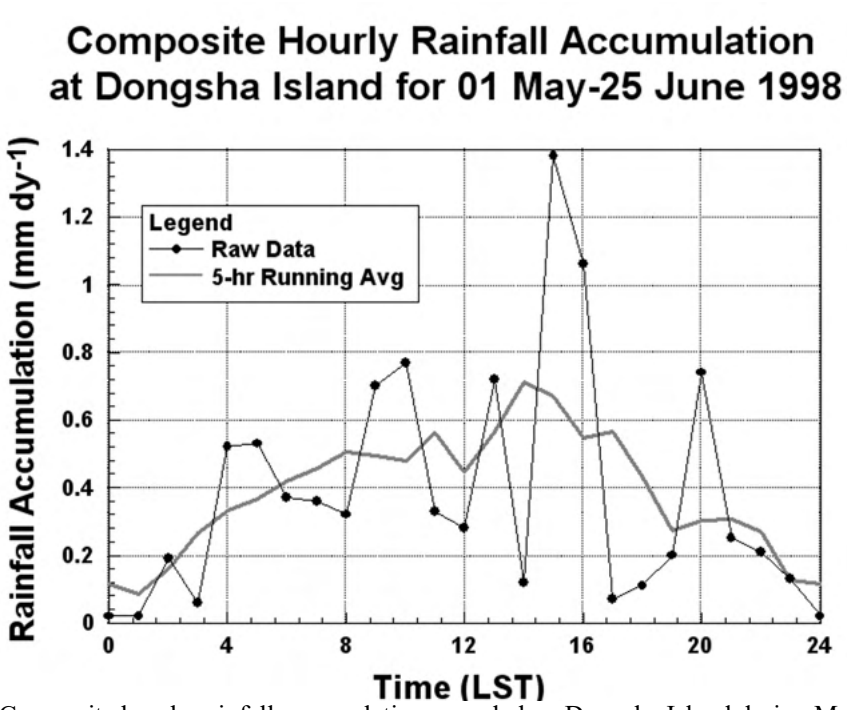

Figure 1.4 Composite hourly rainfall accumulation recorded on Dongsha Island during May and June 1998 as a function of hour of the day. Although noisy, the time series suggests a maximum of precipitation accumulation during the early afternoon hours. A 5-hr running average line is also shown to accentuate the diurnal trend.

polarimetric (C-POL, Chapter 2) Doppler radar to compare direct and indirect measures of convective activity over the South China Sea, something which has typically not been possible in previous studies. Additionally, the South China Sea region has been shown to exhibit relatively anomalous behavior in its diurnal cycle of convection as compared to open ocean regions (Nitta and Sekine 1994, Ohsawa et al. 2001, Yang and Slingo 2001). While anomalous as compared to the open ocean diurnal cycle, the behavior is typical for some of the other seas and bays in the monsoon regions (e.g. the Bay of Bengal). Study of the diurnal cycle over the South China Sea may shed light on processes which may be relevant to these other regimes.

Finally, observations of precipitation accumulation on Dongsha Island, a small island in the South China Sea located approximately 300 km southeast of Hong Kong, provided some unexpected results. Composite hourly rainfall accumulations for the period May-June 1998

(Figure 1.4), although noisy, suggest an early afternoon maximum of precipitation at this particular location. The island is presumably small enough such that it does not generate its own diurnal cycle. Thus, it was considered advantageous to determine if this precipitation observation was representative of the convective regime in the region.

Keeping these motivating factors in mind, the goal of this study is to address the following questions:

- What is the character of the diurnal cycle of convection across the South China Sea region?
- How do direct measures of convective activity (i.e. radar observations from the Dongsha Island C-POL radar) compare with more traditional indirect measures?
- Does the region, on a whole, have a convective behavior consistent with that reported by Nitta and Sekine (1994) and Ohsawa et al. (2001)?
- Is there evidence of a propagation signal along the coastline of Southeast Asia that might influence the diurnal cycle of convection over nearby coastal waters?
- What physical mechanisms seem to be responsible for controlling the diurnal cycle of convection in the region?

Chapter 2 discusses the data sets used to examine these questions, and chapter 3 details the methods that were employed in the data analysis. A discussion of the evolution of the 1998 Southeast Asian monsoon is found in chapter 4. Results of the diurnal study of convection over the South China Sea are presented in chapter 5, with a discussion of these results following in chapter 6. Also included in this study is Appendix A, which discusses in detail a new methodology that was developed to differentiate between the convective and stratiform precipitation regimes that were found in mesoscale convective systems within the radar domain.

Chapter 2: Data

a. The South China Sea Monsoon Experiment

The majority of the data used in this study was collected during the South China Sea Monsoon Experiment (SCSMEX; Lau et al. 2000). SCSMEX is an international field experiment with the purpose of understanding the key processes behind the onset and evolution of the summer monsoon over southeastern Asia and the adjacent tropical waters of the South China Sea (SCS). Figure 2.1 shows the approximate domain of the SCSMEX experiment, along with the locations of various meteorological observing elements utilized during the study. The SCSMEX network itself was contained within the larger domain of the Global Energy and Water Cycle Experiment (GEWEX) Asian Monsoon Experiment (GAME). These two projects are closely related, as they were both executed to study the processes involved with the Asian monsoon. However, the goal of SCSMEX is to study the monsoon from the perspective of air-sea interactions, while GAME focuses more on air-land surface interactions as they relate to the energy and water cycle budgets of the region (Ding and Liu 2001).

During the field phase of SCSMEX (1 May—30 June 1998), an extensive network of meteorological and oceanographic instruments was deployed in two intensive flux arrays (IFAs). The IFA in the northern SCS was centered around the dual-Doppler array composed of radars on Dongsha Island and the research vessel R/V Shiyan #3. The southern IFA surrounded the research vessel Kexue #1 in the southern SCS. These two IFAs were designed to contrast both the onset of and the properties of convection during the South East Asian Monsoon (SEAM) in

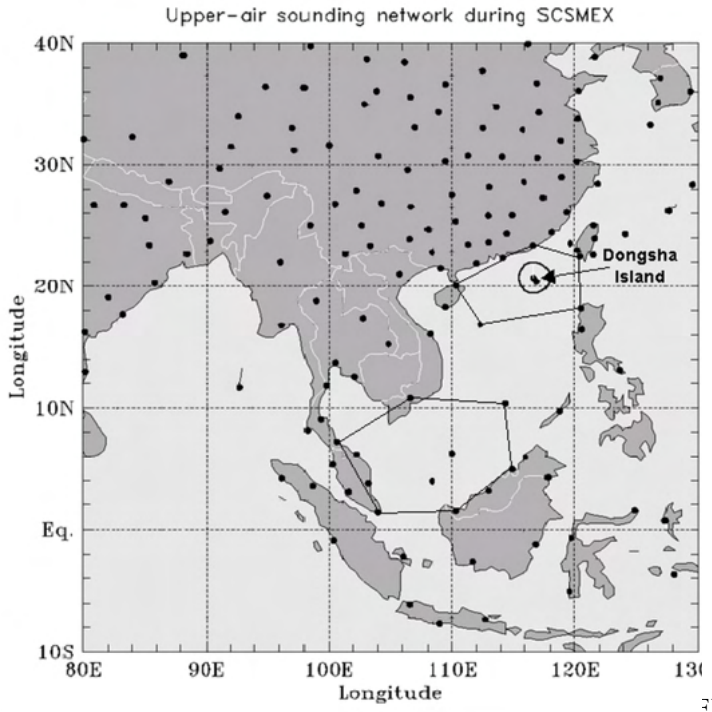

Figure 2.1 Overvie… …X experiment. The domain of the BMRC C-POL Doppler radar, located on Dongsha Island (20.70ºN, 116.72ºE), is depicted by the black circle. The northern and southern IFAs are bounded by thin solid lines.

two distinct tropical oceanic regions. In order to characterize the temporal changes in the SEAM system, two intensive operation periods (IOPs) were conducted during the field phase of SCSMEX. The first IOP (5-25 May) focused on monitoring the onset of the SEAM in terms of the sudden seasonal transition and its effect on precipitation associated with the monsoon trough over the SCS region. The second IOP (5-25 June) focused on monitoring conditions over the SCS during the mature phase and northward migration of the Asian monsoon.

b. Satellite data

The satellite data utilized in this study were collected by the fifth generation of the Geostationary Meteorological Satellite (GMS-5). Operated by the Meteorological Satellite

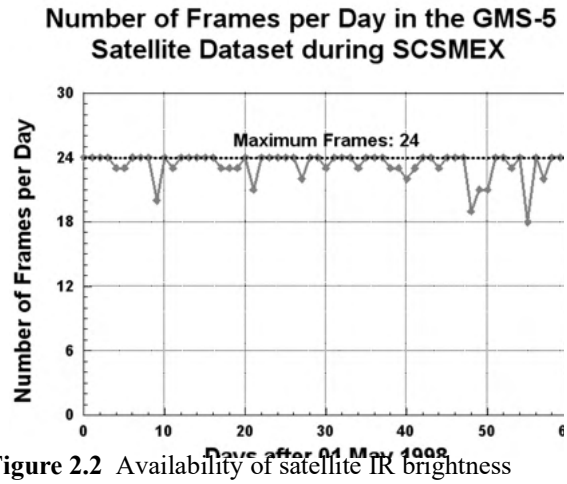

Figure 2.2 Availability of satellite IR brightness temperature frames by day for the period 1 May-30 June 1998. In general, the data set was relatively continuous with the exception of late June.

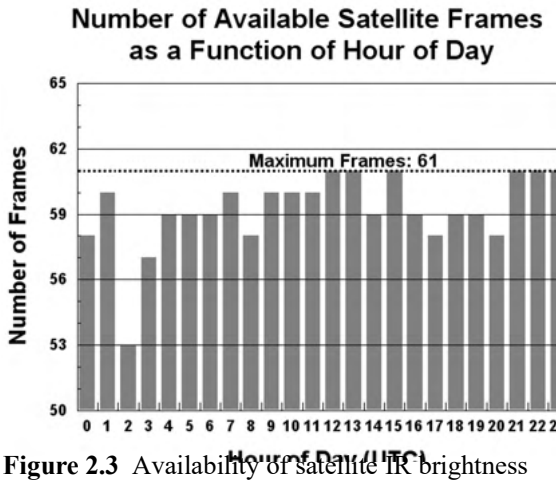

Figure 2.3 Availability of satellite IR brightness temperature frames, as a function of the hour of day, for the period 1 May-30 June 1998. The 0200 UTC hour had the most missing frames; because of this fact, the 0200 UTC hour was sometimes interpolated for the purpose of composite analysis.

Center of the Japan Meteorological Agency, this satellite was located directly above 140ºE longitude during SCSMEX. The provided data sets consist of brightness temperatures of emissions in the infrared spectral band centered on 11μm. This data extended over the range of 70º-160ºE longitude and 20ºS-70ºN latitude, but for the sake of storage space this domain was truncated to 90º-140ºE, 10ºS-40ºN to focus on the region surrounding the South China Sea. Spatial resolution of the infrared imager is 5 km, but the data were geometrically corrected to grid with a constant spacing of 0.05º latitude by 0.05º longitude. The data set has a temporal resolution of 1 h, and extends from 1 May to 30 June 1998.

Figure 2.2 depicts the temporal continuity of the satellite data set, in terms of the number of available satellite frames for each day in the period 1 May-30 June 1998. Approximately 64% of the days in the period have a complete record of satellite information, and most of the other days have only one or two hourly images that were missing or contaminated. A notable exception to this rule exists towards the end of June, when up to a quarter of the daily satellite frames per day

are missing. However, most of the satellite analyses will be focused on the period 15 May –14 June, as this was the period when the most convection existed over the South China Sea region. Figure 2.3 sheds light on the validity of satellite composite analyses by considering the number of available satellite frames as a function of the hour of day. For some undocumented reason, the 0200 UTC hour has the largest number of missing frames, and it was found that during the convectively active period 18-22 May this hour was missing 4 out of 5 times. Because of this fact, the missing 0200 UTC frames are sometimes interpolated, using the frames adjacent in time, to better capture the essence of the diurnal cycle.

c. Radar data

1) Description of the data set

The radar data utilized in this study were collected using the Bureau of Meteorological Research Center's (BMRC) C-band polarimetric (C-POL) Doppler radar, which was centered on Dongsha Island (20.70ºN, 116.72ºE) during SCSMEX. Table 2.1 shows a list of the C-POL radar attributes, including the location, physical characteristics, scanning strategy, and types of variables recorded by the radar. The received data had been interpolated to a Cartesian grid with a horizontal and vertical grid point spacing of 2 and 0.5 km, respectively. Because of size constraints, the radar grid was limited to a size of 127 x 127 grid points; consequently, data along the cardinal directions only extended out to a maximum of 126 km from the radar origin. The received data sets included volumes of both raw and corrected reflectivities (Bringi et al., 2001), and estimated rainfall rates. Reflectivity data were corrected using a scheme based on the polarimetric differential propagation phase measurements, which are insensitive to ice and have a linear relationship with attenuation at typical radar frequencies. Rainfall estimates were obtained using a variety of methods; however, the algorithm based on specific differential phase, which is

Attribute	Value
Radar location	20º42'11"N 116º43'14"E
Altitude	10 m MSL
Peak output power	250 kW
Operating frequency	5605 MHz
Pulse width	1.0 μs
Pulse repetition frequency	1000 Hz
Antenna gain	45 dB
Beam width	1.0º
Maximum range	300 km
Minimum range	1 km
Range resolution	300 m
Scan rate	10.5º s^{-1}
Volume scan frequency	~600 s
Tilt angles (deg.)	0.5, 1.3, 2, 2.8, 3.9, 4.9, 6.2, 7.5, 9.1, 11.1, 13.5, 16.4, 19.9, 24.1, 29.2
Polarization	Linear Horizontal and Vertical
Variables recorded	Z_H, $Z_{Hcorrected}$, V_R, σ_v, Z_{DR}, Φ_{DP}, ρ_{hv}

Table 2.1 Operational characteristics of the BMRC C-POL Doppler radar during SCSMEX.

nearly linearly correlated with rain rate, and differential reflectivity, which yields information about the drop size distribution, was preferred for this study.

The data record from the C-POL radar has a temporal resolution of 10 minutes and extends from 15 May through 27 May, and again from 8 June through 24. May 26-27 and 8-9 June have a large number of missing data and will not be included in the analysis. Additionally, little convection occurred after 9 June, making the entire June dataset relatively useless for the analysis of convection. Therefore, this study will focus on the convection that existed in the radar domain between 15 and 25 May. Figure 2.4 shows the continuity of the data record for this period, in terms of the number of available radar scans for each consecutive 3-h period. The dataset is relatively continuous throughout the period with 16 May being the most notable exception. On this day, the horizontal transmitter/receiver cell was diagnosed as being faulty, and its repair resulted in a two-hour data gap. To diagnose the validity of diurnal composites of radar variables,

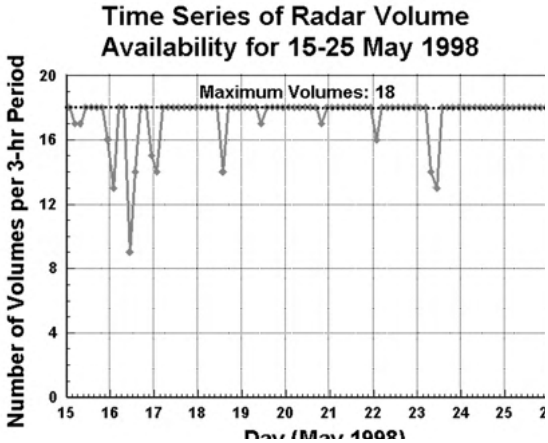

Figure 2.4 Availability of radar volume scan data for the period 15-25 May 1998. The number of volume scans for each 3 hour period is displayed in the graph above, and each period can contain a maximum of 18 volume scans.

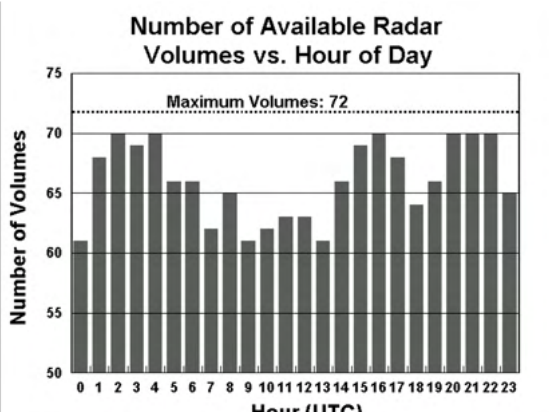

Figure 2.5 Availability of radar volume scan data as a function of the hour of day. This graph is useful in assessing the quality of composite analyses that attempt to diagnose the diurnal cycle of radar echoes.

Figure 2.5 shows the distribution of available data volumes as a function of the hour of day. The missing radar volumes (8.3% of total) were fairly well distributed across all hours such that no interpolation was necessary.

2) Quality control of the corrected reflectivity field

The radar reflectivity data obtained from the BMRC had already been quality controlled to remove spurious echoes from anomalous propagation and ground clutter. Subjective visual inspection of radar volumes confirmed this fact, as there were very few fields that contained non-meteorological echo. However, there were some spurious echoes that were always among the data points closest to the radar origin. These echoes were obviously non-meteorological in nature, with reflectivity values exceeding 100 dBZ at times. In corresponding with BMRC, it was determined that these echoes were the artifacts of a misapplication of the Bringi et al. (2001) reflectivity correction algorithm. Unfortunately, the people at BMRC were not able to resolve the

issue, and the correction algorithm was meant to be applied to reflectivity data in polar format only. Thus, a quality control procedure was developed to remove these spurious echoes from the data on the available Cartesian grid. The procedure was based on the fact that attenuation of a radar beam increases monotonically from the radar origin, as beams of electromagnetic radiation are increasingly absorbed and scattered by hydrometeors (e.g. Bringi et al. 2001). In this manner, the difference between the corrected and raw reflectivity fields should be zero at the radar origin, and ever increasing, in the presence of precipitation, with increasing distance from the origin. Any strong deviation from this profile would indicate erroneous data, and is supplemented with the raw, uncontaminated radar reflectivity field using the following procedure.

The algorithm begins by creating a difference field between the corrected and raw reflectivity fields at a given vertical level. Any data points for which raw data exist, but corrected data does not, are flagged for future analysis. The algorithm then flags data points in the difference field within 30 km of the radar origin if the difference between corrected and raw reflectivity exceeds the threshold value of 40 dB. The radius of 30 km was determined visually to encompass the area in which erroneous data points were found to exist, and the threshold value of 40 dB was chosen subjectively using the frequency distribution of the complete set of difference field values within said radius. Once the erroneous or missing data points have been flagged, the points are then ordered from most to least distant from the radar origin. This ordering helps to ensure that useful data, which can be used to recalculate the corrected reflectivity of the flagged points, will exist in at least some of the immediately neighboring data points. For each flagged data point, the average distance and reflectivity difference are calculated for the available neighboring data points within a radius of one grid point. The reflectivity difference of the flagged data point is then linearly interpolated using the calculated averages, the distance of the flagged point from the origin, and the assumption that the reflectivity difference should be zero at the radar origin. Finally, the corrected reflectivity at the flagged data point is taken to be the sum of the raw

reflectivity and the linearly interpolated reflectivity difference. This procedure is repeated for all flagged data points, and all vertical levels in the volume data. In this manner, contaminated or missing data are not simply thrown out, but estimated using raw data and assumptions that are valid locally and for small values of reflectivity difference.

d. Meteorological Data

In order to get an average sense of the larger-scale patterns responsible for convective development during the period of interest, it was beneficial to consider the fields of meteorological variables obtained during SCSMEX. During the experiment, sounding data collected from 162 sites in the SCSMEX/GAME domain. These soundings were visually inspected up to 100 hPa for the purpose of quality control (Johnson and Ciesielski 2002). From this sounding data, gridded data sets of horizontal wind components, temperature, specific humidity, and geopotential height were created using the multiquadric interpolation scheme of Nuss and Titley (1994). Data sets had a grid spacing of 1ºx1º, a vertical resolution of 25 mb, a vertical extent of 1000-25 mb, and a horizontal extent covering 80-130ºE, 10ºS-40ºN. Analyses were available at 00, 06, 12, and 18 UTC for the period 1 May-30 June 1998. Over the oceanic data-void regions in the domain, gaps with no data within 3º of a 5º grid intersection were assigned GAME Reanalysis values (Yamazaki et al. 2000). This had minimal impact over the South China Sea region, but was essential over the Bay of Bengal and western Pacific regions. Additionally, GAME Reanalysis winds were substituted for the measured winds below 700 mb in the region of the Laong station in the Philippines because of topographical affects that created spurious divergence in the gridded analyses (Johnson and Ciesielski 2002).

Chapter 3: Methodology

The study of the diurnal cycle requires high-resolution data, both temporally and spatially, to adequately describe the phasing and propagation of signals under investigation. Fortunately, this study utilizes a dataset of high-resolution satellite brightness temperatures, with a temporal resolution of one hour and a spatial resolution of 1/20 degree, which extends over the entire domain and is nearly complete for the time period under consideration. However, the radar data available for this study cover a very limited area of the domain, and the record is incomplete for many days. Additionally, meteorological soundings were only regularly performed every six hours during SCSMEX, and the coarse spatial resolution of observation points allows for little more than synoptic-scale inferences with any degree of accuracy. Realizing this limitation, several different methodologies were employed for each type of available data. Doing so will result in both the extraction of as much information from existing datasets as possible, and the increase of the significance of results that are in agreement with each other. Attempts were also made to demonstrate the suitability of satellite data, and its indirect description of convective activity, in describing the diurnal cycle of convection when more direct observations are unavailable. In this manner, the satellite dataset, which is the only complete and detailed record available, can be proven to adequately describe the diurnal cycle of convection for all places and times of interest to this study.

The satellite section of this methodology chapter first provides justification for various indices and thresholds, based on infrared radiance, that are used through the remainder of this study. Following this are discussions of the three main methods that are employed to examine the

diurnal cycle of convective activity: composite analysis, which determines the amplitude and phase of the diurnal cycle at an arbitrary point; time cluster analysis, which tracks the contiguous cold cloud shields of mesoscale convective systems through their life cycle; and the evolution histogram, which succinctly shows the diurnal cycle of cloudiness at all heights on the same diagram. The radar section of this chapter describes the methods used to determine the existence of a bright band signature in a vertical reflectivity profile, and the "bright band fraction" for an arbitrary point in the radar domain. Finally, a fixed vertical level is defined as the working level of horizontal reflectivity, on which a majority of convective classification calculations are made.

a. Satellite Methodologies

1) Indices and thresholds

As mentioned earlier, satellite-derived infrared brightness temperatures are the basis for examining deep convection in this study. Unfortunately, visible reflectance information was not available for this study. This introduces an ambiguity, as deep convective cloud cover can have approximately the same presentation in infrared wavelengths as other high cloud cover not related to deep convection. However, Fu et al. (1990) demonstrated that high clouds fall into two distinct populations based on their visible reflectance and infrared brightness temperature, and that these two populations could be discerned using a simple brightness temperature threshold. Deep convective cloud cover was generally found to have a reflectance ≥ 0.5 and a brightness temperature ≤ 230 K, where cirrus and anvil cover was duller (reflectance < 0.5) and warmer (brightness temperature > 230 K). Other authors (e.g. Hendon and Woodberry, 1993; Yang and Slingo, 2001) have taken advantage of this separation in populations by utilizing the 230 K threshold in their studies of deep tropical convection.

Hendon and Woodberry (1993) used the result of Fu et al. (1990) to construct an index of deep convective activity (DCA) based on satellite infrared brightness temperatures. The DCA index is discontinuous, and only has a value with brightness temperatures lower than 230 K. Mathematically, it can be expressed as

$$DCA = \begin{cases} a*(230 - T) & T \le 230\ K \\ 0 & T > 230\ K \end{cases} \tag{3.1}$$

where T is the brightness temperature in Kelvins. Thus, Hendon and Woodberry (1993) assume a linear weight for infrared brightness temperatures lower than 230 K, which is scaled into physical units by the coefficient a. To quantify a, Hendon and Woodberry (1993) utilized the results of Janowiak and Arkin (1991), who also used a satellite infrared brightness temperature technique to estimate tropical rainfall over the years 1986-1989. The zonal means of estimated rainfall (4 mm d^{-1}) and DCA (0.57 units) calculated by Janowiak and Arkin (1991) were assumed to be representative of the entire area of study of Hendon and Woodberry (1993), and the resulting factor of a (0.29 mm hr^{-1} (unit DCA)$^{-1}$) was assumed to hold locally as well as instantaneously. Yang and Slingo (2001) utilized the DCA index in their study of the diurnal cycle in the tropics, and they incorporated the same values of a and threshold brightness temperature without further explanation. Ricciardulli and Garcia (2000), Riccardulli and Sardeshmukh (2002), and Horinouchi (2002) also used the DCA index in their studies of tropical deep convection, with a slightly modified brightness temperature threshold (240 K). It is interesting (as well as suspicious) that a satellite index of deep convective activity should be based on rainfall data that were themselves estimated by satellite brightness temperatures, and that the linear relationship assumed by the index was never physically justified or shown to coincide with observations, so the index must be further scrutinized before its implementation in this scientific study.

In an attempt to better grasp the physical basis of the DCA index, infrared brightness temperatures were compared to C-POL radar-estimated rainfall rates at individual points and times where both datasets coexisted. This result should be more robust, as radars provide a direct measurement of hydrometeors in deep convective clouds, whereas IR brightness temperatures are only indirectly related to precipitation through the assumption that cold clouds are deep and thus precipitate. In making the comparison, only radar frames from the top of each hour (e.g. 0000 UTC, 0100 UTC) were included to best match with satellite IR brightness temperature retrieval times. Additionally, radar and satellite data points had to be within 1 km of each other to be considered the same point in space and included in the comparison. No geometric correction to best correlate the datasets is included, as only qualitative results are desired for this particular discussion. Only the days 15-20 May, and only the data points within the 142 km radius domain of the Dongsha Island C-POL radar are included in this comparison. While the temporal and spatial extent of this comparison is admittedly limited, the number of observations meeting the above criteria (77805) should be adequate to discern the utility of the DCA index within the context of this study.

Figure 3.1 examines the appropriateness of a linear relationship between satellite IR brightness temperatures and radar-estimated rainfall rates as dictated by the DCA index. In constructing this graph, estimated precipitation data were binned according to the corresponding brightness temperature of each data point (in 5 K bins). Radar data were areally averaged to match the approximate resolution (~5 km) of the satellite data. Statistics were then calculated for each brightness temperature bin to obtain the average and standard deviation of radar-estimated precipitation as a function of brightness temperature. In the range of non-zero DCA values, Fig. 3.1 shows that a linear relationship between DCA and precipitation is consistent with observations, as the average precipitation for each bin increases monotonically and approximately

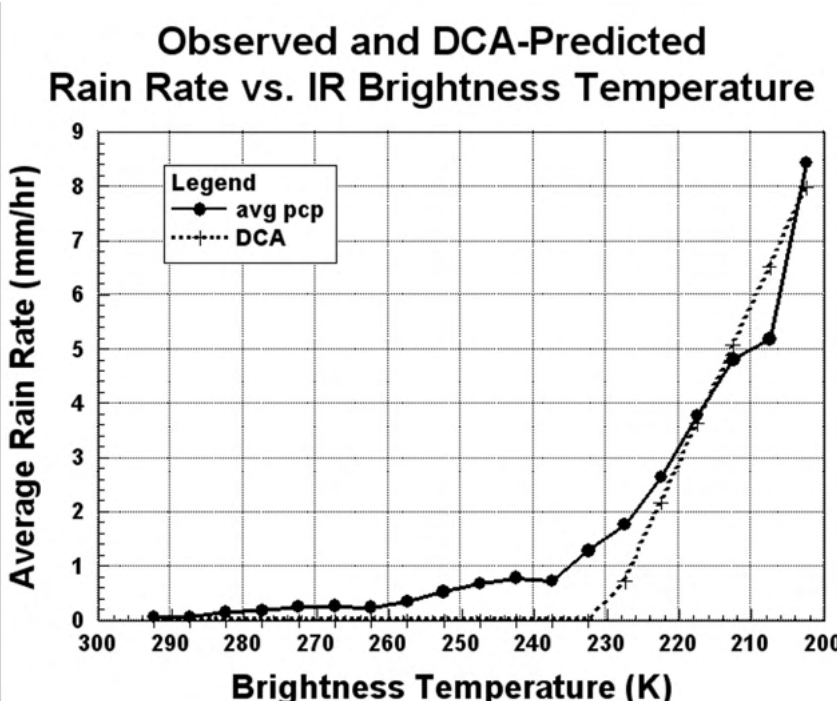

Figure 3.1 Average rain rate versus IR brightness temperature, as calculated from observations and as predicted by the DCA function (Equation 3.1).

linearly with decreasing brightness temperature. Further, Fig. 3.1 shows that the rainfall estimated by the DCA index, as calculated by equation 3.1, matches well with the average radar-estimated precipitation for IR brightness temperature bins colder than 230 K. In fact, time-integrated rainfall accumulations for 15-20 May estimated by the DCA index, and by those radar observations whose corresponding brightness temperatures are ≤ 230 K, agree to within 10%. These factors demonstrate the ability of the DCA index to accurately represent the physical contributions of deep convection in a time-integrated sense.

Caution must be exercised in directly equating DCA and precipitation, however. It is easy to show that the DCA index cannot be used to estimate instantaneous values of precipitation, as cloud-top brightness temperatures are rarely cooler than 180 K, which by Eq. 3.1 would yield a maximum precipitation rate of 14.5 mm hr^{-1}. This precipitation rate is routinely exceeded in tropical deep convection (Yuter and Houze 1997); therefore, the DCA index cannot diagnose

intense precipitation. Additionally, the DCA index did not appropriately estimate the total precipitation over the 15-20 May comparison period, as approximately 40% of the rainfall was associated with clouds whose brightness temperatures were greater than 230 K. The DCA index was incapable of capturing this precipitation, and it did not adequately compensate by overestimating the contribution of clouds with colder tops. Realizing these limitations, the DCA will be used conservatively to focus on the temporal variability of deep convective clouds without assuming a strict relationship to instantaneous precipitation rates or total accumulated precipitation.

In addition to the DCA index, two brightness temperature thresholds will be utilized throughout this study to help isolate the phenomena of deep convection. Mapes and Houze (1993) present a brief review of some of the multitude of thresholds that have been used in literature, along with a physical justification for their various applications. To study deep convection, Mapes and Houze (1993) chose a brightness temperature threshold of 208 K, which they justified through a subjective impression of correspondence to radar echo patterns observed in mature oceanic mesoscale systems during the Equatorial Mesoscale Experiment (EMEX, Webster and Houze 1991). Subsequent studies (e.g. Chen et al. 1996, Chen and Houze 1997, Hall and Vonder Haar 1999) also used this 208 K threshold to scrutinize tropical deep convection, because it is a "closer approximation to the boundary of the precipitating core" and a "conservative indicator of precipitating deep convection" (Chen et al. 1996). These assertions are confirmed by comparing the radar and satellite data used in this study, as it can be shown that the coldest cloud tops, as compared to warmer clouds, are most often associated with both general precipitation and precipitation rates typically generated only through convective processes ($\geq$10 mm hr^{-1}; Rosenfeld et al. 1995, Steiner et al. 1995). These factors provide confidence in implementing 208 K as an indicator of deep tropical convection. The second threshold, 235 K, can be dated back to Arkin (1979) and was chosen because it provided an optimum linear

regression with GATE [GARP (Global Atmospheric Research Program) Atlantic Tropical Experiment] rainfall. The threshold was retained in rainfall estimates by Arkin and Mesiner (1987) and Janowiak and Arkin (1991), and has since been used in a multitude of satellite-based convective studies (e.g. Mapes and Houze 1993, Chen and Houze 1997, Garreaud and Wallace 1997, Liberti et al. 2001, Zuidema 2003).

2) Composite analysis

The technique of composite analysis was employed to best isolate the diurnal cycle, in terms of both its amplitude and phase, from the available time series of data. Composite analysis is based on the *a priori* expectations that a diurnal cycle exists, and that events such as the development, passage, and dissipation of convective systems generally occur at the same time and place each day. The validity of the first expectation is simple to prove, either through previous studies of oceanic tropical convection (e.g. Gray and Jacobson, 1977; Mapes and Houze, 1993; Yang and Slingo, 2001; Ohsawa et al. 2001), or through spectral analysis of a proxy variable for convective activity. Following Hall and Vonder Haar (1999), a spectral analysis of the areal extent of deep convective cloudiness is presented in Figure 3.2. To calculate the power spectrum in Fig 3.2, a time series of areal cold cloud coverage (< 208 K) was created for the South China Sea basin between 10º and 25ºN, and 110º and 120ºE. This time series was 61 days long, covering the entire May-June 1998 satellite dataset. The few gaps in the dataset were filled through linear interpolation. In order to increase the number of spectral estimates, the time series was divided in half, and a Fast Fourier Transform algorithm was executed on both halves. The power spectra from each execution were averaged, and then smoothed, to yield 12 degrees of freedom. For the purpose of statistical significance, it is conservatively assumed that the accompanying red noise spectrum has 12 degrees of freedom as well. Fig. 3.2 shows that there is

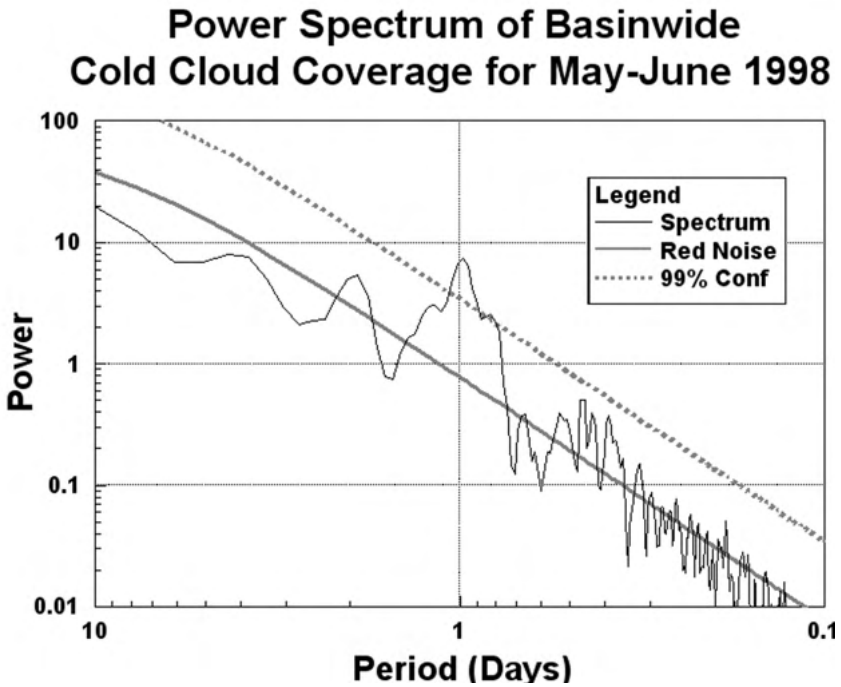

Figure 3.2 Power spectrum of the areal cold (< 208 K) cloud coverage time series for the SCS region (10º-25ºN, 110º-120ºE) during the period 01 May – 30 June 1998. Also shown are the accompanying red noise power spectrum and the 99% statistical confidence demarcation.

power in the frequencies with periods of two, one, and half- days that exceeds the red noise background. However, only the diurnal variation is statistically significant at the 99% confidence level, proving that the amount of convective cloudiness does vary significantly on a diurnal timescale.

Validation of the second expectation is more subjective, but is still easy to prove by examining loops of contiguous satellite frames. Analysis of satellite loops revealed several such instances of convection that formed near or along the coast of southeastern China and propagated away from the coast with time. Since both expectations have been shown to apply to the region of study, it follows that composite analysis should be an effective tool for extracting the diurnal cycle from other frequencies of variation present in the data time series.

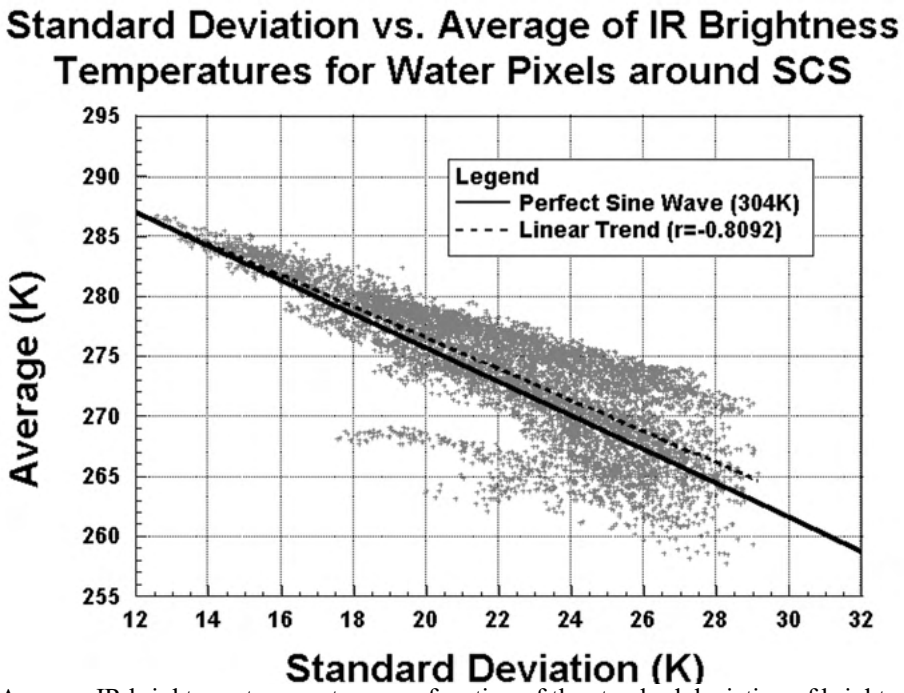

Figure 3.3 Average IR brightness temperature as a function of the standard deviation of brightness temperature for water pixels in the SCS domain (10º-25ºN, 110º-120ºE). Only the MYJN period (15 May-14 June 1998) was considered in this analysis.

Through composite analysis, the goal is to arrive at a composite 24-hour time series that is representative of the diurnal variations of the variable under consideration. To achieve this goal, a time series of some variable (e.g. IR brightness temperature) is considered at an individual point in space. For each hour in the composite series, the data from all similar hours in the variable time series are averaged together to arrive at a composite value for that hour. That is, all 0000 UTC values are summed, and that total divided by the number of days in which the 0000 UTC data exists, in order to arrive at a composite 0000 UTC value. This procedure is repeated for all 24 hours to take advantage of the one-hour resolution of the data. In this fashion, the resulting 24-hr composite time series is assumed to reflect the average state of the variable under consideration for a given location as a function of the time of day. This procedure can be repeated for various points in space to generate a composite two-dimensional map for a given hour.

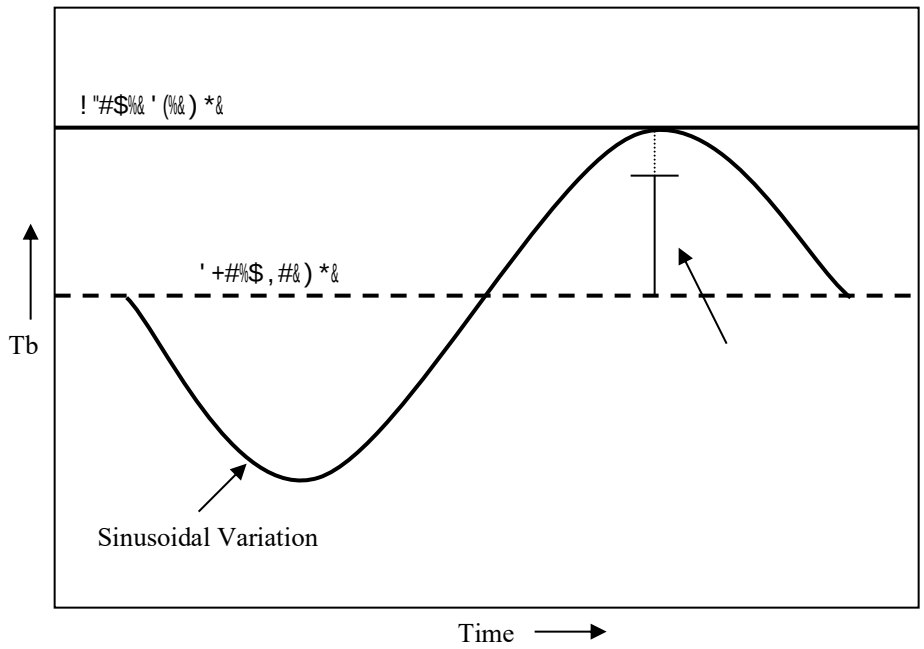

Figure 3.4 Schematic diagram relating the terms used in composite analysis. The clear air brightness temperature is assumed to be the maximum brightness temperature in the absence of cloudiness, representative of near-surface thermal emissions. The sinusoidal variation used to model the diurnal cycle of cloudiness moves about the average brightness temperature, has a standard deviation proportional to its amplitude, and theoretically touches the clear air brightness temperature line at its maximum.

To assess the phase of the diurnal cycle, the 24-hr composite time series is regressed against a sinusoidal variation with a period of one day. This introduces the assumption that variations in the variables under consideration are approximately sinusoidal in nature, but this can be shown to be a reasonable expectation. Figure 3.3 tests the validity of this assumption by comparing the average and standard deviation of brightness temperatures for pixels over ocean waters within the northern SCS domain (10-25N, 110-120E) during the period 15 May-14 June 1998 (hereafter known as the MYJN period). To interpret this graph, the statistical characteristics of the average and standard deviation operators must be considered in relation to the physical limitations governing the data. First, the IR brightness temperature of ocean surface emissions changes very little both diurnally and throughout the period under consideration. This can be related to the small diurnal amplitude of sea surface skin and near surface air temperatures as reported in Chen and Houze (1997), since in the absence of clouds there would be little in an atmospheric column

that would modify the amount of upwelling longwave radiation from its surface emission. Additionally, the sea surface temperatures over the region fluctuated only slightly through the MYJN period (Johnson and Ciesielski 2002). These two facts allow the surface IR emission to be assumed constant with little error. The second step in the analysis process is to assume that a diurnal cycle consists of cloudy and cloud-free periods, such that the maximum brightness temperature of IR emission will be equal to the surface emission value. With this being true, the amplitude of a sinusoidal variation will simply be the difference between the average brightness temperature and the surface brightness temperature, as shown in Figure 3.4. The standard deviation of the sinusoidal variation will be proportional to the amplitude of the variation, which can be shown analytically to be

$$\sigma = \sqrt{\frac{1}{2\pi}\int_0^{2\pi}\left[A\cos(x)\right]^2 dx} = A\frac{\sqrt{2}}{2}, \tag{3.2}$$

where the continuous formulation of variance is utilized, σ is the standard deviation of the sinusoidal variation, and A is the amplitude of the variation. Thus, if only sinusoidal variations of similar amplitude and period exist in the data series, the difference between the average brightness temperature of the time series and the clear-air brightness temperature should be 1.414 times the standard deviation of the time series. Smaller variations around the mean will yield a higher amplitude/standard deviation ratio, due to a reduced variance of the time series. Conversely, sporadic, large-amplitude variations superimposed over a clear-air emission time series will yield an amplitude/standard deviation ratio of unity or less. With this information, the ability of a sinusoidal variation to capture the variance of the time series can be determined, as in Fig. 3.3.

Figure 3.3 shows the relationship between the amplitude and standard deviation of IR brightness temperature time series for water pixels in the northern SCS domain. The amplitude is expressed as the difference between the sea surface temperature and the average IR brightness temperature for a given location. It is evident that amplitude and standard deviation are well correlated, as the linear correlation coefficient for the least-squares regression is very significant ($r=0.8734$). The slope of the relationship (1.36) is very close to the derived ratio for a sinusoidal variation (1.41), and this would indicate that such a variation would be appropriate to capture the essence of the variance in IR brightness temperature time series. Visual inspection of time series emphasizes this point, as variations are generally sinusoidal in nature, especially in composite time series (see, for example, Figure 5.1). Other advantages to using a sinusoidal variation include the extensive use in literature (e.g. Hendon and Woodberry 1993, Yang and Slingo 2001, Liberti et al. 2001), and the continuous and periodic nature of the function, which coincides with the basis of a diurnal cycle and facilitates the calculation of its distinguishing parameters, namely phase and amplitude. Considering its appropriateness, robustness, and simplicity of use, a sinusoidal variation will be used to describe characteristics of diurnal cycles without further reservation.

The phase of the diurnal cycle was found by maximizing the linear correlation coefficient between the 24 h composite time series and a sinusoidal variation with a period of one day, in a manner similar to Liberti et al. (2001). The linear correlation coefficient is defined as the covariance between the time series of data and the sinusoidal variation divided by their standard deviations, and can be expressed as

$$r = \frac{\overline{[f(t) - \mu_f]\cos(t - \varphi)}}{\sigma_f(\sqrt{2}/2)} \qquad t \in \{0,1,2,...,23\}, \tag{3.3}$$

where *f(t)* is the time series of data, φ is the phase that represents the maximum of the sinusoidal variation, and μ_f and σ_f are the mean and standard deviation of the time series, respectively. Thus, maximizing the linear correlation coefficient will yield the most appropriate phase of the diurnal maximum of a given variable. In the case of IR brightness temperatures, this would indicate the daily minimum of convection. Once the phase of the diurnal cycle has been calculated, the regressed amplitude of the variation can be found through a Fourier coefficient summation:

$$A = \frac{1}{\pi}\int_0^{2\pi} f(t^*)\cos(t^* - \varphi^*)dt^* \approx \frac{1}{12}\sum_{t=0}^{23} f(t)\cos(t - \varphi)\,. \tag{3.4}$$

The integral equation shown above is the continuous formulation of the Fourier coefficient for a variation with a period of 2π. This can be converted to a 24-hr period of discrete data values by considering the number of time steps per period and multiplying by the interval between data points. The regressed amplitude is a measure of the strength of the diurnal cycle, and as compared to the standard deviation of the time series, is a measure of the relative importance in describing the total variance of the time series. This is a more rigorous treatment of significance than that found in Liberti et al. (2001), who express amplitude simply as the difference between the maximum and minimum values of the composite time series. Such a difference would be more than twice the regressed amplitude as calculated above.

The procedure of constructing a composite time series and determining the phase and amplitude of the diurnal cycle can be repeated for various points across the domain to confirm the existence of a convective propagation signal across the domain. In this study, a propagation

signal is defined as a systematic variation in the phase of the diurnal cycle of a given variable with a coherent spatial structure. This propagation signal is assumed to exist because of some large-scale organization, whether due to gravity waves (e.g. Mapes et al 2003a,b), land/sea breeze convergence (e.g. Houze et al. 1981), or some other forcing mechanism.

3) Time cluster analysis

In the above discussion, a propagation signal was assumed to indicate the regular formation and passage of mesoscale convective systems such that the phase of the diurnal cycle increases in the direction of propagation. The validity of this assumption can be demonstrated through the technique of time cluster analysis, which tracks the large cold cloud shields of mesoscale convective systems through successive satellite frames in order to determine diurnal characteristics (such as the time of formation, dissipation, and maximum spatial extent) and the speed and direction of motion of such systems. Objective time cluster analysis was first used by Woodley et al. (1980) to assess convective systems over the GATE domain. Williams and Houze (1987) modified this technique to study the characteristics of winter monsoon convective cloud clusters over the southern South China Sea. Subsequent studies (e.g. Arnaud et al. 1992, Mapes and Houze 1993, Chen and Houze 1997, Machado et al. 1998, Zuidema 2003) used techniques similar to Williams and Houze (1987) to examine convective systems in different regions of the world.

The technique used in this study is most similar to that of Mapes and Houze (1993), as their region of emphasis (namely, the western Pacific warm pool) encompassed the South China Sea, and their choice of thresholds is appropriate for oceanic tropical convection. Wielicki and Welch (1986) provide a detailed description of a similar cloud cluster-finding algorithm. For each satellite frame, “line clusters”, or connected areas of cold cloudiness with IR brightness

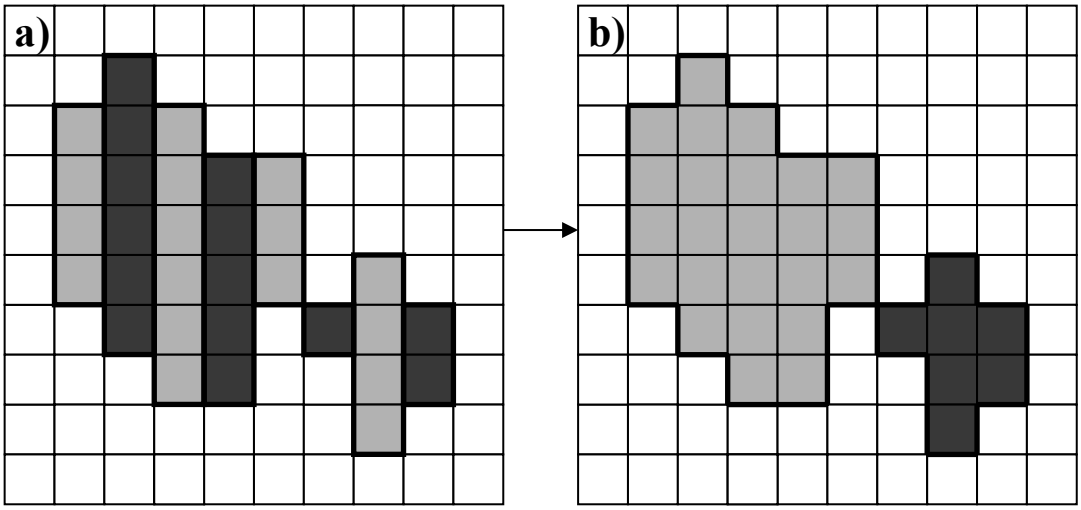

Figure 3.5 Schematic diagram showing the process of line and cloud cluster identification. Each box in the grids above represents a data point of IR brightness temperature. The first step in the process (image a) shows the identified line clusters, which are columns of connected elements that satisfy the brightness temperature criterion. In (a), line clusters are outlined in bold, and those in adjacent rows are alternately colored light and dark for emphasis. The second step (image b) shows the identification of cloud clusters, which are collections of line clusters whose adjacent members share at least one column. Two cloud clusters are identified in (b) and colored differently for emphasis; the diagonal they share is not adequate for association as a single cloud cluster.

temperatures below an arbitrary threshold, are found within each row of the satellite brightness temperature array (see Figure 3.5a). In order to focus on deep convective clouds, a threshold of 208K was maintained. After all of the line clusters have been identified in a satellite frame, they are then matched from one line to the next and considered "cloud clusters". Line clusters on two successive lines must share a column to be considered connected; diagonals are not sufficient (see Figure 3.5b). Once the cloud clusters have been identified in a frame, a routine sums the area and calculates the centroid position of the constituent pixels of each cluster. Since the satellite data were interpolated to a latitude-longitude grid with constant angular spacing, the area of each pixel varies as a function of latitude, reaching a maximum at the equator. The area can be expressed as

$$Pixel\ Area = (r_{earth}\Delta\varphi)(r_{earth}\Delta\lambda\cos\varphi) = 30.90\ km^2 * \cos\varphi,$$

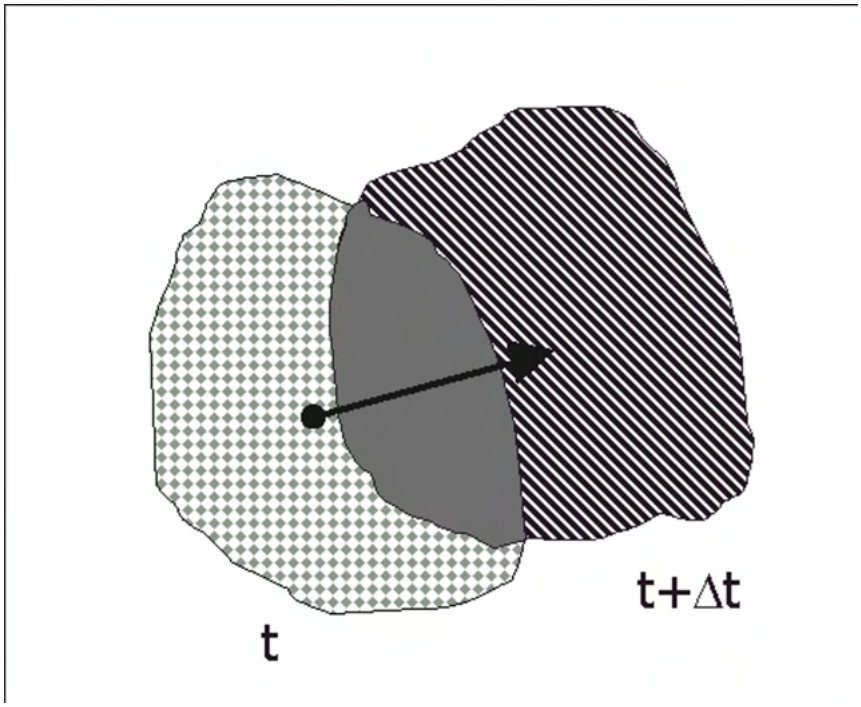

Figure 3.6 This schematic diagram shows the process of time cluster tracking. Cloud clusters in two satellite frames adjacent in time (separated by Δt), shown as bounded regions of different shading, were found to overlap. If intersection area of the two cloud clusters (solid) meets one of the two area criteria; if so, the two time clusters are assumed to be the same cloud system and tracked through time (time cluster).

where φ is the latitude of the pixel and $\Delta\lambda=\Delta\varphi=0.05^{o}$. Only the cloud clusters with a sufficient size (greater than 1000 km^2) are retained throughout the analysis. Centroid positions are calculated on an area-weighted basis to accurately reflect the spherical geometry of the earth's surface. Although some authors calculate centroid positions on a brightness temperature-weighted basis (e.g. Arnaud et al. 1992), that approach was not utilized here because the focus is already on some of the coldest of clouds, and the emergence and dissipation of convective towers could lead to a more discontinuous depiction of motion than by simply tracking the entire cold cloud shield.

Once all of the cloud clusters have been identified, another algorithm attempts to follow the clusters throughout their existence by considering the intersection of clusters in adjacent satellite

frames. Such ensembles of cloud clusters, tracked through time from birth to dissipation and considering splits and mergers, are called "time clusters". The process for identifying time clusters depends on the intersection area of two cloud clusters in neighboring satellite frames (Figure 3.6). If two cloud clusters overlap by a given threshold area, they are considered to be the same cloud cluster displaced by the difference in centroid positions of the two clusters. In such a circumstance, the two cloud elements would be included in the same time cluster array. In order to be considered the same time cluster, the area of intersection of two cloud elements must either be greater than 10^4 km^2, or it must be at least 50% of the area of either of the cloud clusters. Two thresholds are utilized to ensure that both large clusters, which may not necessarily overlap by 50% after splits, and small clusters, which can have an areal smaller than 10^4 km^2, are tracked appropriately. Additionally, the area of intersection must be compared to the area of both time clusters, as a growing (shrinking) time cluster may have a total area too large (small), as compared to its counterpart, to allow the 50% criteria to be met. By comparing the area of intersection to the area of both time clusters, the morphology of convective systems has much less of an effect on the tracking algorithm. Williams and Houze (1987) and Arnaud et al. (1992) give excellent discussions on the processes and pitfalls of time cluster tracking algorithms.

One caveat to time cluster tracking, which was not adequately discussed in previous literature, deals with the algorithm's ability to associate moving cloud clusters as being part of the same time cluster. As described above, two cloud clusters in successive satellite frames must overlap by at least some threshold area to be considered the same time cluster. This can be troublesome for smaller and fast moving cloud clusters, as both of these attributes will cause the intersecting area to be lessened. The problem can be best exemplified by considering the maximum speed that a cloud cluster of a given area can attain and still meet the area threshold criteria. The maximum velocity is simply the maximum distance between the centroids of two cloud clusters, divided by the time step, that yields an intersecting area that just meets one of the

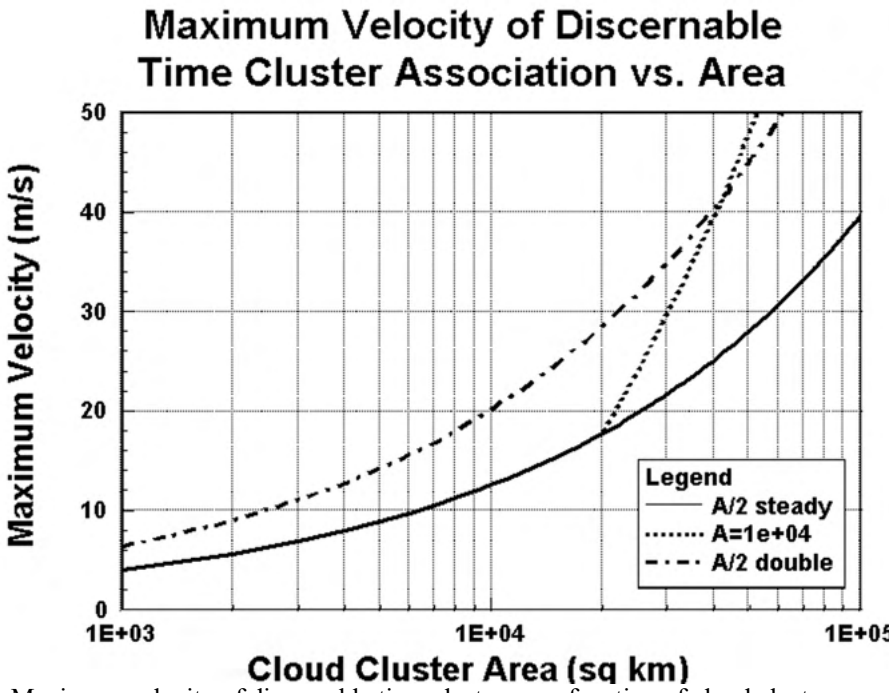

Figure 3.7 Maximum velocity of discernable time clusters as a function of cloud cluster area, shown for the two area criteria. The maximum velocity using the 10^4 km^2 threshold assumes a steady state and is only displayed over the range of its significance. Curves for the half-area criterion are shown for both cloud clusters with the same area (steady-state), and for cloud clusters whose areas double in one time step.

two area criteria; any more displacement over a given time step would lessen the intersecting area such that it fails to meet the criteria, and the time cluster connection would not be possible. Cloud clusters were assumed to be circular for the sake of simplicity. Even so, the resulting function for areal intersection is transcendental in nature, and the maximum distance between centroids was found through an iterative procedure. The maximum velocity for steady state (i.e. same area) time clusters is shown for both area criteria in Figure 3.7. The half-area criterion is difficult to satisfy for very small steady-state cloud clusters, as the maximum velocity for the cloud clusters up to $2\text{x}10^3$ km^2 is less than 6 m s^{-1}. The 10^4 km^2 area threshold becomes dominant for cloud clusters larger than $2\text{x}10^4$ km^2, and it has the effect of increasing the maximum allowable velocity over that suggested by the half-area criterion. Also shown in Figure 3.7 is the maximum velocity for the situation where a cloud cluster doubles in area over a given time step.

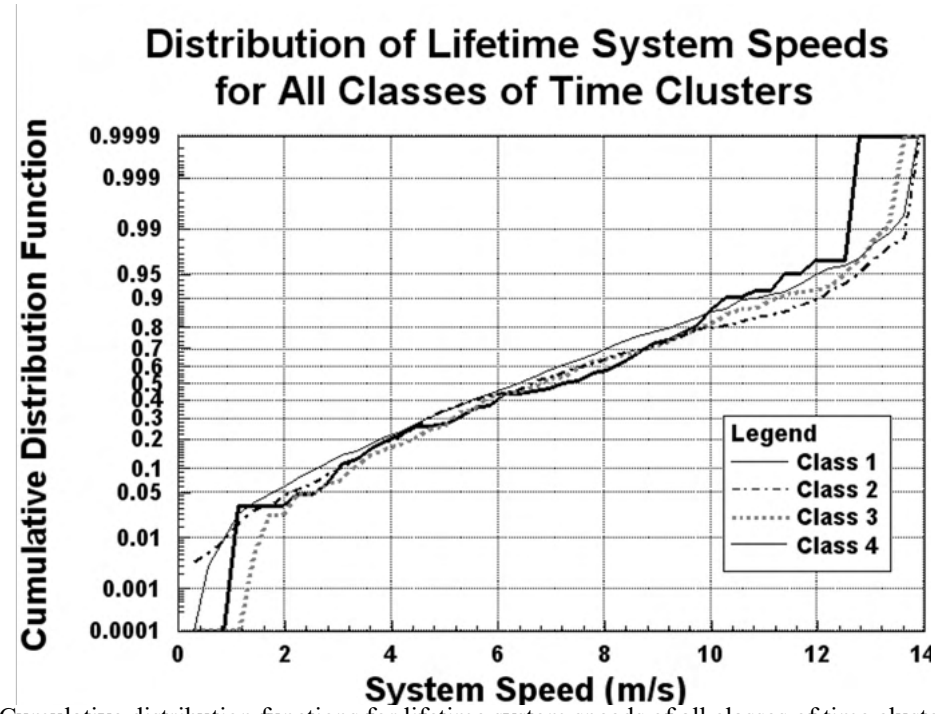

Figure 3.8 Cumulative distribution functions for lifetime system speeds of all classes of time clusters. The class of a time cluster is determined by the maximum areal extent of its constituent cloud clusters, with a higher number class indicating a larger system.

This situation occurs most often with the smallest cloud clusters (Machado et al. 1998), and has the effect of increasing the maximum allowable velocity over steady-state cloud clusters.

Figure 3.8 illustrates the distribution of system speeds for time clusters that were tracked in the northern SCS domain. The median speed of time clusters was approximately 7 m s^{-1}, and 90% of time clusters had speeds lower than 12 m s^{-1}. Realizing this, Figure 3.7 suggests that about half of steady state cloud clusters with areas of $3x10^3$ km^2 will not be properly associated. Since cloud clusters of that size are quite often increasing in area, the number of incorrectly unassociated cloud clusters is much lower, as the doubling-size curve suggests a miss rate closer to 10%. In addition, the distribution of system speed was only weakly dependent on system size, which would indicate that the smallest systems were being adequately captured. This information suggests that, because of the high temporal resolution of the satellite data, only small class 1

cloud clusters would be difficult to associate, and general inferences about time clusters will be robust in most circumstances. However, authors whose data were limited to a temporal resolution of three hours would have difficulty associating cloud clusters on the order of 10^4 km^2, but this was never mentioned in their analyses.

The threshold of 208 K was chosen to focus on deep tropical convection, and to ensure that splits and mergers, which are much more prevalent at higher brightness temperature thresholds, would not lead to anomalous propagation in the form of a connection between two unrelated convective systems. When a merger occurred, with two or more cloud shields merging into one contiguous shield in a single time step Δt, the life history of the merged time cluster at time $t+\Delta t$ was thought to be composed of the histories of both time clusters at time t, with the oldest system being dominant. When a split occurred, the two or more resulting cloud clusters were thought to belong to the same time cluster, with the future of each cloud cluster (i.e. splits, mergers, dissipation) adding to the same time cluster. Cloud clusters in a time cluster array were allowed to keep their individual identities and were stored with a link to their neighbors in adjacent time steps so the chronology of the time cluster and all of its constituent cloud clusters can be carefully followed. For statistical purposes, however, the time cluster was assumed to be a single entity at a given time step, with an area equal to the sum of the areas and a centroid given by the area-weighted average of the centroid of each element in the time cluster at that time step.

4) Evolution histogram

In order to understand the morphology of convective systems as it relates to the diurnal time scale, it would be advantageous to display the frequency of occurrence of cloudiness not only by hour, but also by brightness temperature at well. In this manner, one could witness the likelihood of cloudiness at all levels and for all hours of the day simultaneously. Such a diagram has been

called an “evolution histogram” by authors like Morcrette (1991). Its original emphasis, as in Morcrette (1991), was to diagnose the diurnal cycle of surface and atmospheric radiances from the standpoint of both satellite observations and model prognoses. Later, Chen and Houze (1997) and Yang and Slingo (2001) showed the evolution histogram’s applicability to diagnosing the diurnal cycle of tropical convection.

To construct an evolution histogram, spatial and temporal bounds must first be placed on the data to focus on a certain location and time. A composite analysis of the frequency distribution of brightness temperature is then conducted for each composite time step (in this case, one hour) by simply binning the brightness temperatures of each pixel in the spatial domain into the appropriate time step array, and then dividing by the total number of observations for that time step. In order to produce a relatively smooth frequency distribution, the brightness temperature bin size for this study was 4K. The histograms of composite hourly frequencies are displayed in vertical columns on the evolution histogram, such that the average relative frequency of occurrence for clouds of all brightness temperatures can be ascertained for any given hour of the day. The utility of the evolution histogram, however, is most evident by focusing on the rows of frequencies, as these reveal the diurnal cycle of the frequency of occurrence of clouds in a given brightness temperature bin. In this manner, the diurnal cycles of clouds with all brightness temperatures can be displayed in a single diagram, allowing inferences about the morphology of cloud systems to be made.

One of the difficulties in interpreting an evolution histogram involves the strong variation in frequency among different brightness temperature bins. Bins that typify the brightness temperature of clear air returns can contain more than 10% of the data for an arbitrary composite time step, while the bins of the coldest clouds might contain less than 0.1%, for a difference of at least two orders of magnitude. The strong dependence of frequency upon brightness temperature

often overpowers the subtle messages contained in the evolution histogram. To remedy this problem, Yang and Slingo (2001) took the concept of the evolution histogram one step further by subtracting the mean histogram of brightness temperatures of the entire data set from the histogram of each composite time step. The resulting histograms much more readily reflect when clouds of a given brightness temperature are more or less frequent than average, allowing for an easier interpretation of the diurnal cycle.

b. Radar methodologies

1) Determination of a bright band signature

Through the course of this study, it was beneficial to define the existence of a bright band signature in the vertical reflectivity profile of an arbitrary radar data point. Battan (1973) describes the radar presentation of a bright band as a horizontal band of intense echoes located ~0.5 km below the freezing level, which is caused by the melting of ice aggregates formed through stratiform precipitation processes. Such a bright band signature would be a sufficient condition to classify the precipitation production regime in the vicinity of said data point as stratiform (Steiner et al. 1995). Thus, the existence of a bright band signature could be used as a check for convective classification algorithms, which attempt to determine the precipitation production regime using radar reflectivity information. A precipitation region that exhibits a bright band signature in the vertical should be classified as stratiform, and this fact can be used to test the accuracy of a partitioning algorithm. Additionally, qualitative comparisons of radar variables can be made for data points with and without bright band signatures in their vertical reflectivity profiles. These comparisons can reveal which radar variables are best at

differentiating between the (stratiform) precipitation regimes that produce bright band signatures and those that do not, and can be used to refine a convective partitioning algorithm.

To determine the vertical layer in which to search for a bright band signature, it was advantageous to consider the techniques established in literature, the scanning strategy of the C-POL radar used in this study, and the frequency of the levels of maximum reflectivity in the data. Rosenfeld et al. (1995) defined the existence of a bright band as a maximum reflectivity in the vertical profile within ±1.5 km of the 0˚C altitude. Steiner et al. (1995) stated that a reflectivity maximum between 3 km and 5.5 km likely corresponded to a bright band signature. The freezing level height in their study, calculated from soundings averaged over a month, was approximately 5 km. A similar freezing level was found over the northern South China Sea during the SCSMEX experiment, so the layers indicated by previous authors should be applicable.

The scanning strategy of the C-POL radar was optimized to detect echoes up to 15 km high for ranges >30 km from the origin. A volume scan consisted of fifteen vertical tilts, ranging from 0.5˚ to 29.2˚. Near the edge of the radar domain's 142 km radius, the differences in vertical height of radar beams with the lowest tilts are between 1.5 km and 2 km. Thus, a layer with a depth ±1.5km surrounding the 0˚C level would be necessary to contain at least one radar beam, as suggested by Rosenfeld et al. (1995).

Figure 3.9 depicts the distribution of the level of maximum reflectivity, in kilometers above ground level, for all of the valid vertical columns of reflectivity used in this study. Only the vertical levels below 7 km are displayed in Fig. 3.9. The frequency of occurrence is small for heights below 2 km, and this can be partially attributed to the lack of radar data at these low levels. Far from the radar origin, the radar beam is higher above the ground, due to the curvature effect of the Earth. At these distances, the radar is unable to sample the lowest levels of the

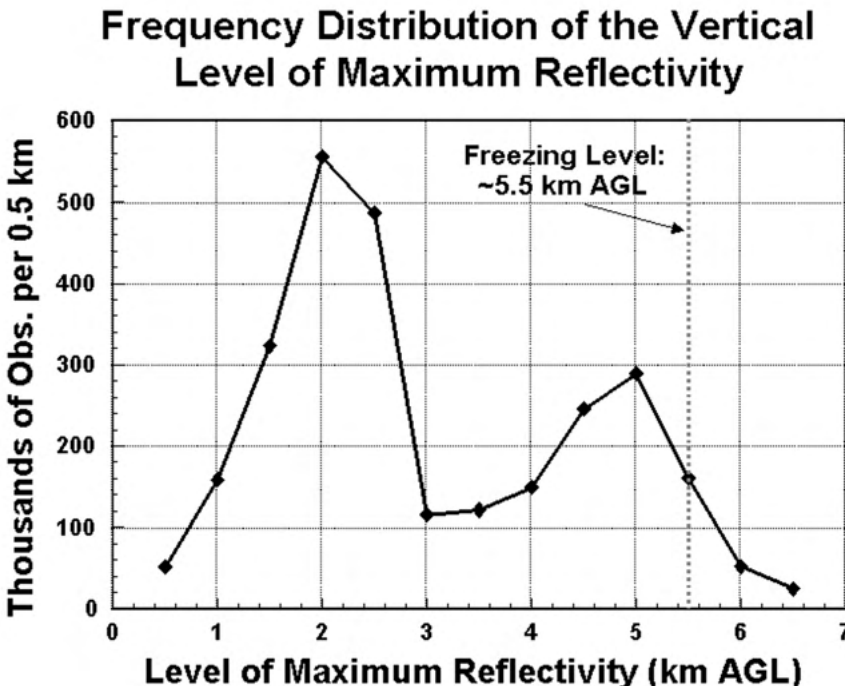

Figure 3.9 Frequency of occurrence of the level of maximum reflectivity for all valid vertical columns utilized in this study. Only the levels between 0.5 km and 6.5 km are considered. The rapid decrease of occurrence below 2 km can be partially attributed to the lack of data available at these levels, due to the increasing height of radar beams from the origin. The mean freezing level is denoted by the dotted line.

atmosphere. In the case of a tropical convective cell, Steiner et al. (1995) showed, on average, a monotonic decrease of reflectivity with increasing height. Thus, the level of maximum reflectivity for a tropical convective cell is typically the lowest available data level, and the maximum of occurrence for convective cells, as shown in Fig. 3.9, would be artificially shifted towards 2 km since data exists at this level across almost the entire domain.

The distribution of the level of maximum reflectivity shown in Fig. 3.9 is distinctly bimodal, with a maximum frequency at 2 km, and a secondary maximum at 5 km. As stated earlier, the 2 km maximum can be attributed partially to convective cells. The 5 km maximum is located near the 0ºC level, which is where the bright band is expected to exist. This bimodal distribution, considered in conjunction with previous examples in literature and the C-POL radar scanning

strategy, suggests that the existence of a bright band should be defined as a maximum of reflectivity in the vertical layers between and including 3.5 and 6.5 km AGL.

2) The bright band fraction

Rosenfeld et al. (1995) discuss the utility of the bright band fraction (BBF) in diagnosing areas of stratiform precipitation. They note that the existence of a bright band is difficult to detect with volume scanning radars because of the small vertical extent of the feature as compared to the radar beamwidth. To combat this difficulty, the BBF was defined as the fraction of echo area within a ~7 km x 7 km window that exhibited a bright band signature in the vertical reflectivity profile. This fraction ranged from 0 to 1, and was shown to provide good separation between precipitation regimes; the highest rain rates coincided with low values of BBF, while the rain rates associated with high values of BBF were almost exclusively below 10 mm hr^{-1}. Rosenfeld et al. (1995) suggested that the BBF would be good at distinguishing between convective and stratiform precipitation regimes in the following way: $0.0 \leq BBF < 0.4$ convective, $0.4 \leq BBF < 0.6$ transition, and $0.6 \leq BBF < 1.0$ stratiform. Because the BBF will not be used as the sole indicator of precipitation regimes in this study, values of BBF greater than 0.5 are defined as indicative of stratiform precipitation processes.

3) The working level of horizontal reflectivity

For the sake of consistency, the same level of horizontal reflectivity will be used in calculations through the study. The selection of a working level requires consideration of several factors, including the height of the bright band, evaporation effects, and the maximum desired radius of radar information. In the case of partitioning echoes into stratiform and convective contributions (discussed in Appendix A), Steiner et al. (1995) suggest that any level below the

bright band can be used. The 0ºC level in their study and in the current study was approximately 5 km altitude, and this sets the upper bound for the working level. Regarding the effects of evaporation, Steiner et al. (1995) indicate that a level at or below 3 km MSL would be appropriate such that the precipitation pattern represented by the echoes at said level would be representative of precipitation accumulation at the surface. This argument only applies to the moist tropical atmosphere, and a lower level would need to be chosen for midlatitude studies. Finally, the working level must be high enough to extend the range of radar data as far as possible. The maximum data range of the C-POL radar was 142 km, and the lowest tilt angle was 0.5º. Under standard atmospheric conditions, a data level of at least 2.5 km MSL would be adequate to capture the entire data range of the radar. Thus, the working level was chosen to be 2.5 km, since the lowest data level that encompassed the entire radar domain, while minimizing bright band contamination and evaporation effects.

Chapter 4: General aspects of 1998 Southeast Asian Monsoon

a. Summary of events relating to monsoon onset and evolution

Before focusing on the diurnal cycle of convection over the South China Sea (SCS) region of interest, it is important to examine the long-term evolution of the monsoon for the 1998 study period. As mentioned in chapter 1, the Asian monsoon system is temporally and spatially variable through the course of a given season. However, the summer monsoon follows a common pattern characterized by an onset in the South China Sea region, and the northward progression of the monsoon convergence zone, and hence convective activity, throughout the summer months. The fact that the convergence zone often advances northward in a discontinuous fashion, with sudden jumps separating periods of little movement, may allow the dataset to lend itself readily to subdivision. Considering subdivided datasets can increase the amplitude of the diurnal signal in each subperiod, and would increase confidence in the statistical analysis if there were agreement amongst the divided data.

It is also important to consider the 1998 Asian monsoon in context of average monsoon conditions. The 1997-1998 El Niño event was one of the strongest on record, and this may have had implications as to the development and maintenance of the Southeast Asian monsoon in 1998. Indeed, there were definitely some anomalous aspects of the 1998 monsoon. The onset of convective activity was slightly delayed as compared to other years, occurring 15-20 May in 1998, but early-mid May in typical years. The northward penetration of convective activity was relatively weak, reaching only 30ºN in 1998 as compared to 40º-45°N in a normal year. Thirteen

typhoons developed in 1998, well below the average seasonal total of 28. And finally, there was extremely severe flooding in the Yangtze River Basin, which was caused by a prolonged stationary period in the monsoon convergence zone. (Chang and Chen 1995, Ding and Liu 2001)

Ding and Liu (2001) provide an excellent, detailed description of the meteorological events that transpired during the onset and progression of the monsoon in 1998. A brief summary of their work is included here for a better understanding of the large-scale patterns evident in 1998. The onset of convective activity over the SCS was shown to occur in two phases. The first onset took place over the northern SCS, and was likely caused by a combination of midlatitude and tropical influences. The northern onset process began with the development of a low-level twin cyclone straddling the Equator near the longitude of Sri Lanka, as is often the case when the onset first occurs in the northern SCS. Westerly winds were accelerated between the two cyclones, and as the cyclones advanced eastward these westerly winds penetrated into the SCS region around 15 May. This marked the beginning of the monsoon flow over the region, and was consequently followed by a distinct increase in precipitation. Interestingly, the westerly wind surge was also accompanied by a southward intrusion of cold air into the northern SCS. A latitude-time Hovmöller diagram of 850 hpa temperatures (Figure 4.1) clearly shows a cold anomaly slowly sinking southward through China in early May, reaching the northern SCS latitudes by 15 May. These data are supported by the coexistence of an upper-level trough, and by satellite observations of a southward-moving band of low outgoing longwave radiation. Thus, the initial onset of the monsoon over the northern SCS seems to be caused by an interaction between a midlatitude weather system and the tropical monsoon current. Other authors have documented this sequence of events in previous years (e.g. Chang and Chen 1995).

The onset over the central and southern SCS region did not occur until around 20 May. The western Pacific subtropical ridge was slower to retreat here as compared to the northern SCS, and

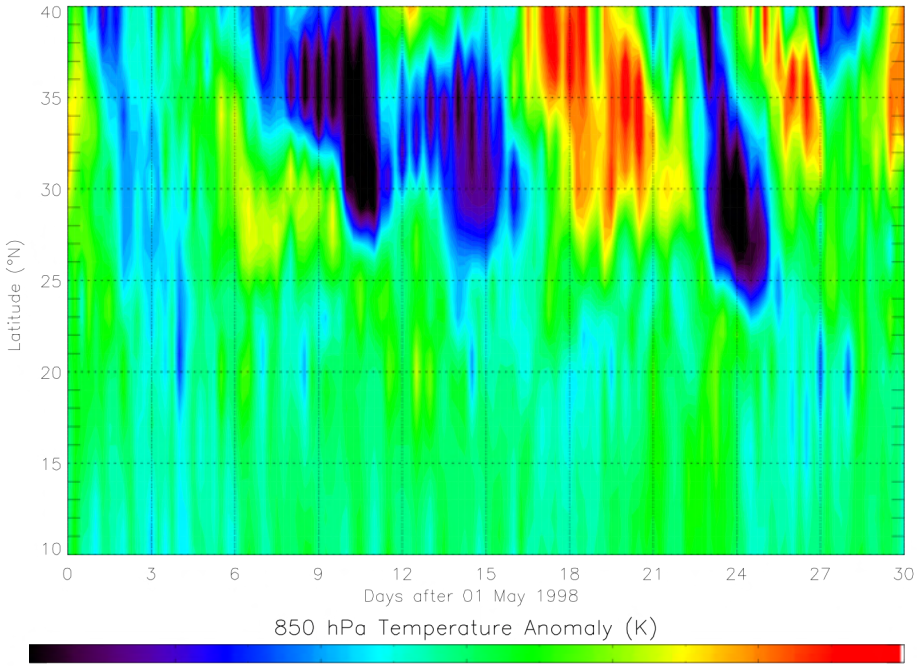

Figure 4.1 Latitude-time Hovmöller diagram of 850 hPa temperature anomalies along 117ºE longitude. The times along the abscissa are days after 1 May 1998. Values shown are calculated by subtracting average 850 hPa temperatures for the month of May from instantaneous values at a given latitude. (Adapted from Ding and Lau 2001)

the midlatitude weather system was unable to penetrate this far into the tropics. A fundamental change in circulation features was required before westerly winds finally dominated over the entire SCS and rainfall increased markedly in the south. Additionally, the existence of a westward-moving mixed Rossby-gravity wave was found in upper level wind data (Johnson and Ciesielski 2002)), and a possible link between it and the timing of the monsoon onset over the southern SCS was speculated.

After the onset in mid May, the low-level monsoon convergence zone remained in the vicinity of the SCS until mid June, when it shifted rapidly into China (near the Yangtze River). It remained stationary in southern China through the rest of June, and subsequent rounds of convective activity caused severe flooding over the region. The monsoon convergence zone

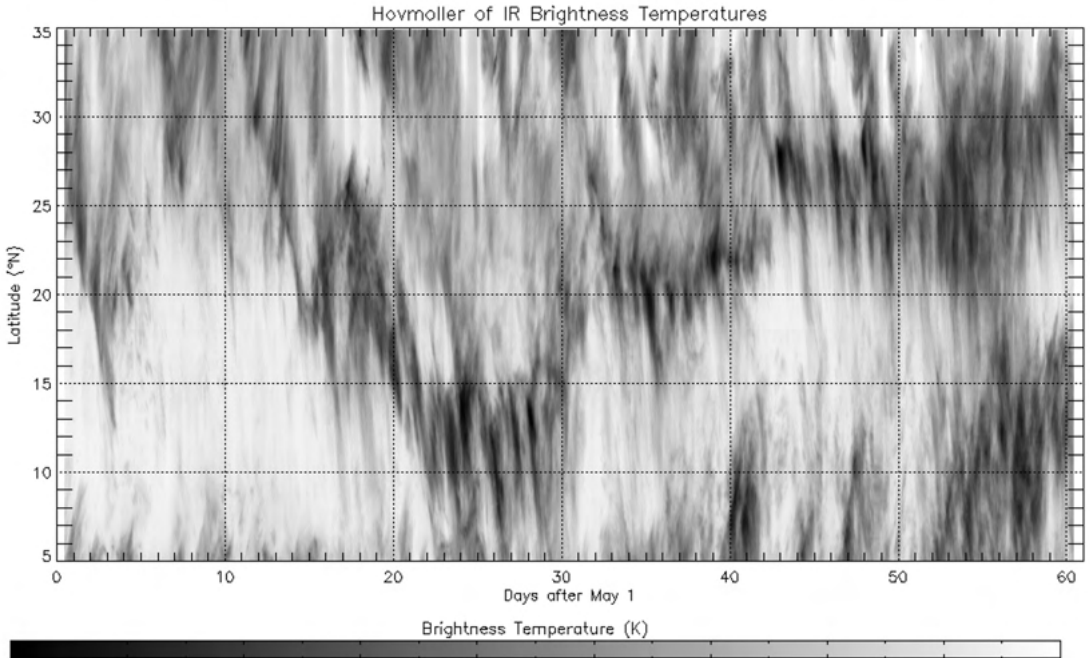

Figure 4.2 Latitude-time Hovmöller diagram of infrared brightness temperatures over the study region. The values along the abscissa are days after 1 May 1998, and cover the entire range of the available infrared dataset (1 May-30 June). Values shown are that of brightness temperature averaged over the 116º-117ºE longitude band, which was chosen to coincide with the location of the Dongsha Island radar.

briefly penetrated farther northward in early July, but returned to the Yangtze River basin in mid July for another round of flooding. However, the available satellite record for this study only extends to 30 June, so the focus will be on the days in this period when convection was present over the SCS region.

A Hovmöller diagram of infrared (IR) brightness temperature is shown in Figure 4.2. Fig. 4.2 covers the latitude range of 5º-35ºN, the time interval 1 May-30 June 1998, and displays values of IR brightness temperatures averaged over the 116º-117ºE longitude band to coincide with the position of the Dongsha Island C-POL radar. During the first part of May, an organized area of low brightness temperatures, indicative of the high cloudiness typically associated with convective activity, penetrates southward into the northern SCS. This is not the monsoon onset, however, because it is not accompanied by a westerly wind surge, and is followed by clear sky

conditions for ~10 d. Between 10-15 May, another organized area of low brightness temperatures (i.e. cold cloudiness associated with a midlatitude disturbance) can be seen propagating southward through the latitudes that are located in mainland China at this longitude. Convective development begins along the frontal boundary over the northern SCS around 15 May, which represents the monsoon onset over the northern SCS as previously discussed. For the next six days (15-20 May), the coldest brightness temperatures are confined to the 15º-25ºN latitude band. During this time, individual streaks of low brightness temperature are discernable, and each exhibits southward propagation (to be discussed in detail later).

The onset of convective activity over the central and southern SCS (south of 15ºN) is evident in Fig. 4.2 after 20 May. Several large mesoscale convective systems occurred in this region between 20-30 May, which are again represented by discrete bands of lower brightness temperature. The southward propagation of individual cloud systems is much more pronounced in this time period, with the first low brightness temperatures regularly appearing between 12º and 15ºN, and extending southward with time often as far south as 5ºN. The regular appearance of these features suggests the possibility that some sort of diurnal forcing is organizing the initiation of cloud systems in this region. During the same time period, it is interesting to note that the northern SCS is relatively quiet, with higher brightness temperatures indicating a lack of convective activity. This would suggest that the main focus of low-level convergence in the monsoon flow has shifted south, out of the northern SCS and into the central and southern SCS, where it remains relatively stationary for approximately 10 days.

An abrupt shift in the cloud pattern is apparent around 1 June, when the band of lowest brightness temperatures quickly shifts northward into the vicinity of the southern China coast (around 23ºN at this longitude band). As in the previous two periods, regularly spaced streaks of cold brightness temperature suggest the diurnal formation and southward propagation of

convective cloud systems through the northern SCS. The band of low brightness temperatures remains along the southern China coast for another 10 days before shifting rapidly northward into the southern Yangtze River basin of China (26º-30ºN). Repeated convective events occur here through the remainder of the month of June, causing severe flooding in the region (Ding and Liu 2001). Compared to the active monsoon onset, brightness temperatures over most of the SCS region remain relatively high in the latter half of June, with a few exceptions. Brightness temperature depressions in the far northern SCS appear to be linked to the remnants of convective systems that form over southern China. A more organized area of low brightness temperatures appears over the far southern SCS latitudes in late June, associated with a low-latitude westerly wind surge. However, attention will be appropriately focused on the period when systems most often initiated and propagated over the SCS, namely 15 May-14 June.

b. Average monsoon characteristics and selection of time periods

With the available dataset of infrared brightness temperatures, there are several ways to explore the average characteristics of monsoon convection over the study region, each with its own advantages and disadvantages. Averages of brightness temperature are useful in depicting areas that are frequented by cold cloud cover. Over the open waters of the SCS, the only factors that significantly affect the observed brightness temperature are the existence and height of cloud cover. Even so, the average brightness temperature information is ambiguous, as it cannot explicitly differentiate between regimes of sporadic cold cloudiness (i.e. that related to convective activity) and more persistent, warmer cloudiness. The standard deviation of brightness temperature can help to remove some of this ambiguity by determining the variability of cloudiness associated with each average brightness temperature. Figure 3.3 depicts the relationship between the average and standard deviation of brightness temperature over the region of interest, with the anticipated result of higher standard deviations being associated with lower

averages. This suggests that, to first order, a lower average brightness temperature is an indication of increased convective activity over the SCS.

To better determine the level of convective activity over a given period of time, averages of the percent occurrence of high cloudiness and the Deep Convective Activity (DCA, section 3.a.1) will also be considered. Percent occurrence of high cloudiness at a given location is simply the ratio of the number of satellite frames in which the brightness temperature is below a threshold value to the total number of frames in a given time period. The threshold of 208K is selected as a typical value for focusing on deep tropical convective cloudiness (see section 3.a.1). Figure 3.1 reflects a generally good relationship between the DCA and radar-estimated precipitation over the study region, so an average DCA value can be satisfactorily interpreted as average satellite-estimated precipitation. These two methods provide a more precise measure of convective activity and will be used in conjunction with brightness temperature average and standard deviation data to arrive at a more complete understanding.

1) The "full" period, 1 May-30 June 1998

Figures 4.3a-d portray the average convective activity for the full record of satellite data (1 May-30 June 1998, hereafter the "full" period) using the four methods described above. The lowest average brightness temperatures (Fig 4.3a) are found in the southern Bay of Bengal off the western tip of Sumatra. This is not surprising, as the Bay of Bengal is often the site of the highest mean precipitation of the entire Asian monsoon region (Zuidema 2003). A band of relatively low average brightness temperatures extends northeastward through the Bay of Bengal, along the southern coast of China, and through the islands of Japan. This corresponds to the most frequent location of the cloudiness associated with the monsoon convergence zone during this time period. Other locations with relatively low brightness temperature averages in Fig. 4.3a include coastlines

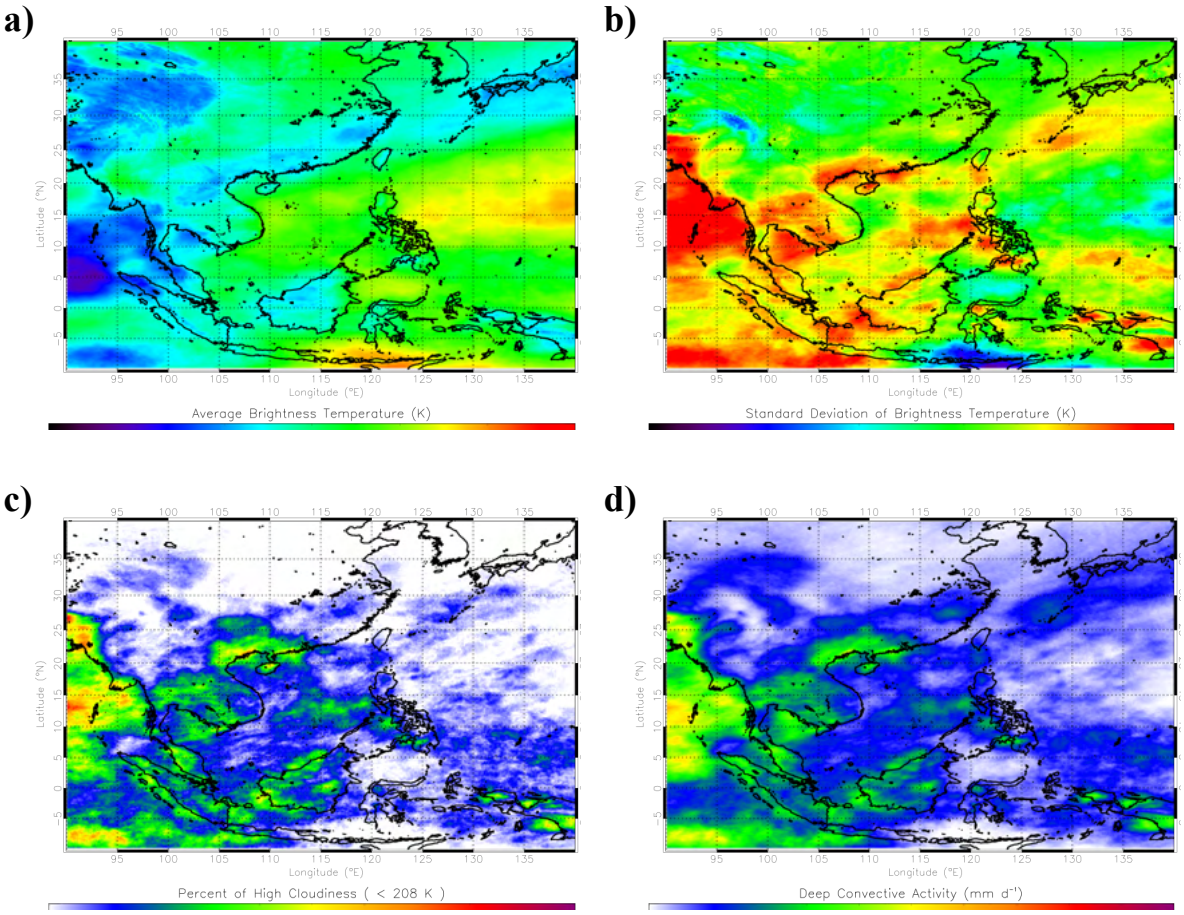

Figure 4.3 Averages of infrared satellite parameters indicative of convection for the "full" period (1 May-30 June 1998). In general, lower brightness temperature averages in (a), higher brightness temperature standard deviations in (b), higher percent of high cloudiness in (c), and higher deep convective activity values in (d) all suggest increased convective activity over tropical oceanic regions.

(i.e. the coast of Sumatra), coastal concavities (the Gulf of Thailand), islands (Hainan, Taiwan, and New Guinea), and the Himalayan Plateau; not all of these regions are frequented by convective activity. The highest brightness temperature averages in the northern hemisphere are east of the Philippines and between 10º-25ºN, which coincides with the average position of the western Pacific subtropical high. In the SCS region of interest, averages are moderate in magnitude, with the lowest values located just off the southern China coast and the northwestern coast of Borneo, and slightly higher averages in the central SCS (along 15ºN).

The standard deviations of brightness temperature for the full period, found in Figure 4.3b, exemplify the ambiguity in considering average brightness temperature alone. In some circumstances, low averages in Fig 4.3a match well with high standard deviations in Fig 4.3b, a relationship that suggest increased convective activity. Good examples are along the southern China coast west of Hong Kong, the island of Hainan, the Gulf of Thailand. However, there are some noticeable departures from this relationship. For example, the highest standard deviations in the Bay of Bengal are to the north of the lowest average brightness temperatures, which would indicate that the southern average minimum is caused by more persistent cloud cover. The convective band seen extending southwest-northeast in Fig 4.3a is not as obvious in Fig 4.3b, especially to the north of 25ºN. Perhaps the most striking departures are the highlands of the Himalayas, Taiwan, and New Guinea, where both average and standard deviation are at a minimum. This may seem counter-intuitive, as one would expect significant variability associated with deep convection in addition to the diurnal cycle over highland regions. Liberti et al (2001) noted similar behavior over the highlands of New Guinea. Over the SCS, brightness temperature average and standard deviation exhibit a generally inverse relationship, suggesting the utility of low averages and high standard deviations in diagnosing convective activity in this region.

A more definite measure of deep convective activity is found in the percent of high cloudiness (< 208 K) during the full period (Figure 4.3c), generally confirming the results of Figs. 4.3a-b. High clouds were most prevalent over the Bay of Bengal during this period, as well as along the southern China coast, the island of Hainan, and the region around Bangladesh. Relatively low values were found over Taiwan and the highlands of New Guinea. Two areas of enhanced occurrence of high cloudiness are over the SCS; a weaker band north of and along 20ºN that stretches eastward from the maximum over southern China, and a stronger band between 10º

and 15ºN with no apparent connection to land. Almost no high cloudiness is apparent north of 30ºN, indicating that any convective cells which formed in this region were not as deep as those in the tropics. Thus, the threshold chosen is only useful in diagnosing the prevalence of tropical convection.

The average DCA (Figure 4.3d) paints a similar picture to that of the percent of high cloudiness. However, because the threshold of a non-zero DCA value is lower (brightness temperature $\leq$ 230K), it is not a mirror image. The highest values of DCA, exceeding 25 mm d^{-1}, are located in the central and southern Bay of Bengal. Other DCA maxima are typically located on the southwestern coastlines of the Asian continent (e.g. the Andaman sea, the Gulf of Thailand, and Malaysia) and several of the major islands in the "Maritime Continent" (Sumatra, Borneo, the Philippines, and New Guinea). DCA values are high along the southern China coast west of Hong Kong, and extension of these high values continues eastward along 20ºN in the northern SCS. As with high cloudiness, a second, stronger area of high DCA is found in the central SCS between 10º and 15ºN.

Two main conclusions should be drawn from Figs. 4.3a-d. First, although not applicable everywhere, the four figures generally agree about the distribution and magnitude of convective activity over the SCS study region. Thus, brightness temperatures, cold cloudiness, and DCA will be used somewhat interchangeably in further diagnoses. Second, the SCS was characterized by intermediate convective activity period during the early 1998 monsoon season. While not as regular as the Bay of Bengal, the level of activity over the SCS was on par with other regions of the Maritime Continent. Additionally, it was evident in Fig 4.2 that most of the convective activity over the SCS occurred in late May and early June. Thus, it may be advantageous to focus on this subset of data to amplify the convective signal over the study region.

2) The “MYJN” period, 15 May-14 June 1998

To achieve this focus, most of the analyses in this study are conducted over the time period 15 May-14 June 1998 (hereafter the “MYJN” period). The start of the MYJN period was chosen to logically coincide with the onset of the monsoon over the SCS region. Obviously, the choice excludes the pre-monsoon activity that is evident over the region from 1-5 May (Fig. 4.2), but this allows the analyses to be based solely on convection driven by the summer monsoon regime. The end of the MYJN period roughly corresponds with the rather discontinuous movement of monsoon convection out of the SCS and into southern China. Such movement is clearly evident in Fig. 4.2, as the latitude with the coldest brightness temperature jumps from 22ºN to 28ºN in the course of approximately one day (day 42). Convective activity that occurs in the SCS region after 14 June is excluded from MYJN analyses. However, this exclusion is deemed to be insignificant, because the activity in the northern SCS is associated primarily with decaying remnants of mesoscale convective systems (MCSs) that developed over southern China, and the activity over the southern SCS is caused by a low-latitude westerly wind surge that appears to be unrelated to the main monsoon convergence zone (Ding and Liu 2001). The 31 day length of the MYJN period is sufficient to capture many episodes of convective development over the SCS region, adding to the statistical significance of analyses conducted over that time period.

Figures 4.4a-d depict the level of convective activity during the MYJN period using the same four methods as in the previous subsection. Comparisons with the full period (Figs. 4.3a-d) reveal differences in both the location and intensity of convective activity between the two time periods, and illustrate the benefits of using the MYJN period to analyze convection over the SCS. One of the most notable differences between the MYJN and full periods is apparent in the average brightness temperature fields (Figs. 4.3a and 4.4a). A band of low brightness temperatures extends from the Bay of Bengal toward the northeast in both periods, but in the

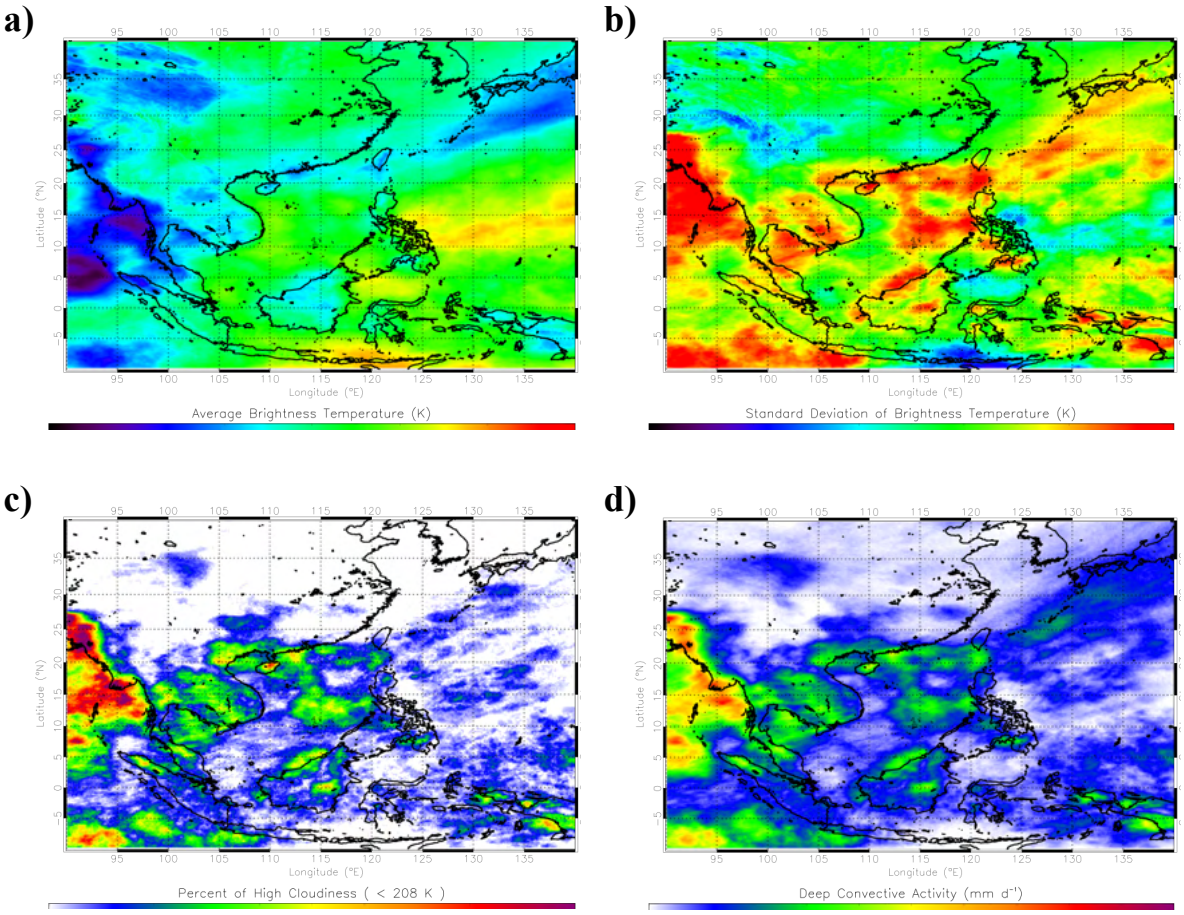

Figure 4.4 Averages of infrared satellite parameters indicative of convection for the "MYJN" period (15 May-14 June 1998). In general, lower brightness temperature averages in (a), higher brightness temperature standard deviations in (b), higher percent of high cloudiness in (c), and higher deep convective activity values in (d) all suggest increased convective activity over tropical oceanic regions.

MYJN period this band is shifted south of its full period position (east of 110ºE). This is a consequence of the MYJN period selection, as the monsoon convergence front had not yet jumped into southern China by the end of the period. Instead, the band of low brightness temperatures is located in the northern SCS, where the front remained stationary on two separate occasions during the period.

The other indicators of convective activity over the SCS region confirm that the MYJN period is more active, on average, than the entire full period. This fact is substantiated by

increases in brightness temperature standard deviation (Fig. 4.4b), the percent of high cloudiness (Fig. 4.4c), and the DCA (Fig 4.4d). Because the MYJN period is a subset of the full period, this would imply that most of the convective activity over the SCS region during the full period actually occurred within the bounds of the MYJN period, which is a very desirable result. However, these same indicators, along with the Hovmöller diagram of brightness temperature (Fig. 4.2), indicate that further subdivision is possible within the MYJN period. Fig. 4.2 clearly shows that the band of convective activity goes through three "quasi-stationary" phases over the SCS during the MYJN period, and the transitions between these phases are relatively abrupt and discontinuous. Figs. 4.4b-d confirm this by showing two discrete maxima of convective activity over the SCS; one just off the southern China coast in the northern SCS (along 20ºN), and the other in the central SCS (along 12ºN). Examining the behavior of convective activity during these individual subperiods would help to isolate the diurnal signals of each stationary phase, and comparing these to the entire MYJN period would beneficially increase the statistical significance of similar results.

3) The "PD1" period, 15-20 May 1998

The first stationary phase of monsoon convection during the MYJN period occurred over 15-20 May (hereafter the "PD1" period), which coincided with the monsoon onset over the northern SCS. During this six day period, the lowest average brightness temperatures (Figure 4.5a) extend in a continuous band from the Bay of Bengal east-northeastward through the northern SCS to Taiwan, and onward south of the islands of Japan. Average brightness temperatures in the central SCS were generally above 290K, which is close enough to the clear air value to suggest almost cloud-free skies during this period. Standard deviations of brightness temperature (Fig. 4.5b) mirror the average brightness temperature results, with high values in the northern SCS and low values in the central and southern SCS. The DCA distribution (Fig 4.5c) is also similar, with

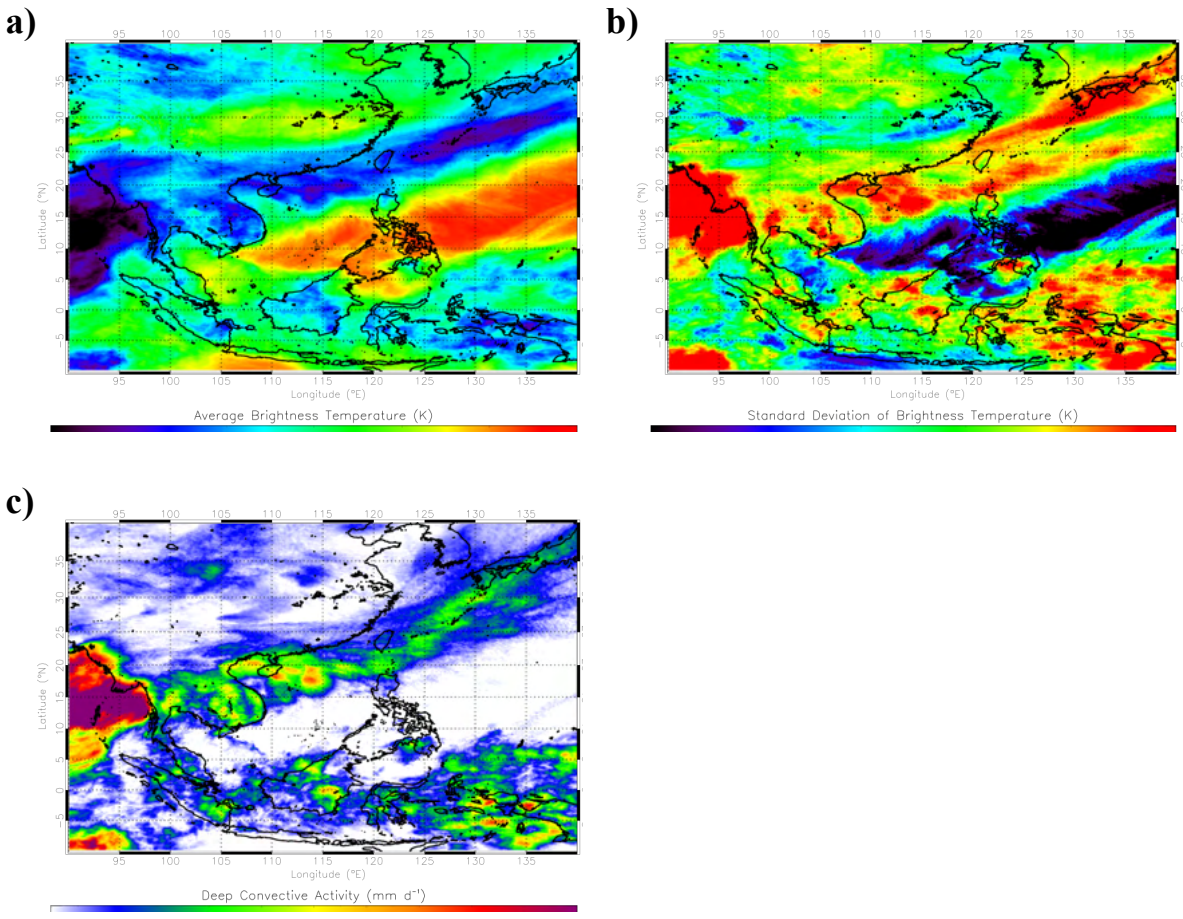

Figure 4.5 Averages of infrared satellite parameters indicative of convection for the "PD1" period (15-20 May 1998). In general, lower brightness temperature averages in (a), higher brightness temperature standard deviations in (b), and higher deep convective activity values in (c) all suggest increased convective activity over tropical oceanic regions.

average values of 10-30 mm d^{-1} over the northern SCS and almost zero over the central and southern SCS. Figs. 4.5a-c all demonstrate that during PD1, the convective activity over the SCS region was confined to the northern SCS, generally north of 15ºN.

Figures 4.6a-b illustrate the average lower- and upper-level flow patterns that generated the convection during PD1. The twin cyclones that aided the northern SCS monsoon onset (Ding and Liu 2001) are accelerating 850 hpa southwesterly flow, extending from the western edge of the domain through Indochina and into the northern SCS (Fig. 4.6a). Naturally, this air current

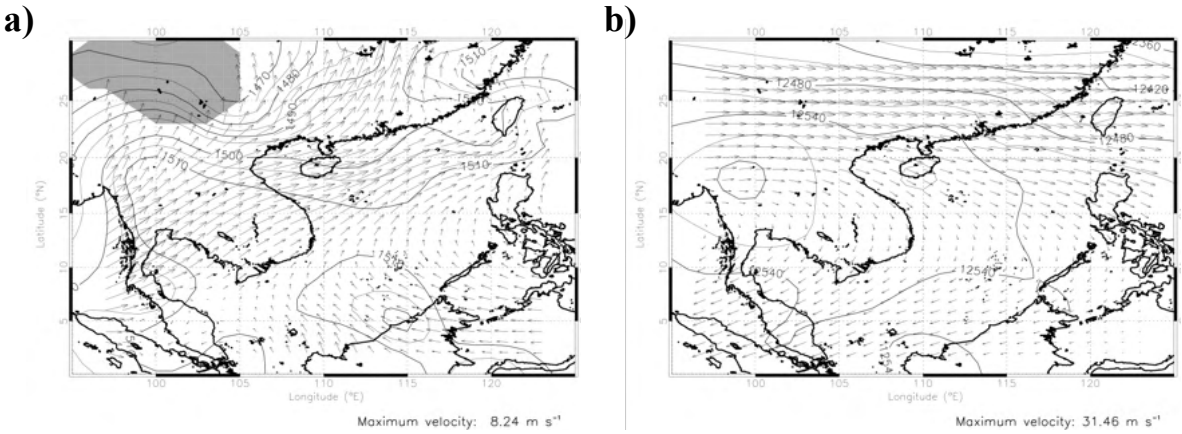

Figure 4.6 Average geopotential heights and winds at (a) 850 hPa and (b) 200 hPa during the "PD1" period (15-20 May 1998). Areas shaded in gray in (a) indicate where the 850 hPa level is below ground.

coincides with the belt of maximum convective activity across the region, indicating the importance of the moist, lower-level southwesterly flow in maintaining convective development. Although not obvious in the geopotential height field, the anticyclonic curvature of winds over the central and southern SCS suggest the western Pacific subtropical ridge is still present and is responsible for suppressing convective development during PD1. Meanwhile, an upper level anticyclone was beginning to dominate the 200 hpa flow over the SCS (Fig. 4.6b), which is another indication of the summer monsoon onset over the region. The upper-level trough associated with the midlatitude cold-air intrusion into the SCS region has moved off the eastern edge of the GAME domain, but relatively strong northwesterly flow still exists in the upper levels over the northern SCS (> 20 m s^{-1}).

4) The "PD2" period, 21-31 May 1998

The second stationary phase of monsoon convection during the MYJN period took place over 21-31 May (hereafter the "PD2" period), or the eleven days after the monsoon onset over the central and southern SCS. The pattern of coldest average brightness temperatures over the region

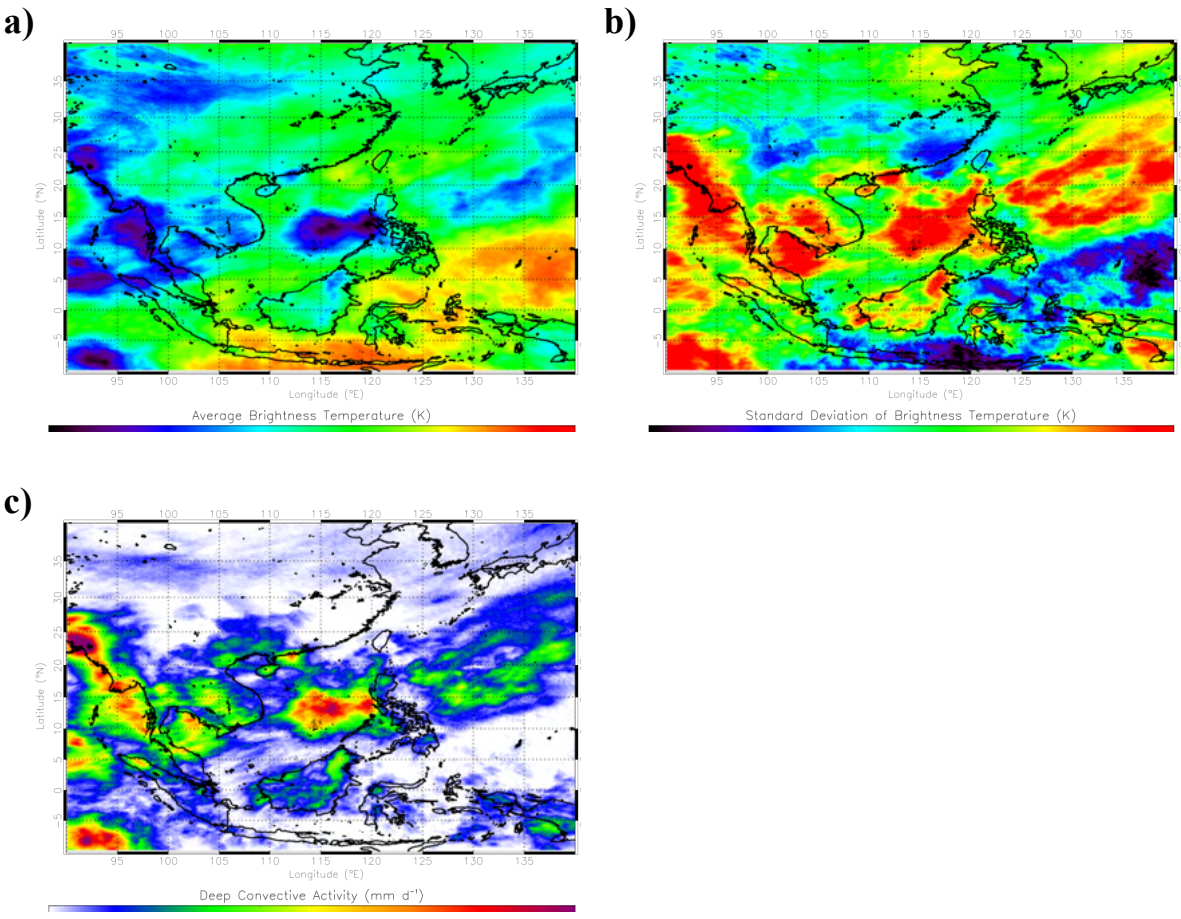

Figure 4.7 Averages of infrared satellite parameters indicative of convection for the "PD2" period (21-31 May 1998). In general, lower brightness temperature averages in (a), higher brightness temperature standard deviations in (b), and higher deep convective activity values in (c) all suggest increased convective activity over tropical oceanic regions.

(Figure 4.7a) is different than in all of the previous examples, with no evident continuous band. Instead, there are several discrete minima of average brightness temperatures, located over open ocean waters and along the windward side of landmasses. The most prominent minimum over the SCS region is generally between 9º-16ºN, where MCSs repeatedly develop and decay during this time period. Average brightness temperature values are generally higher over the northern SCS, indicating decreased convective activity, with a notable exception along the southern China coast west of Hong Kong. Standard deviations (Fig. 4.7b) are more cluttered than in previous examples, but agree that the greatest convective activity over the SCS region is in the 9º-16ºN

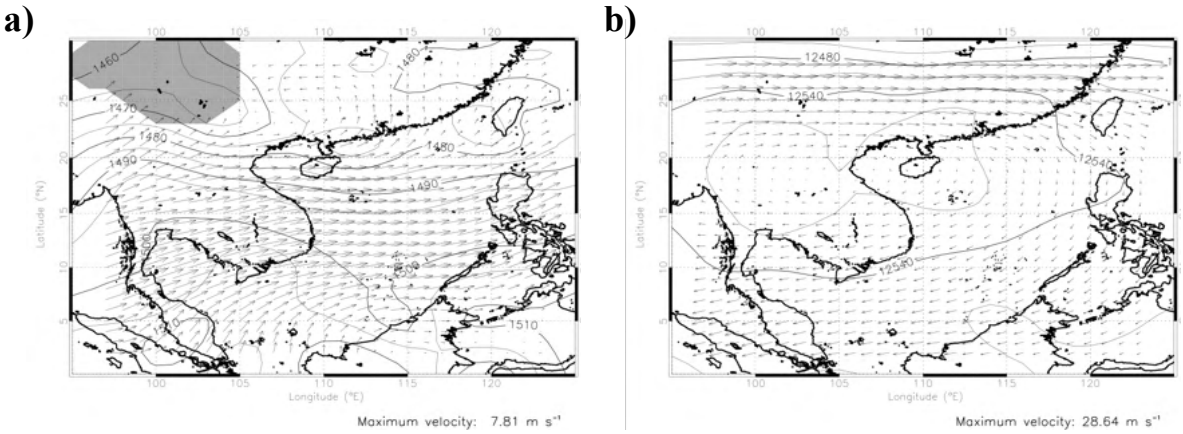

Figure 4.8 Average geopotential heights and winds at (a) 850 hPa and (b) 200 hPa during the "PD2" period (21-31 May 1998). Areas shaded in gray in (a) indicate where the 850 hPa level is below ground.

latitude band. DCA values (Fig. 4.7c) over the central SCS during PD2 are higher than those over the northern SCS during PD1, with maximum PD2 averages approaching 50 mm d^{-1}. In general, Figs. 4.7a-c all confirm that the greatest convective activity over the SCS region during PD2 was confined to the region north of 9ºN, south of 16ºN, east of 112ºE, and west of the Philippines.

The average 850 hpa flow over the SCS during PD2 (Fig. 4.8a) is notably different from PD1 (Fig. 4.6a). The low-level tropical monsoon current shifts southward into the central SCS during PD2, as the western Pacific subtropical high retreats out of the region. The acceleration of westerly winds over the central SCS marks the full summer monsoon onset and is responsible for the intense convective activity in this area. The 850 hpa flow over the northern SCS is weaker and more diffluent in PD2 than in PD1, resulting in decreased convective development there. In the upper levels (Fig. 4.8b), the strong northwesterly flow over the northern SCS during PD1 diminishes significantly in PD2, as the midlatitude trough is replaced by the strengthening anticyclone centered along 20ºN. Light north or northeasterly flow dominates the 200hpa flow over the central and southern SCS.

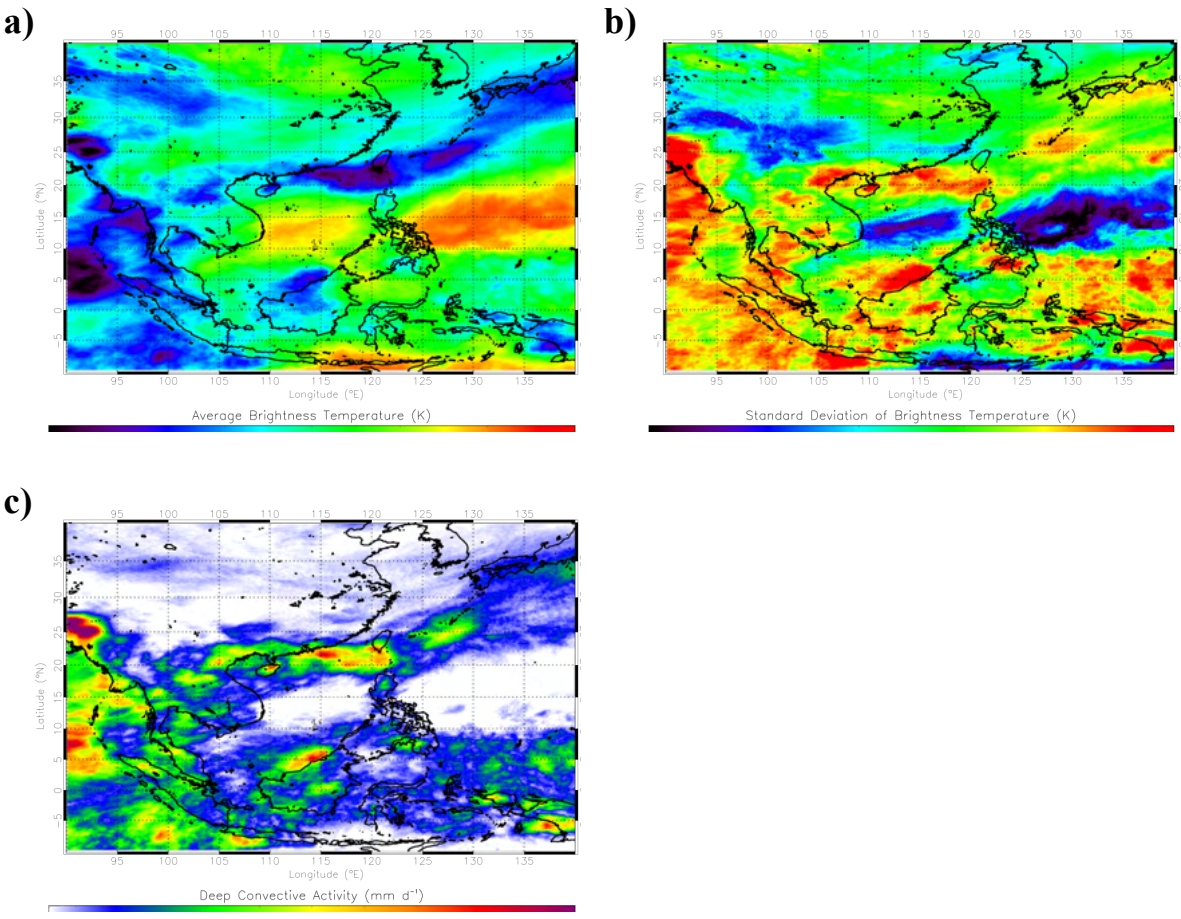

Figure 4.9 Averages of infrared satellite parameters indicative of convection for the "PD3" period (1-10 June 1998). In general, lower brightness temperature averages in (a), higher brightness temperature standard deviations in (b), and higher deep convective activity values in (c) all suggest increased convective activity over tropical oceanic regions.

5) The "PD3" period, 1-10 June 1998

The third stationary phase of monsoon convection during the MYJN period occurred over 1-10 June (hereafter the "PD3" period). As in PD1, a belt of relatively low average brightness temperatures extends across the region (Figure 4.9a), extending from the Bay of Bengal through the northern SCS and south of Japan. Higher average brightness temperatures return to the central SCS, suggesting little convective activity during PD3. High values of brightness temperature variance extend nearly west-to-east across the northern SCS, and are confined to the

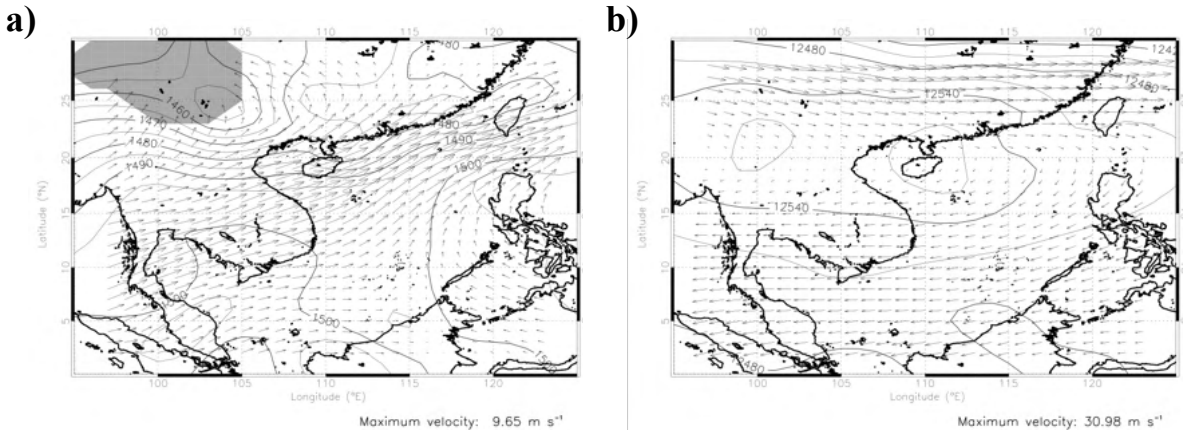

Figure 4.10 Average geopotential heights and winds at (a) 850 hPa and (b) 200 hPa during the "PD3" period (1-10 June 1998). Areas shaded in gray in (a) indicate where the 850 hPa level is below ground.

area north of 18ºN (Figure 4.9b). The DCA pattern is remarkably similar (Figure 4.9c), with values above 15 mm d^{-1} extending along the southern China coast to the island of Taiwan. Maximum DCA values exceeding 40 mm d^{-1} suggest more intense and/or persistent convection over the northern SCS during PD3 (as compared to PD1).

As expected, the average 850 hpa winds (Figure 4.10a) match well with the pattern of convective activity over the SCS during PD3. Strong low-level southwesterly flow returns to the northern SCS, increasing low-level moisture flux and enhancing convective development. The increasing intensity of the monsoon low over the Himalayan Plateau is also notable. At 200 hpa (Figure 4.10b), the tropical anticyclonic circulation dominates the region south of 25ºN, with relatively light upper-level winds over the SCS.

6) Discussion and comparisons of subperiods

Subperiods PD1-PD3 were selected in an attempt to isolate the quasi-steady segments of the 1998 summer monsoon progression. There are two points that should be emphasized from the

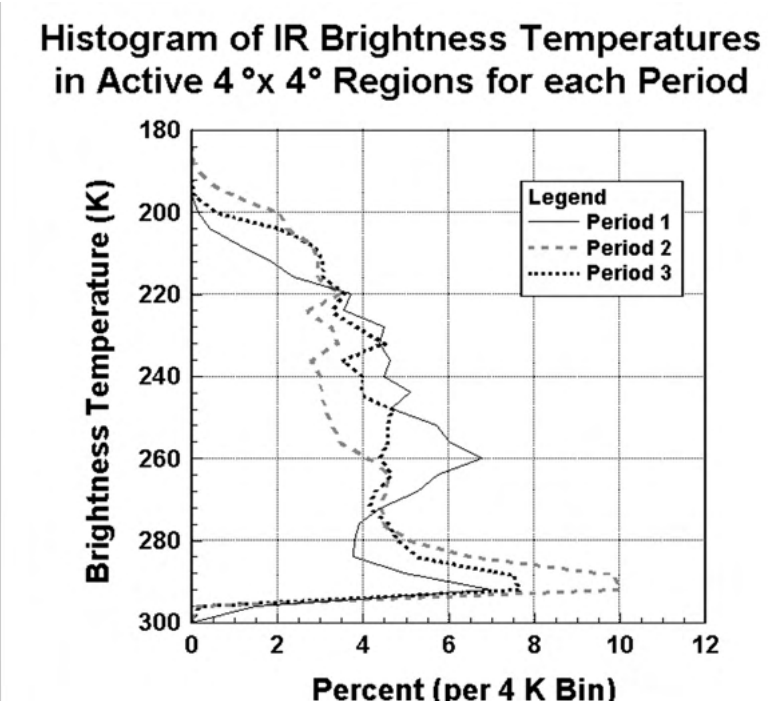

Figure 4.11 Distribution of infrared brightness temperatures over the most convectively active 4ºx4º region during each of the predefined subperiods. Brightness temperatures are on the ordinate axis as they are related to height in the atmosphere. Percent of occurrence is displayed in 4 K bins for continuity.

previous subsections that speak of the success of PD1-PD3 subdivison. First, the pattern of convective activity in each subperiod is unique and can be easily related to quasi-steady regimes of lower-level southwesterly flow. Second, the convection during each subperiod is generally confined to a bounded area within the SCS region of interest. In this manner, the individual diurnal signals of convective activity in each subperiod can be compared to the entire MYJN period. This would aid in determining how the subperiod signals combine to generate the MYJN signal, and in ensuring repetitiveness among subperiods.

It is interesting to compare the convective patterns among the different subperiods. Although the minima of average brightness temperatures in the SCS are similar in PD1-PD3, the spatial distribution of brightness temperatures is markedly different in PD2, with several discrete minima over open ocean as compared to a continuous band. PD2 also appears to encompass the most

intense convection, as it is associated with the highest values of DCA. Figure 4.11 supports this by showing the distribution of brightness temperatures in the most active region for each subperiod. Each distribution was calculated over a 4º x 4º box centered over the maximum value of DCA for said period. PD2 had the highest occurrence of cold cloud tops (< 208 K), while PD1 had the least. This is consistent with the findings of Johnson and Ciesielski (2002), who found relatively weak instability over the northern SCS during PD1. Also of note is the bimodal distribution evident in PD1, with maximum occurrence centered over 260K, representing approximately the 400 hpa level, and 290K, representing surface emissions. This suggests that the pattern of cloudiness in PD1 is fundamentally different than in the other subperiods, a result possibly caused by the midlatitude influences on convective development during PD1, and/or the remnant cool waters over the northern SCS from the previous winter.

Chapter 5: The Diurnal Cycle of Convection over the South China Sea

As mentioned in the introduction, many authors have found a significant diurnal cycle of convective activity over various oceanic regions of the world. Several authors (e.g. Nitta and Sekine 1994; Ohsawa et al. 2001) have focused on the region around tropical Asia, and concluded that a significant convective diurnal cycle also exists in the South China Sea (SCS). Considering areal extent of high cloudiness as a proxy for convective activity, a significant diurnal cycle was evident over the SCS during the period 1 May—30 June 1998 (see figure 3.2). Thus, it is advantageous to detail the specific characteristics of the diurnal cycle of convection over the SCS during 1998, using the wealth of high-resolution data available. This chapter will discuss these characteristics, by first examining the general aspects of the diurnal cycle over the entire northern and central SCS region, and then focusing on the fine-scale structures evident in the diurnal cycle during the subperiods mentioned in Chapter 4.

a. General characteristics of the 1998 SCS convective diurnal cycle

Figure 5.1 depicts the diurnal cycle of infrared brightness temperature over the SCS region during the MYJN period (15 May—14 June 1998, Chapter 4). To construct Fig 5.1, infrared brightness temperatures for all of the data points located over water and within the bounds of 10-25ºN, 110-120ºE are averaged for each available satellite frame. These average brightness temperatures are then composited by the hour of day, meaning all 0000 LST values are averaged into one composited 0000 LST result, etc. (see Chapter 3 for more details about composite

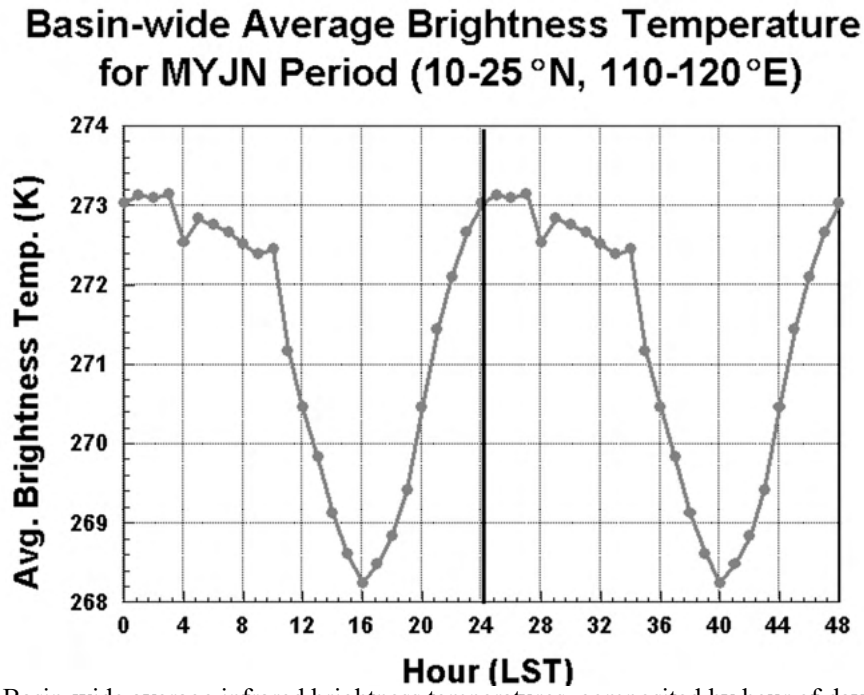

Figure 5.1 Basin-wide average infrared brightness temperatures, composited by hour of day, for the MYJN time period and over the region bounded by 10-25ºN, and 110-120ºE. The composite hourly averages are displayed using local solar time, and the cycle is repeated twice for the sake of clarity.

analysis). It is assumed that infrared brightness temperature can be a proxy for convective activity, as deep convective clouds are the main contributor to depressed values of infrared brightness temperature. Small kinks evident in the curve are likely due to missing data and not variations in the data itself. Fig 5.1 clearly shows that the average infrared brightness temperature does vary over the entire SCS on a diurnal time scale. The minimum average brightness temperature, indicative of increased cloudiness and perhaps greater convective activity, occurs around 1600 LST. The variation is somewhat sinusoidal in nature, with an approximately constant maximum value between 0000-0900 LST.

To ensure factors other than cloudiness are not influencing the diurnal cycle of brightness temperature evident in Fig 5.1, the average diurnal cycle of "clear-air emissions" is presented in

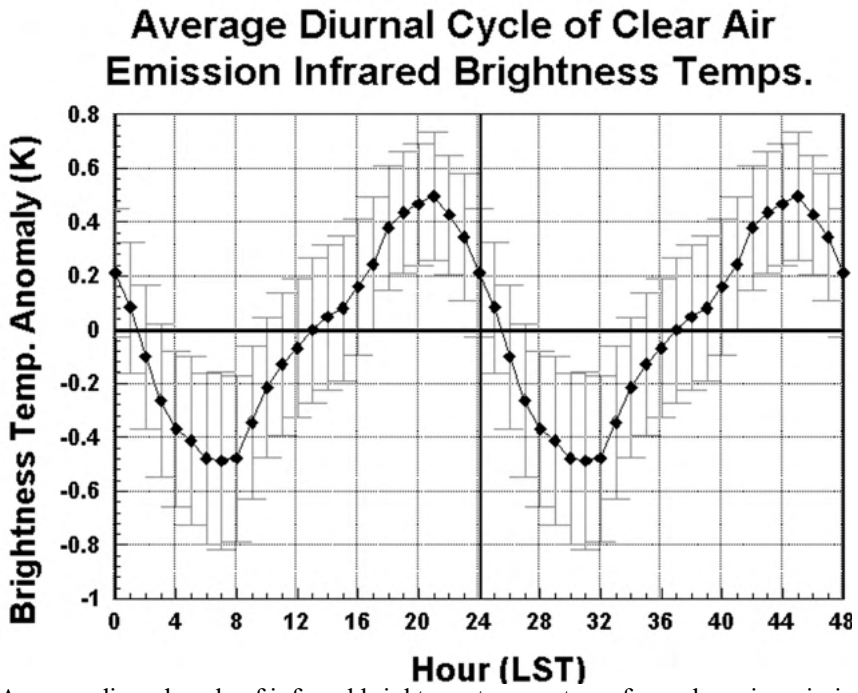

Figure 5.2 Average diurnal cycle of infrared brightness temperatures from clear air emissions. The average brightness temperature was removed from each clear-air pixel, and the anomaly time series from all pixels were then averaged to create the graph above. Error bars show 95% confidence intervals for each average hourly value, based on 30 degrees of freedom.

Figure 5.2. A 24-hour time series of brightness temperatures is said to be derived from clear-air emissions if it has a low standard deviation (< 5 K) with only mild hourly fluctuations (< 5 K hr^{-1}). To construct Fig 5.2, all of the qualifying 24-hour time series, taken from data points used in Fig 5.1, are composited by the hour of day. 95% confidence intervals, based on 30 degrees of freedom, are included in Fig 5.2 to show the statistical significance of the clear-air emission diurnal cycle. While significant, the diurnal variation in clear air emissions cannot account for the average brightness temperature variation, as the amplitude of the clear-air variation in Fig 5.2 is significantly smaller (1 K as compared to 5 K) and out of phase (almost in quadrature) with the variation found in Fig. 5.1. Thus, it appears as if clouds are indeed the major contributor to the diurnal cycle of brightness temperature.

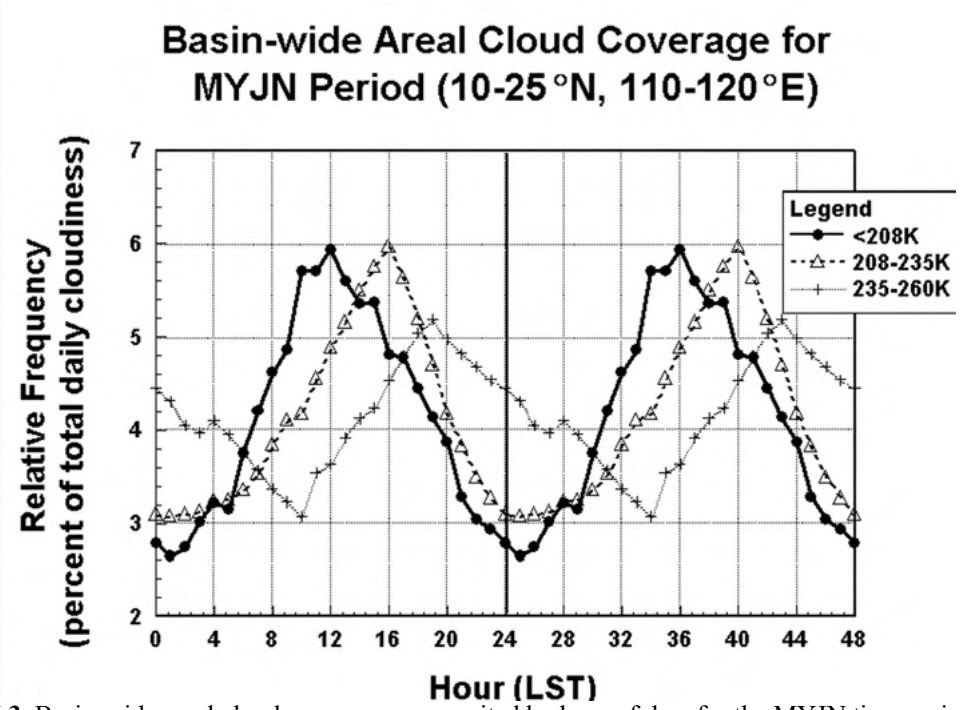

Figure 5.3 Basin-wide areal cloud coverage, composited by hour of day, for the MYJN time period and over the region bounded by 10-25ºN, 110-120ºE. The values displayed above are relative frequencies, found by considering the total daily areal cloud cover in each brightness temperature category. The relative frequencies are displayed using local solar time, and the cycle is repeated twice for the sake of clarity.

To examine how clouds at different levels in the atmosphere contribute to the diurnal cycle of brightness temperature, Figure 5.3 examines the diurnal cycle of areal cloud coverage in three brightness temperature ranges. Fig. 5.3 involves the same period and region as Fig. 5.1. For each brightness temperature range, the areal coverage of cloudiness with brightness temperatures within said range is composited by the hour of day. These composited values are then divided by the total sum of cloud coverage within said range to achieve an hourly composite relative frequency.

The coldest range of brightness temperatures, indicative of deep convective cloudiness, has a maximum relative frequency at around noon local time (Fig. 5.3), and a minimum relative frequency around midnight. Fig. 5.3 would suggest that the maximum of the deepest convective

cloudiness occurs a few hours before the minimum in brightness temperature (Fig 5.1), illustrating the time lag that is inherent in studies of brightness temperature alone (e.g. Mapes and Houze 2003a). Successively warmer ranges have maximum cloud coverage at successively later hours of the day, with 208-235 K peaking at 1600 LST, and 235-260 K at 1900 LST. This behavior has been documented by other authors, and has been attributed to two possible causes. One idea, forwarded by Sui et al. (1997) and Yang and Slingo (2001), is that distinct cloud populations are responsible for the differing high- and low-level cloudiness frequency maxima. They speculate that nocturnal mesoscale convective systems (MCSs) are responsible for the peak in cold convective cloudiness in their studies, while afternoon convective showers, extending only into the mid-troposphere, cause a secondary peak in lower-level cloudiness. The other idea is that the phasing of maximum frequencies evident among brightness temperature ranges is a result of the life cycle of MCSs themselves (Mapes and Houze 1993; Chen and Houze 1997). The cloud shield of an MCS tends to warm and expand horizontally through its evolution (e.g. Churchill and Houze 1984; Lilly 1988), which would cause the phasing in question.

Figure 5.4 attempts to address this issue by examining the diurnal cycle of cloudiness, over the same period and region as Fig. 5.3, in narrow bins instead of 30 K or greater ranges. Called an evolution histogram (see Chapter 3 for details), Fig 5.4 succinctly displays the frequency of occurrence of cloud-top temperature (within 4 K intervals) over the entire range of possible brightness temperature values. In this manner, the diurnal cycle of frequency for all cloud-top heights can be displayed in one figure. The values displayed in Fig. 5.4 are actually frequency anomalies, found by subtracting the daily mean histogram of brightness temperature from the individual hourly histograms. Frequency anomalies are able to more clearly capture the essence of the diurnal cycle; positive values indicate cloudiness of a given brightness temperature bin is more frequent than its average daily occurrence.

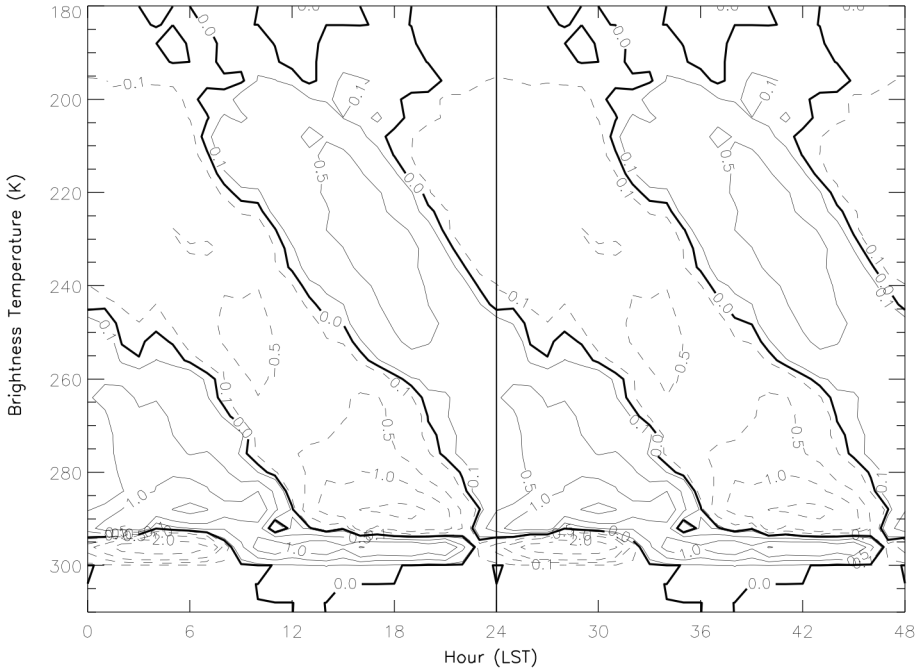

Figure 5.4 Basin-wide evolution histogram for the MYJN time period and over the region bounded by 10-25ºN, 110-120ºE. The values shown above are percentage anomalies, found by subtracting the daily mean histogram of brightness temperature from hourly histograms. Positive anomalies indicate when cloudiness of a given brightness temperature is more frequent than its average daily occurrence.

It is apparent in Fig. 5.4 that the coldest cloud tops (< 200 K) are most frequent over the SCS region around 1100 LST. The disorganized nature of percentage anomaly values in the region colder than 190 K suggests that there is not enough data beyond this point to draw any useful conclusions. After the peak in coldest cloud top occurrence, there is a coherent pattern in which progressively warmer brightness temperature bins achieve a maximum frequency anomaly at successively later times in the day. For example, the maximum occurrence at 210 K is around 1400 LST, increasing to 1900 LST by the 250 K bin. The continuous nature of the percentage perturbation between 1000 and 2000 LST suggests that the diurnal cycle is being most influenced by the life cycle of MCSs in the region, as in Chen and Houze (1997).

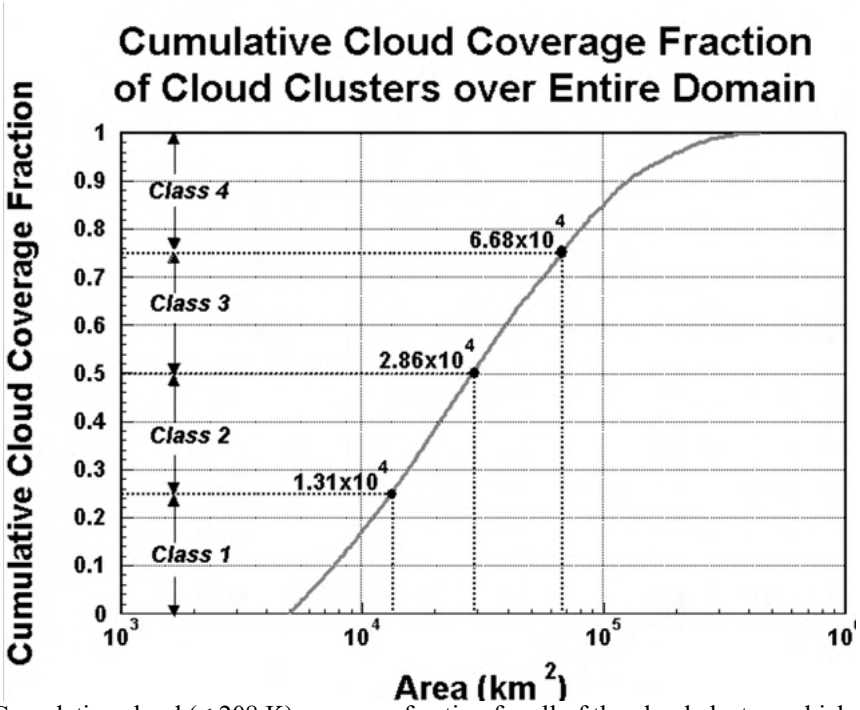

Figure 5.5 Cumulative cloud (< 208 K) coverage fraction for all of the cloud clusters which occurred in the satellite domain. Cloud clusters are categorized by areal extent, based on their contribution to total cold cloud coverage, with an increasing class number indicating a larger size. By definition, class 1 cloud clusters are smallest and account for 25% of the total cloud cluster area, class 2 the next 25%, etc.

The life cycle of MCSs in the SCS region can be better understood through time cluster analysis (see Chapter 3 for more details on this technique). With time cluster analysis, the individual cold cloud shields of MCSs (< 208 K) can be traced through their entire existence. In doing so, useful characteristics about the initiation, maximum areal extent, dissipation, duration, and propagation direction can be obtained. To facilitate discussion, the population of time clusters that existed in the SCS region during the MYJN period is subdivided according to maximum size achieved by a time cluster. These subdivisions are based on the cumulative cold cloud coverage of all cloud clusters, as shown in Figure 5.5. For example, class 1 cloud clusters are defined as being smallest, and the sum of their areas contributes 25% to the total areal coverage of all cloud clusters. Class 2 cloud clusters are the next largest size and constitute the second quartile of total areal coverage, etc. The size boundaries for each quartile occur at areas

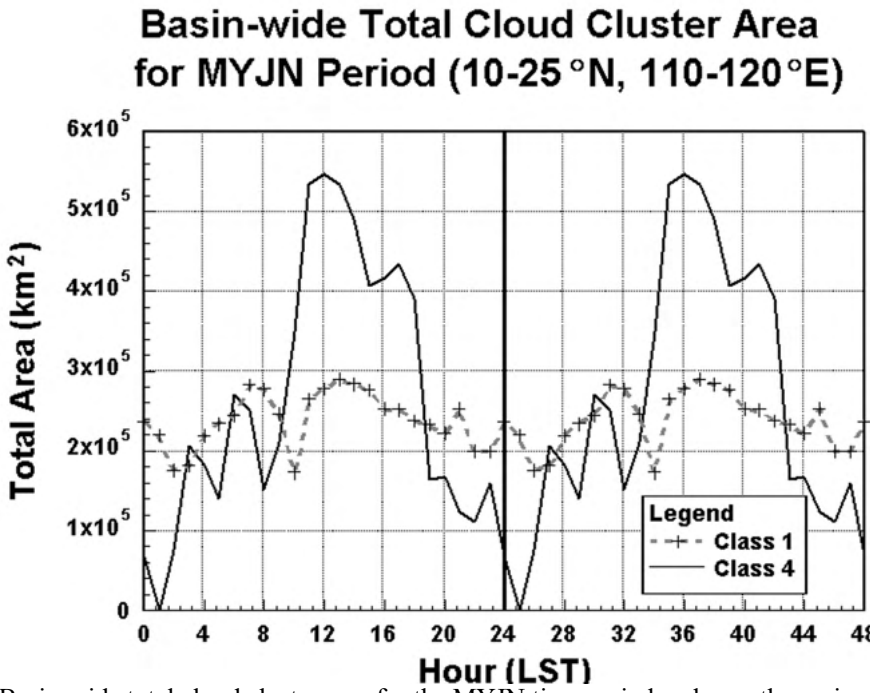

Figure 5.6 Basin-wide total cloud cluster area for the MYJN time period and over the region bounded by 10-25ºN, 110-120ºE. The total composite hourly areas of the largest (class 4) and smallest (class 1) quartiles of cloud clusters, as defined in Fig. 5.5, are displayed above.

of 13,100, 28,600, and 66,800 km^2. The corresponding circular radii to these area thresholds, given by

$$r = \sqrt{area / \pi}\,, \tag{5.1}$$

are 36, 54, and 82 km, respectively. It is interesting to note that these size thresholds suggest a population of smaller cloud clusters over the SCS in 1998, as compared to those studied over the western tropical Pacific (e.g. Chen and Houze 1997).

Figure 5.6 depicts the diurnal cycle of total cold cloud area for the smallest and largest size classes defined in Fig. 5.5. While the phase of the diurnal cycle is similar for both size classes,

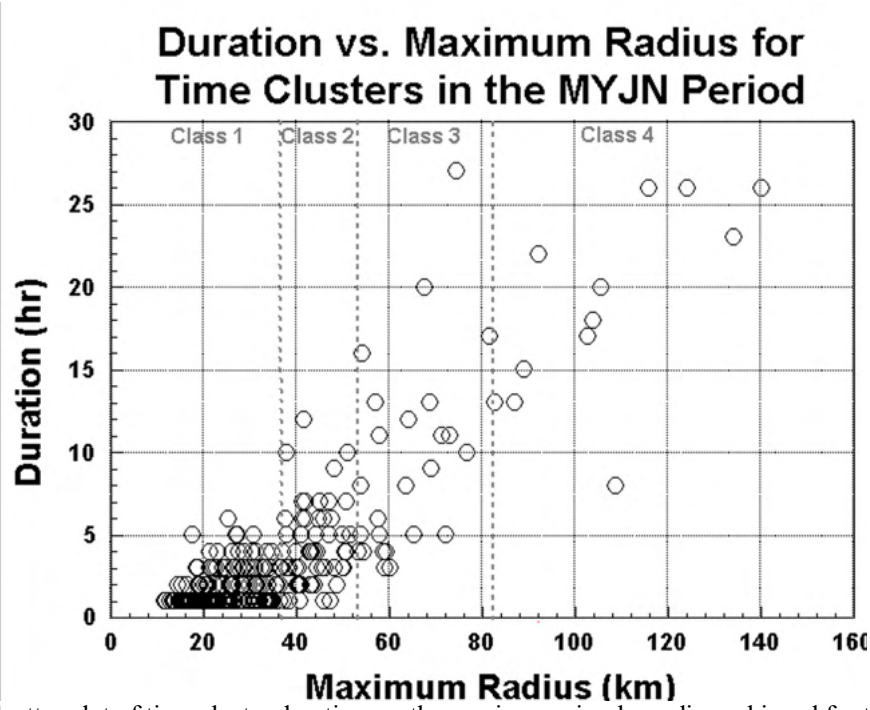

Figure 5.7 Scatter plot of time cluster duration vs. the maximum circular radius achieved for time clusters in the SCS region during the MYJN period. The maximum radius is simply (maximum area/π)$^{1/2}$. The size thresholds separating the four classes (defined in Fig 5.5), expressed as radii, are illustrated with dashed lines.

the amplitude is very dependent on the size of cloud cluster being considered. The smallest class of cloud clusters has a very small amplitude of diurnal variation, while the largest class has a much stronger variation with peak coverage around noon and a minimum around midnight. This size dependence on the amplitude of diurnal variation has been documented by other authors (e.g. Mapes and Houze 1993; Chen and Houze 1997; Zuidema 2003), and suggests that the largest cloud clusters are most responsible for the determining the observed diurnal cycle of convection over the SCS region.

Although the phase of maximum cold cloud cover is similar for the largest and smallest time cluster classes, the typical evolution of large and small convective systems are quite different. Figure 5.7 exemplifies this by displaying the scatter of time cluster duration as a function of the

maximum areal extent achieved during its lifetime. It is apparent that class 1 time clusters have a relatively short duration; over 80% of these clusters are tracked for only one hour. Duration generally increases with increasing maximum size, such that almost every class 4 cloud cluster is tracked for more than 12 h. The direct duration-size relationship is approximately linear, with a noticeable spread that can be partially attributed to the chaotic nature of mergers and splits within a time cluster's evolution.

Naturally, the life cycle of each convective system (time cluster) includes initiation, growth, and dissipation. Systematic diurnal behavior of these stages of evolution, such as systems forming at the same time each day, can have a profound effect on the diurnal cycle of convective activity. Figure 5.8 shows the diurnal development characteristics for the smallest two classes of time clusters, in terms of the hourly frequency of their a) initiation, b) maximum size, and c) dissipation. Small time clusters preferentially form during the late morning and early afternoon hours (Fig. 5.8a). The distribution of time of maximum areal extent (Fig 5.8b) looks very similar to the distribution of initiation times. This is expected, as small systems were shown to have a short duration (Fig. 5.7), and thus they evolve relatively quickly. Small systems tended to dissipate most frequently in the early through late afternoon hours (Fig 5.8c), a few hours after the preferential initiation time. The diurnal development characteristics of small time clusters in Fig 5.8, with systems preferentially forming and decaying in the afternoon hours, matches well with the afternoon maximum of cloud area for small systems in Fig 5.6.

In contrast, the development characteristics of the largest two classes of systems are more complex (Figure 5.9). Large systems have two preferred initiation times; the most obvious is around 1800 LST, with a secondary peak between 0300-0600 LST (Fig 5.9a). The reason for this bimodal distribution is not clearly understood, but may be a result of the relatively small sample

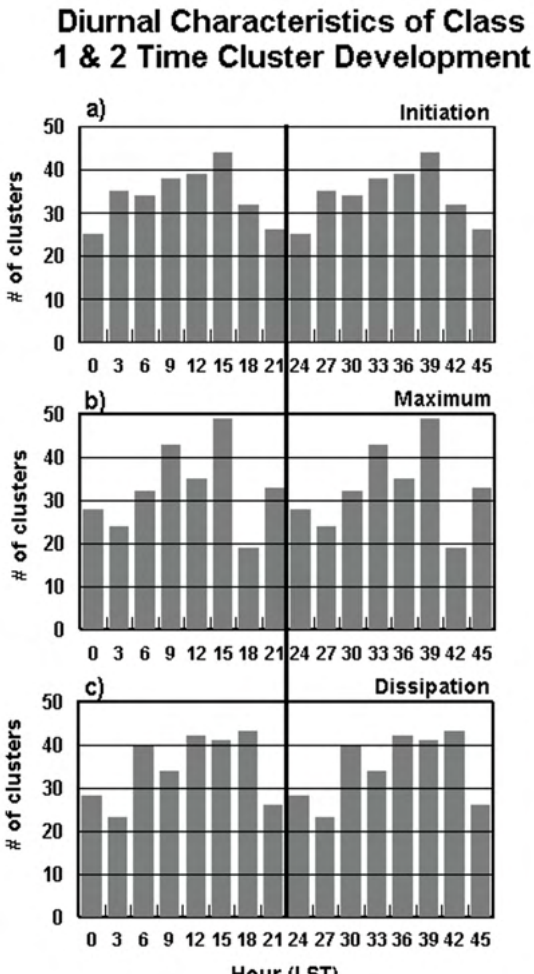

Figure 5.8 Composite frequency distribution of time clusters at the time of a) initiation, b) maximum areal extent, and c) dissipation for the smallest two classes of time clusters.

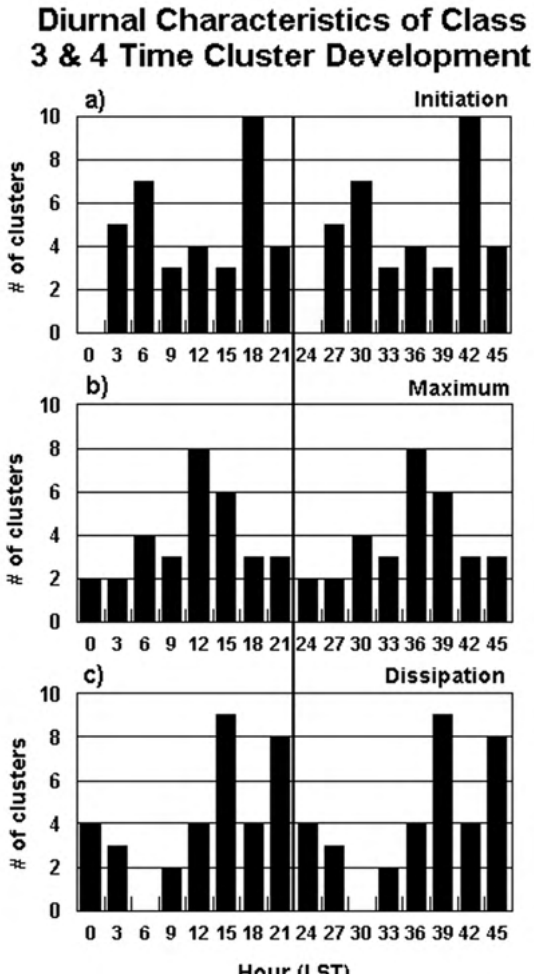

Figure 5.9 Composite frequency distribution of time clusters at the time of a) initiation, b) maximum areal extent, and c) dissipation for the largest two classes of time clusters.

size. Regardless, there is a clear preference for large time clusters to achieve a maximum size between 1200-1500 LST (Fig 5.9b). Large systems were most likely to dissipate between 1500-2100 LST (Fig 5.9c), several hours after the peak frequency of maximum size. The longer life cycles of large systems suggested by Fig. 5.9 is consistent with Fig 5.7, and the greatest frequency of maximum size in Fig 5.9b agrees with the afternoon maximum of large system cloud area in Fig 5.6.

It is evident, considering averages over the entire SCS region, that the maximum of convective activity occurs in the early afternoon hours. However, it is not immediately clear if the whole region has the same phase of maximum convective activity, or if only the most active parts of the region are skewing the average results. To determine the prevalence of this afternoon maximum of convection across the SCS region, empirical orthogonal function (EOF) analysis is employed. In this case, EOF analysis is applied to the 24 h composite time series of infrared brightness temperatures, calculated over the MYJN period, for satellite data points within the SCS region (10-25ºN, 110-120ºE). A grid spacing of 0.25º x 0.25º is used to facilitate the computationally expensive EOF analysis procedure, and only grid points located over water are included in the analysis. The use of composite time series will only allow the detection of variations with periods of one day or less.

Figure 5.10 presents the results of the EOF analysis, and includes the spatial patterns of the leading (Fig 5.10a) and second (Fig 5.10b) EOFs, the principal component time series of the leading and second EOFs (Fig 5.10c), and the variance explained by the EOFs (Fig 5.10d). First, the variance explained by the leading and second EOFs suggests that they are well separated and statistically significant. Error bars, depicting the uncertainty in the measure of variance explained, are determined using the equation

$$s_e = s\sqrt{2/N^*}\,, \tag{5.2}$$

where s_e is the variance error, s is the variance explained, and N^* is the effective degrees of freedom. In this case, N^* is chosen to be 120, as that is the approximate number 1º x 1º boxes used in the analysis. North et al. (1982) suggest that Eq. 5.2 provides a 95% confidence interval

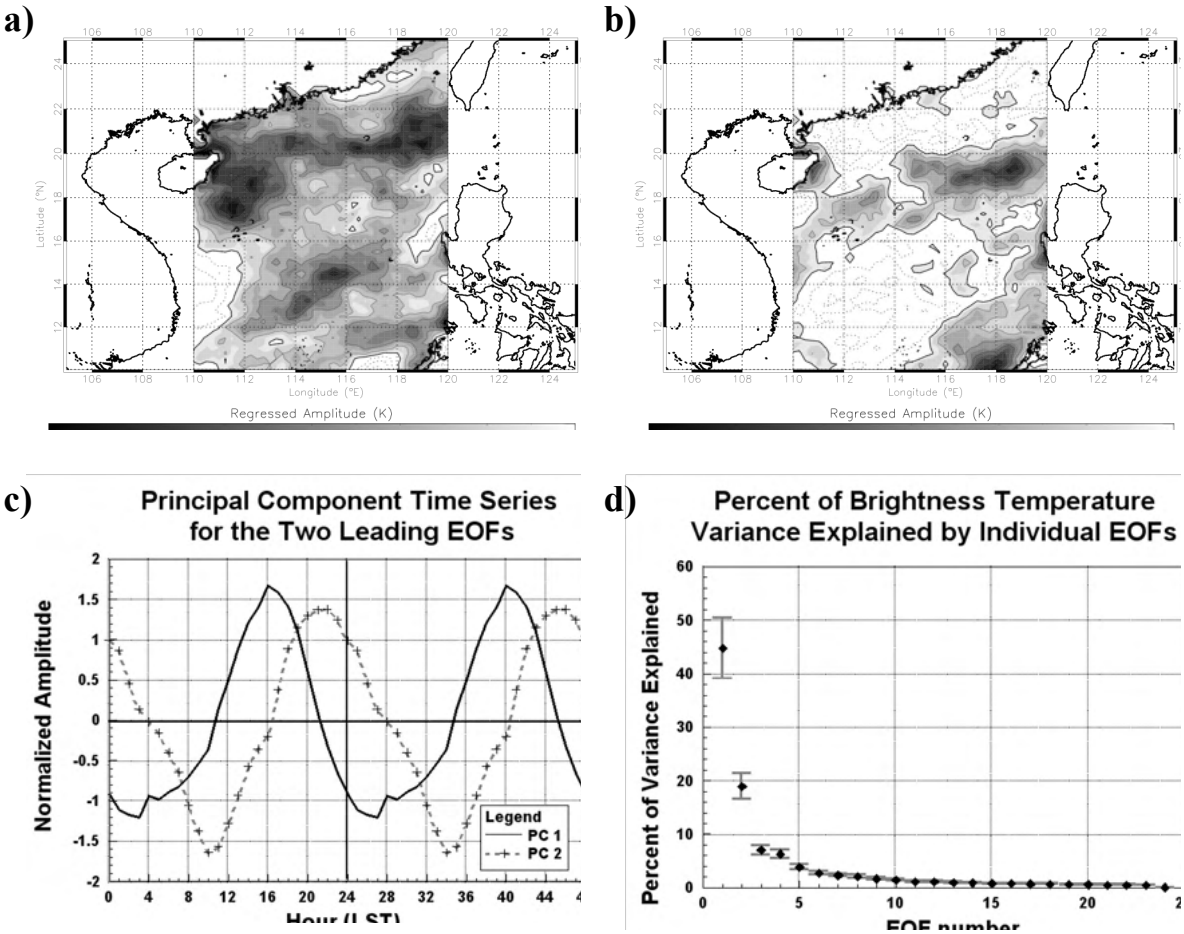

Figure 5.10 Results of the EOF analysis of 24 h composite brightness temperatures, calculated for the MYJN period and for grid points across the SCS region. Figures (a) and (b) show the spatial patterns of the leading and second EOF, respectively. Contour intervals are 0.5K in both (a) and (b), and negative values are shaded (as negative anomalies of brightness temperature should correspond with positive anomalies of convective activity). Figure c) provides the principal component time series for the leading and second EOFs. The variance explained by all EOFs, shown in Figure d), verifies that the first two EOFs are well-separated.

for the actual variance explained by an EOF. Additionally, an EOF is said to be well separated if its error bars do not overlap with any other EOF. Thus, it is clear that the first and second EOFs are very well separated from the rest of the pack, even with a more conservative choice of N^*. Another interesting point is that the principal component time series of the leading and second EOF (Fig 5.10c) both have a period of one day. Consequently, Fig 5.10d indicates that the diurnal variation accounts for 65% of the variability in the composite brightness temperatures

(considering only the variations with a period of a day or less).

EOF analysis determines the coherent spatial patterns which best explain the variance in an input data set. The leading pattern of spatial variability in the composite brightness temperature data is shown in Fig. 5.10a, which was constructed by regressing the composite brightness temperature time series against the leading principal component time series (PC1) in Fig 5.10c. Shading in Fig 5.10a represents the area in which the brightness temperature anomaly is out of phase with PC1, and unshaded regions vary in phase with PC1. The level of convective activity is inversely proportional to brightness temperature, so shaded regions in Fig 5.10a should be more convectively active than average when PC1 is positive. A vast majority of the region depicted in Fig 5.10a is shaded, which indicates that the diurnal cycle of convection over most of the SCS region is at least somewhat in phase with PC1. In fact, PC1 is almost exactly an inverted version of the composite brightness temperature curve in Fig 5.1, adding to the significance of the findings.

It is interesting to note that the most negative values in Fig 5.10a extend in a line approximately parallel to the southeastern China coast, and are a few hundred kilometers off shore. This is likely a result of a diurnal cycle with a larger amplitude than in surrounding regions, and with a phase that closely matches PC1, as both factors would cause the increased regressed values.

The second EOF, whose spatial pattern is depicted in Fig 5.10b, provides more information about the diurnal cycle across the region. As with PC1 and Fig 5.10a, areas that are shaded in Fig 5.10b are likely more convectively active when the second principal component time series (PC2) is positive. A noticeable pattern exists in PC2 with positive regressions near the China coastline,

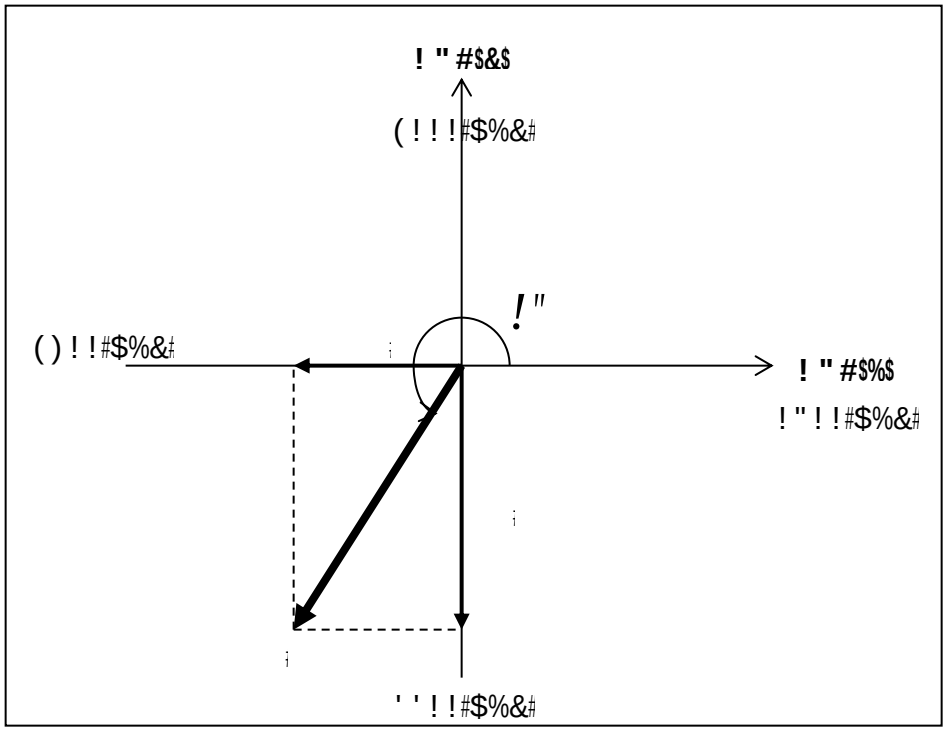

Figure 5.11 Schematic diagram which depicts the process of finding the true phase (*!*) and regressed amplitude ( ) of the diurnal cycle of infrared brightness temperature, given the regressed values of infrared brightness temperature from the leading and second EOF as shown in Fig 5.10.

but negative regressions several hundred kilometers south of the coast. This pattern would suggest that convection is more likely near the coast in the late morning hours, when PC2 is negative. Farther from the coast, convection is more likely in the late evening hours, when PC2 is positive.

This point can be further developed by combining the information from Figs 5.10a-c in one succinct manner. By definition, each EOF-PC set is orthogonal to all of the other sets. It is also true that PC1 and PC2 are the only two variations from the EOF analysis with a period of exactly one day. As mentioned earlier, the values shown for the leading and second EOFs are derived by regressing the composite brightness temperature time series against PC1 and PC2, respectively. Since PC1 and PC2 are orthogonal, it is possible to find the actual regressed amplitude and phase

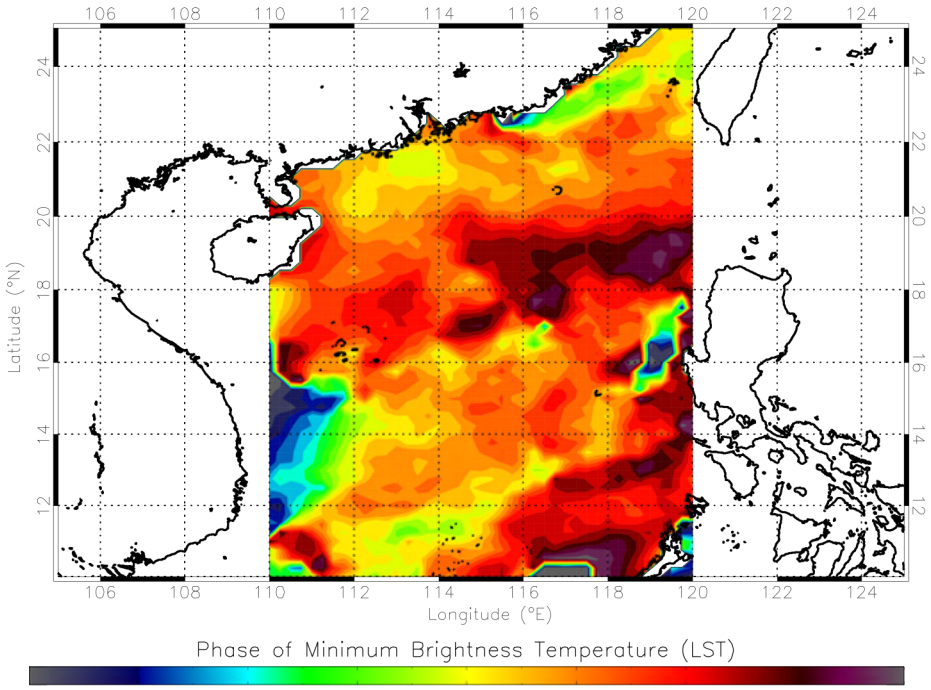

Figure 5.12 The hour (LST) of the minimum in the diurnal cycle of infrared brightness temperature for data points in the EOF domain. This is also assumed to be the hour of the maximum convective activity. Values were calculated using the results in Figs. 5.10a-c and the procedure illustrated in Fig. 5.11.

of the diurnal variation by using the regressed values from the leading and second EOF as basis vectors. This procedure is shown schematically in Figure 5.11, and can be repeated for the composite brightness temperature time series at each grid point in the domain. If, for example, a composite time series regresses positively onto PC1 but not at all onto PC2, that composite time series is exactly in phase with PC1. PC1 is at a minimum around 0400 LST, so the minimum brightness temperature (and implied convective maximum) of the example composite time series would also be 0400 LST. When composite time series regressions onto both PC1 and PC2 are non-zero, the phase angle θ shown in Figure 5.11 can be determined to find the true phase of the brightness temperature minimum (and implied convective maximum).

Figure 5.12 displays the phase of the minimum in the diurnal cycle of brightness temperature, for all of the grid points in the EOF analysis, using the procedure illustrated in Fig. 5.11. As anticipated, a general pattern exists near the southeastern China coast where the hour of minimum brightness temperature, and presumably the hour of maximum convective activity, increases with increasing distance from the coastline. The hour of minimum brightness temperature is in the late morning hours near the coast, and gradually increases to the late evening hours around 600 km from the coast, where the signal disappears. The same coherent pattern extends along the entire length of the coast contained in the EOF analysis domain. This pattern, which can be described as a systematic variation in the phase of the diurnal cycle of convection with a coherent spatial structure, is defined as a propagation signal (see Chapter 3 for more details), and will be explored further in the remainder of this chapter.

So far, only the general characteristics of the diurnal cycle of convection for the entire SCS region have been explored. It was determined that the different indicators of maximum convective activity, including minimum brightness temperatures and maximum cold (< 208 K) cloud coverage, indicate an early afternoon maximum across the SCS region. Time cluster analysis suggests that this afternoon maximum can be most attributed to the life cycle of the largest convective systems, which has also been shown by other authors (e.g. Mapes and Houze 1993; Chen and Houze 1997; Zuidema 2003). EOF analysis shows that the afternoon maximum of convective activity was prevalent across most of the region. However, EOF analysis also implies the existence of a propagation signal near the southeastern China coast. To explore this propagation signal, the time periods PD1-PD3, defined in Chapter 4, will be examined individually to see how the small segments of similar convective behavior add to create the entire MYJN picture.

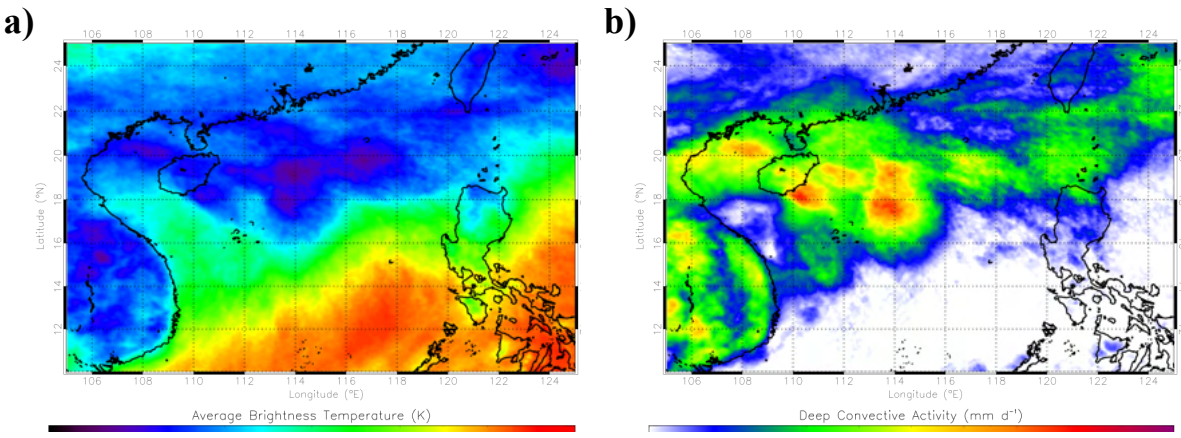

Figure 5.13 Average brightness temperatures (a) and satellite estimated precipitation (b) over the northern and central SCS region during PD1 (15-20 May 1998).

b. The diurnal cycle of convection over the SCS during PD1 (15-20 May 1998)

The first subperiod (PD1; 15-20 May 1998) coincides with the onset of the monsoon over the northern SCS region. PD1 is characterized by a frontal passage during 15 May, followed by several days of nearly continuous convective activity across the same general region. It is also interesting to note that PD1 is the only subperiod that contains a full set of radar data, so important comparisons between satellite and radar representations of the diurnal cycle of convection are necessarily confined to this subperiod.

Figures 5.13a-b depict the spatial distribution of the average infrared brightness temperature and DCA over the PD1 period. The lowest brightness temperature averages, presumably coincident with increased levels of convective activity, stretch in a band that runs approximately parallel to, and several hundred kilometers south of, the southeastern China coastline (Fig. 5.13a). This matches well with the results of Johnson and Ciesielski (2002), who also found a primary rainfall maximum away from the south China coastline during PD1. Johnson and Ciesielski (2002) attributed this to a strong north-south SST gradient across the northern SCS, with

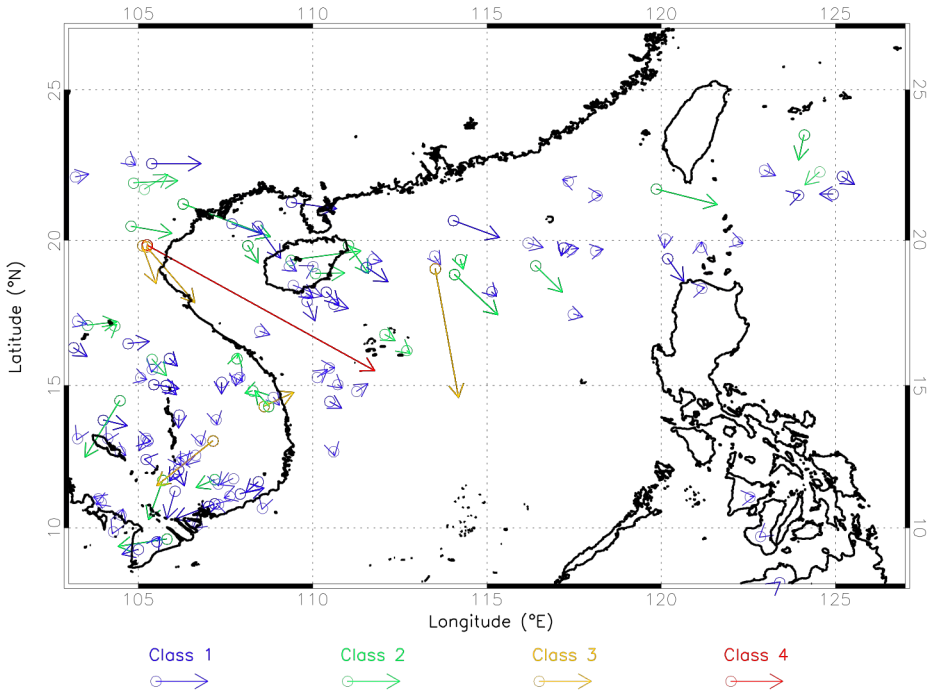

Figure 5.14 Time cluster tracks, which depict the motion of discrete cold convective cloud shields across the SCS region during PD1 (15-20 May 1998). A circle denotes the location that the tracking algorithm first detects a time cluster, while the arrow points to the last detectable location of said cluster.

convective development being preferred in the warmer waters that were farther from the coast. In contrast, the high average brightness temperatures (> 285 K) in the central SCS suggest almost no convection during PD1, as the western Pacific subtropical high had not yet retreated from that area. Fig. 5.13b confirms this, with average daily satellite-estimated rainfall of 10-30 mm d^{-1} in the northern SCS, and negligible amounts in the central SCS.

Figure 5.14 illustrates the paths of time clusters, or the cold cloud (< 208 K) shields associated with MCSs, which occur during PD1. In agreement with Fig. 5.13, most of the time clusters in PD1 were confined to the southeastern Asian mainland, and to a band that extended roughly parallel to (and several hundred kilometers off) the southeastern China coast. Two large systems, one class 3 and one class 4, traversed the northern SCS during PD1. The majority of time clusters over the northern SCS, however, were generally small. The lack of very large cold

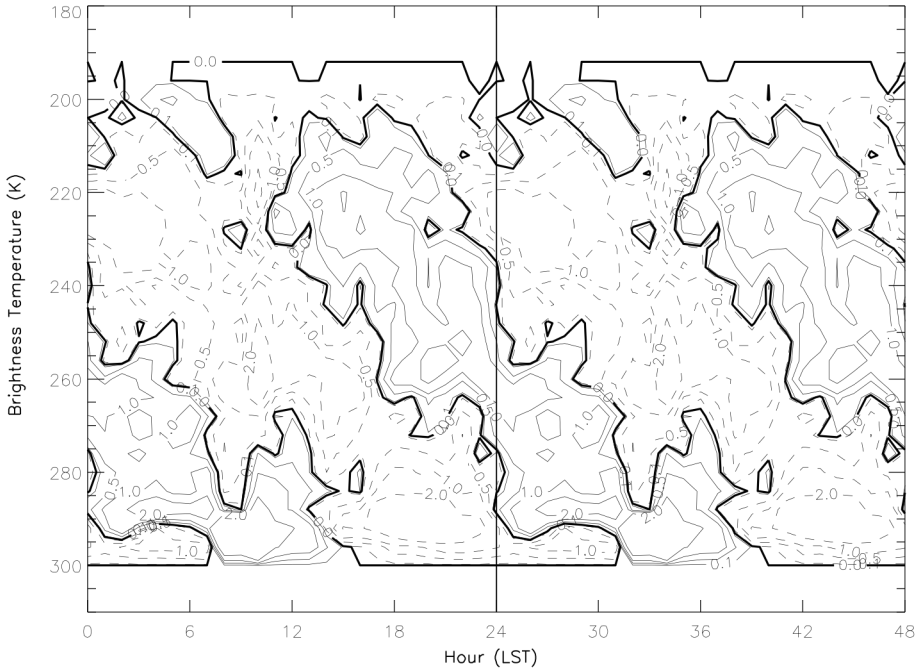

Figure 5.15 Evolution histogram for the PD1 time period and over the region bounded by 18-22ºN, 115-119ºE. The values shown above are percentage anomalies, found by subtracting the daily mean histogram of brightness temperature from hourly histograms. Positive anomalies indicate when cloudiness of a given brightness temperature is more frequent than its average daily occurrence.

cloud shields, as compared to other subperiods, can be attributed to the fact that convection was found to be relatively weak during PD1 (Johnson and Ciesielski 2002), which may have been a result of relatively low CAPE during this onset period.

The evolution histogram of brightness temperatures (Figure 5.15) over the northern SCS during PD1 looks remarkably like the same diagram constructed over the MYJN period (Fig 5.4), although Fig. 5.15 is much more convoluted because in is based on a smaller time period. Fig. 5.15 was created using the satellite data points over water within the range 18º-22ºN, 115º-119ºE. As in Fig 5.4, Fig 5.15 shows a general pattern of cold cloud tops (< 210 K) most frequently occurring in the early afternoon hours, and clouds with successively warmer tops occurring most frequently later in the afternoon and evening hours. Thus, it appears as if the afternoon maximum

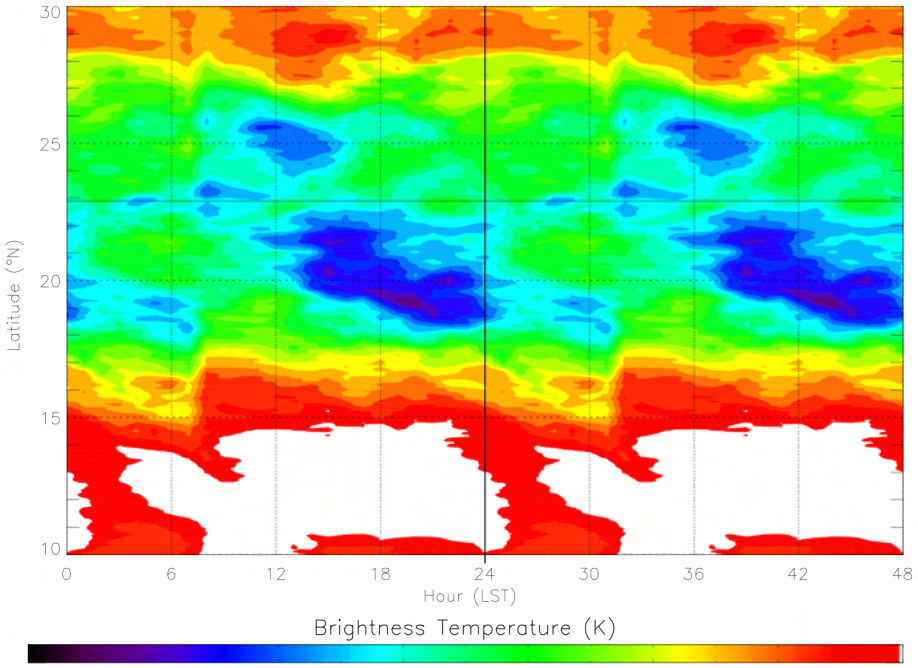

Figure 5.16 Hovmöller diagram depicting the average brightness temperature as a function of latitude and time of day. Only the data within a one-degree longitude swath centered on 117ºE was considered in this analysis. The solid line at 22ºN denotes the location of the China coastline at this longitude.

of convection found to exist over the SCS during the MYJN period also occurs in the convectively active region of the SCS during PD1.

To examine how the phase of the maximum of convective activity varies over the SCS, a Hovmöller diagram of composite brightness temperatures is presented (Figure 5.16). This latitude vs. time diagram is constructed by averaging brightness temperatures from satellite data points in a one-degree longitude swath centered on 117ºE to coincide with the location of Dongsha Island. Fig. 5.16 clearly shows a southward progression of cold brightness temperature anomalies with time. The cold anomaly appears to originate near the latitude of the southern China coast (23ºN) during the mid-morning hours, and shifts south to the latitude around Dongsha Island (20ºN) by the early afternoon. By the early evening hours (2000 LST), the

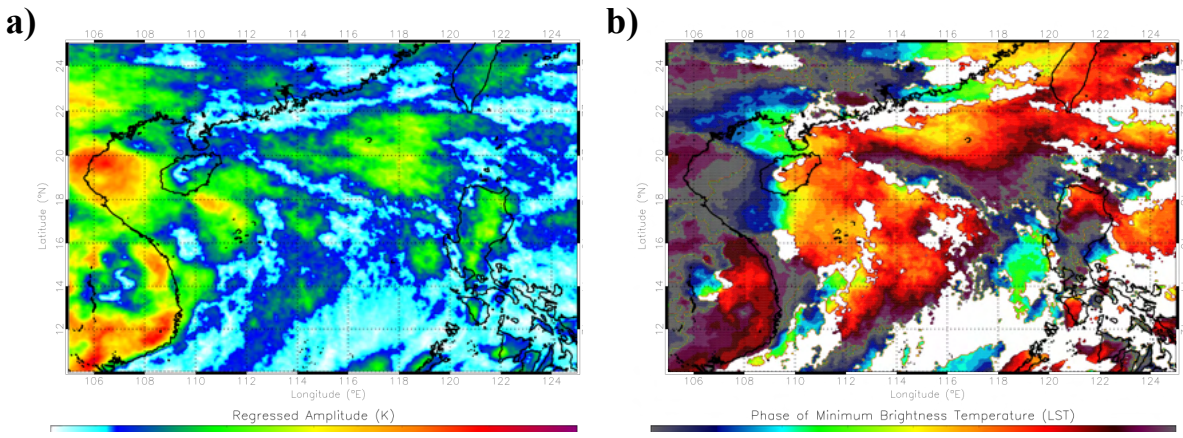

Figure 5.17 Regressed amplitude (a) and phase of minimum (b) in the diurnal composite time series of brightness temperature for PD1. In (a), higher values are indicative of a stronger and more coherent diurnal cycle of brightness temperature. In (b), the times shown correspond to the phase of maximum convective activity as suggested by brightness temperatures, and only data points with significant (> 3 K) regressed amplitudes are displayed.

anomaly has sunk to 18ºN where it becomes difficult to discern. Farther south (e.g. around 16ºS), the signal transitions from diurnal to more semidiurnal in nature, which has been documented by Liberti et al. (2001). In general, Fig. 5.16 suggests the regular formation and southward propagation of cloud systems through the northern SCS in the specified longitude band.

However, this southward propagation is not unique to a single one-degree longitude band. By performing a composite analysis of infrared brightness temperatures at each satellite grid point, maps of the regressed amplitude and phase of the diurnal cycle can be generated. Because of the large number of missing 1000 LST satellite frames during PD1, the composite value for this hour was interpolated as being the average of 0900 and 1100 LST values. In this manner, the strength of the diurnal cycle, as given by the regressed amplitude, can be determined for PD1 (Figure 5.17a). In general, the highest regressed amplitudes are co-located with the lowest brightness temperature averages (Fig. 5.13), as the highest values are found along the Southeast Asian coast and in a band running just south of the China coast. More importantly, the spatial extent of the propagation signal across the SCS during PD1 can be verified by considering the

distribution of the phase of minimum in the diurnal cycle of brightness temperatures (Figure 5.17b). To reduce clutter, only the data points whose diurnal cycle exhibit a regressed amplitude greater than 3K are displayed in Fig. 5.17b. It is clear that the general pattern of increasing time-of-minimum with increasing distance from the China coast exists across a significant portion of the northern SCS. This propagation signal, which is evident to the west of 113ºE and extends up to 500 km off the Southeastern China coast, and is caused by the regular formation and propagation of cloud elements over the same areas and at similar times of day.

Other notable behaviors also exist in Fig. 5.17b. Along the inland side of the Vietnam coast, a band with an afternoon (1700 LST) minimum of brightness temperature is observed, which suggests that convection occurs most frequently here during the afternoon hours. The timing and proximity to the coast suggesting a combination of land surface heating and sea breeze effects as the driving forces behind the convective diurnal cycle in this location. The minimum time of brightness temperatures increases in all directions from this band, up to local midnight a few hundred kilometers off the coast. This is likely caused by the expansion of upper level anvils as the convective systems mature. The increasing time-of-minimum in all directions suggests relatively stationary convective systems in this region. Also of note is the effect that the large class 4 MCS had on the diurnal cycle over the far western SCS, with a propagation signal evident from the Gulf of Tonkin to approximately 17ºN.

While brightness temperatures have been shown to be adequate in capturing the diurnal cycle of cold convective cloudiness in this study, their ambiguity necessitates the consideration of other variables that may be more directly related to convective activity as a basis of analysis. The deep convective activity (hereafter DCA; see Chapter 3 for more details) index is a more appropriate choice, as it has been shown to be correlated with accumulated precipitation in both this study and previous studies of tropical convection (i.e. Hendon and Woodberry 1993). As a reminder,

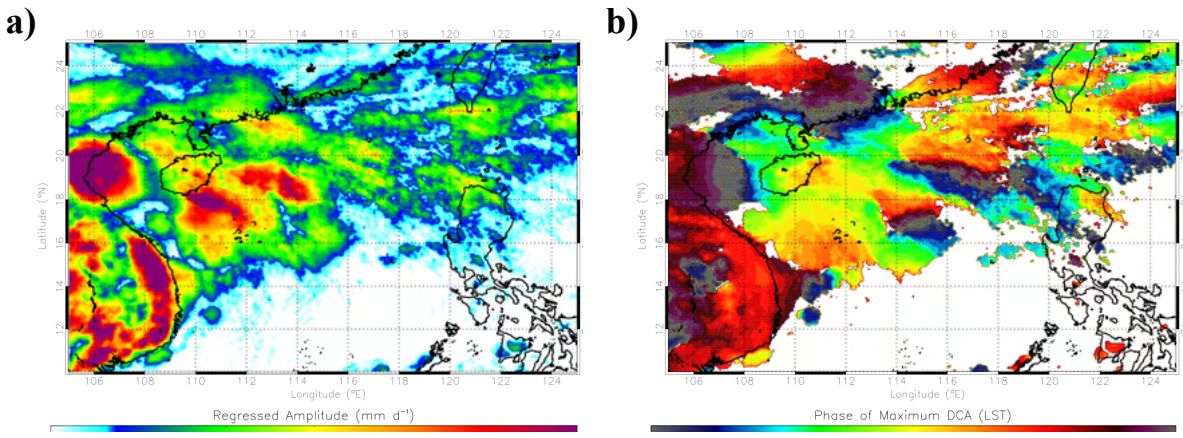

Figure 5.18 Regressed amplitude (a) and phase of maximum (b) in the diurnal composite time series of satellite-estimated precipitation for PD1. In (a), higher values are indicative of a stronger and more coherent diurnal cycle of DCA. In (b), the times shown correspond to the phase of maximum convective activity as suggested by DCA, and only data points with significant (> 3 K) regressed amplitudes are displayed.

the DCA index has a nonzero value for brightness temperatures lower than 230K, gives linear weight to clouds with even colder brightness temperatures, and can be expressed in units of mm d^{-1}.

Figures 5.18a-b show the regressed amplitude and phase of the diurnal cycle, calculated in a similar fashion to Figs. 5.17a-b but using composite time series of DCA. The spatial pattern of the regressed amplitudes of DCA (Fig. 5.18a) is quite similar to Fig. 5.17a, with the exception of the central SCS south of 15ºN where DCA values (and hence regressed amplitudes) were around zero during PD1. The phase of maximum DCA (Fig. 5.18b) also shows the same general pattern as the phase of brightness temperature minimum (Fig. 5.17b). Again, composite time series with a regressed amplitude less than 3 mm d^{-1} are not displayed in Fig. 5.18b to focus on only significant diurnal variations. A noticeable propagation signal for time-of-maximum DCA extends across most of the northern and eastern SCS (between 113º and 118ºE), just as it did in the brightness temperature analysis. Thus, Fig 5.18b would suggest that the propagation signal is being produced, at least in part, by colder clouds typically associated with convection (< 230 K).

Up to this point, the analysis of the diurnal cycle of convection during PD1 has been based on infrared satellite brightness temperatures, which are only an indirect measure of the level of convective activity. However, complete reflectivity and estimated precipitation datasets for PD1 are available from the BMRC C-POL Doppler radar located on Dongsha Island (see Chapter 2 for more details). These datasets consist of variables that are better associated with the level convective activity, as compared to satellite brightness temperatures. In the same manner, composite analyses of the radar datasets should provide a more direct measure of the diurnal cycle of convection within the radar domain. The results from the radar analyses can be compared to those from satellite analyses to determine the suitability of satellite data in capturing the fine-scale details of the diurnal cycle of convective activity, a fact that has not been adequately addressed in existing literature. It is important to note that PD1 is the only subperiod for which a complete radar dataset is available; thus, comparisons between satellite and radar representations of the convective diurnal cycle are limited to this subperiod.

Figure 5.19a displays the results of composite analysis conducted on the radar-estimated precipitation data from PD1. The precipitation estimates are based on the specific differential reflectivity and the differential phase from the polarimetric radar data (see chapter 2). To construct Fig. 5.19, composite hourly time series of estimated precipitation rates are calculated at each radar grid point. Because the radar data has a 10 minute temporal resolution, composite values for a given hour (e.g. 0800 LST) are created by using the available volume scans within 30 minutes of said hour (e.g. 0730-0830 LST). The resulting phase of the diurnal maximum in

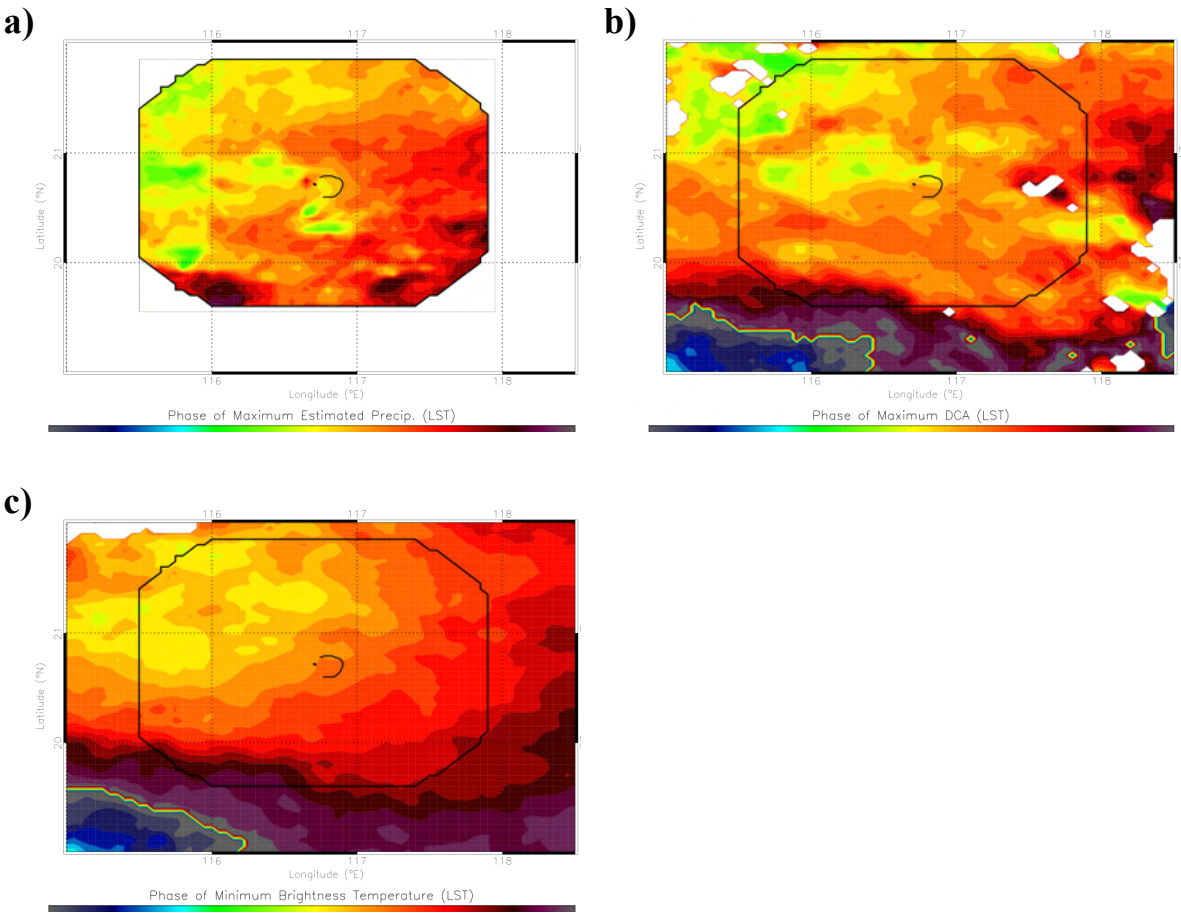

Figure 5.19 Phase of maximum convective activity during PD1, plotted over the BMRC C-POL Doppler radar domain, as suggested by: (a) radar-estimated precipitation, (b) satellite-estimated precipitation, and (c) infrared brightness temperatures.

radar-esitmated precipitation rate for each grid point is shown in Fig. 5.19a. There is a clear pattern evident in Fig. 5.19a across the entire radar domain, with the earliest diurnal maxima in precipitation rates to the north and west of the radar origin, and the latest maxima to the south and east. The southeastern coast of China is located to the north-northwest of the radar, so the pattern of phases found in Fig. 5.19a suggests an increase in the time of maximum precipitation with increasing distance from the China coast. This is the same result as found in the composite analyses of satellite brightness temperatures and DCA indices, indicating that the propagation signal exists in both direct and indirect measures of convective activity. For the sake of comparison, phase diagrams for DCA (Fig 5.19b) and brightness temperature (Fig. 5.19c)

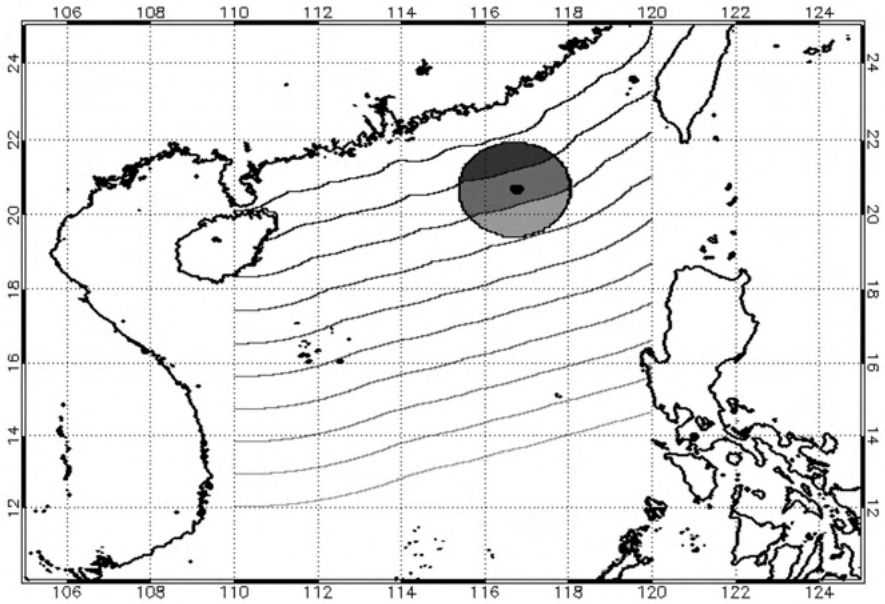

Figure 5.20 Depiction of isolines of least distance to the southeastern China coast. These isolines are used in the analyses that consider convective activity as a function of distance from the China coast. The contour interval shown above is 100 km, and the Dongsha Island radar domain is highlighted.

covering the same area as Fig. 5.19a are included. In general, both Fig. 5.19b-c match well with Fig. 5.19a, as the earliest diurnal maxima of convective activity implied by each variable is found to the north and west in Figs. 5.19a-c, and the latest maxima to the south and east. Agreement at the grid point level in Figs. 5.19a-c is evident but not as robust, with a noticeable lag in the brightness temperature representation of convective activity.

A more quantitative description of the propagation signal in the vicinity of Dongsha Island can be expressed by considering the phase of maximum convective activity with respect to the distance from the southeastern China coastline. To accomplish this, each data point within a given longitude range is binned according to the shortest distance from said point to the China coast. Figure 5.20 shows the isolines of shortest distance from the China coast across the SCS region, as well as the domain of the C-POL Doppler radar. For this analysis, the longitude range 115-118ºE is chosen to coincide with the approximate maximum east-west extent of the Dongsha

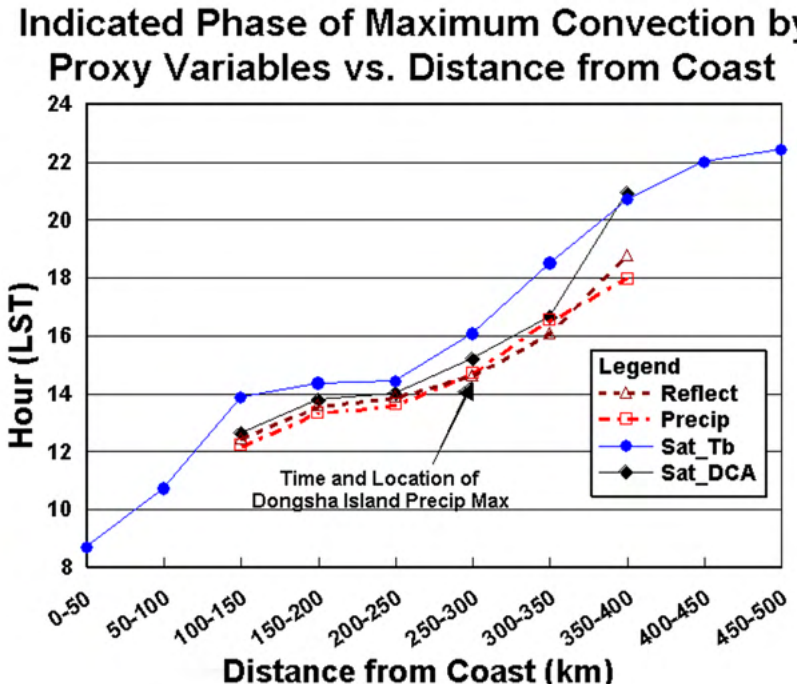

Figure 5.21 Phase of maximum convective activity vs. distance from the China coast. This graph examines the agreement in depicting the convective diurnal cycle among different proxy variables for convective activity (e.g. brightness temperature, DCA, radar estimated precipitation).

Island radar domain. The composite time series of each data point within a 50-km distance bin is averaged to obtain a single composite time series for that particular bin. Performing this procedure on the satellite brightness temperatures and DCA, and on radar reflectivity and estimated precipitation, provides a concrete and quantitative comparison of the implied phase of maximum convective activity among these proxy variables (Figure 5.21), from which the propagation signal can be better illustrated.

Fig. 5.21 shows the implied maximum of convection as a function of distance from the China coast. The results from the radar analyses are displayed over their entire available range in Fig. 5.21, while results from satellite analyses are displayed only when the amplitude at a given distance bin is significant (> 3 K for brightness temperature, > 3 mm dy^{-1} for DCA). It is

apparent in Fig. 5.21 that the phase of maximum convection increases monotonically with increasing distance from the China coast for all of the proxy variables under consideration. Satellite brightness temperatures suggest the maximum of convective activity just off the China coast occurs in the late morning hours (around 0800 LST). In the vicinity of Dongsha Island, which is between 250-300 km offshore, the implied convective maximum occurs during the early afternoon hours. The time of convective maximum increases with increasing distance from the coast until the signal becomes insignificant at around 500 km; at this distance, the implied diurnal maximum is in the late evening hours. The propagation speed indicated by the brightness temperature analysis over its entire range of significance is around 10 m s^{-1}, though the propagation speed near the vicinity of Dongsha Island is faster (~12 m s^{-1}) than it is farther from the coast (~8 m s^{-1}).

The satellite-derived DCA and radar-based variables show the same monotonic increase over their range of significance in Fig. 5.21. However, the depicted times of convective maxima for each distance bin are one to three hours earlier than that suggested by satellite brightness temperatures. This lag between brightness temperatures and (derived) precipitation has been evident throughout the analysis process. It is interesting to note that the DCA generally lags the radar variables only slightly, with the exception of the 350-400km range bin (where the DCA was only marginally significant). Considering the brightness temperature time lag, this would suggest that the DCA is better suited to capture the essence of the diurnal cycle of convective precipitation over the study region. This fact gives more confidence in using DCA to diagnose convective diurnal cycles in periods or regions where radar data is not available. The implied propagation speed from the entire DCA analysis averages around 7 m s^{-1}, though it is much faster in the vicinity of the China coast (~14 m s^{-1}) and slower beyond 300 km from the coast (~5 m s^{-1}). The possible reasons for these two distinct propagation modes will be further discussed in Chapter 6.

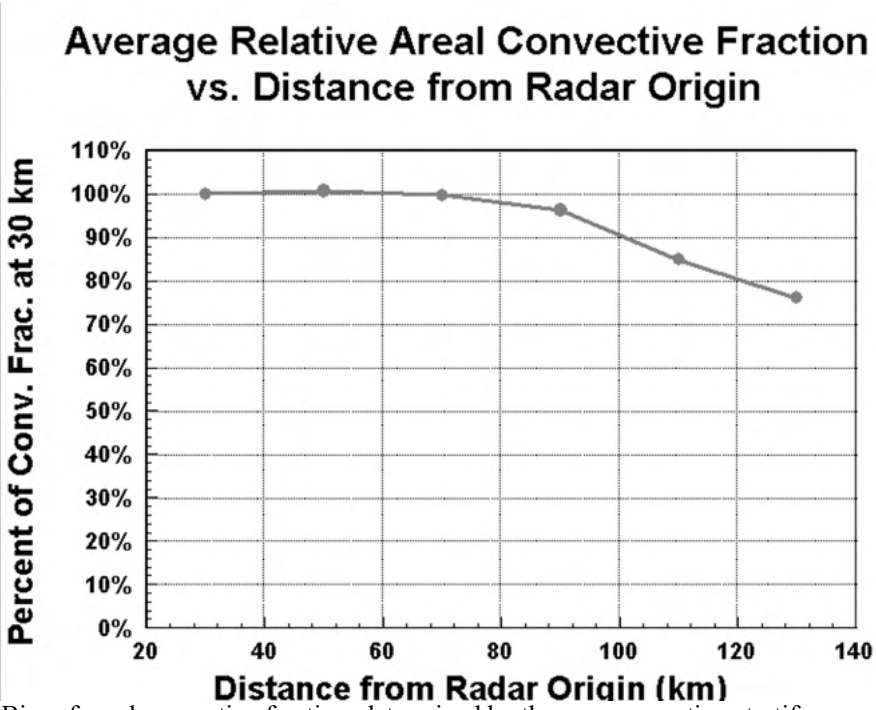

Figure 5.22 Bias of areal convective fraction, determined by the new convective-stratiform partitioning algorithm (see Appendix A), as a function of distance from radar origin.

Examining the evolution of convective systems in the C-POL Doppler radar domain is another way to diagnose the propagation away from the China coastline. It is generally accepted that as an MCS evolves, the fractional contribution of precipitation generated by convective processes to the total precipitation associated with the MCS decreases (e.g. Leary and Houze 1979; Houze 1993). This is substantiated by the fact that a convective system typically continues to precipitate even after strong ascending vertical motions have ceased. Thus, if a decrease in the convective fraction of precipitation is evident across the Dongsha island radar domain, it would imply the evolution and propagation of MCSs in the direction of said decrease.

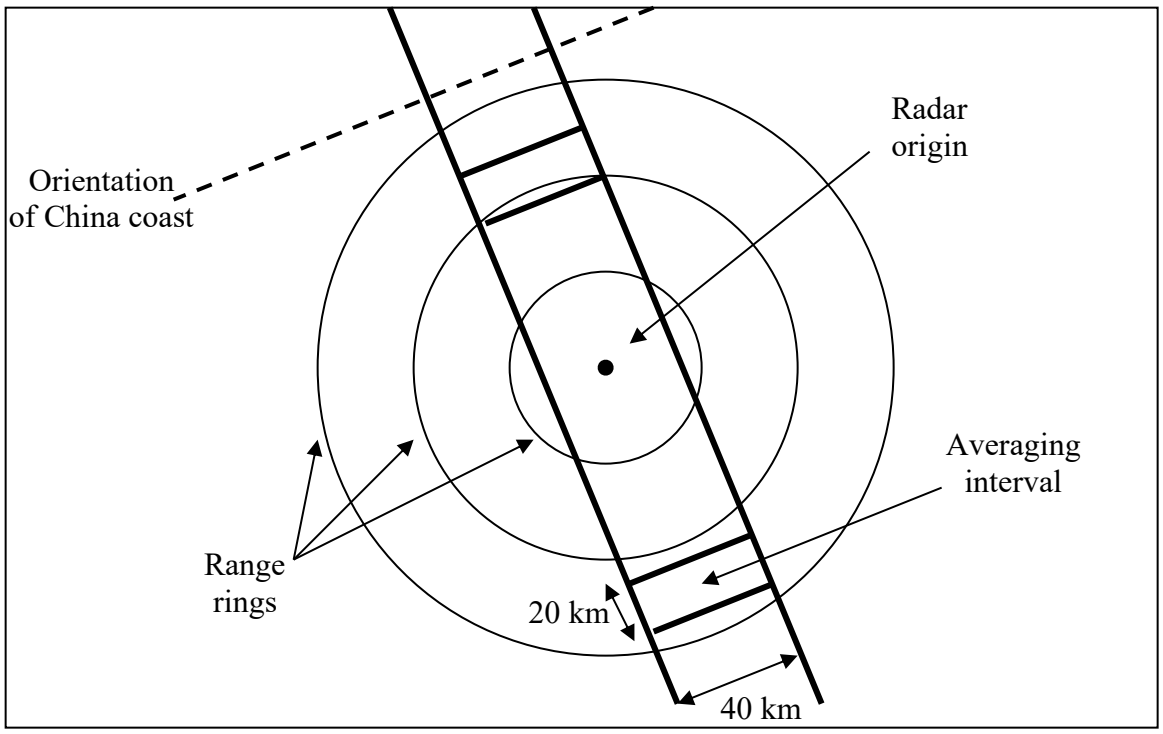

Figure 5.23 Schematic depicting essential elements in convective fraction analysis. Every 40km x 20km averaging interval is oriented perpendicular to china coast, and in a swath that runs through radar origin. For each averaging interval, average distance from coast, distance from radar origin, and areal convective fraction is determined.

Before the MCS evolution analysis can be performed, any bias in the measure of convective fraction must be removed. For the sake of simplicity, the fraction of the total precipitating area that can be attributed to convective processes (the "areal convective fraction") will be used in this analysis to remove any assumptions inherent in rainrate estimation from polarimetric data. See Appendix A, section e for more information about convective partitioning procedures. Figure 5.22 shows the bias of areal convective fraction as a function of distance from radar origin. To create Fig. 5.22, the average areal convective fraction is calculated within 20 km wide annuli surrounding the radar origin. These averages are then compared to that of the innermost annulus. It is clear in Fig. 5.22 that the average areal convective fraction decreases with increasing distance from the radar origin. This decrease in convective fraction can be attributed primarily to beam spreading, which would decrease gradients between convective cells and stratiform regions;

lofting, which would raise the radar beam closer to the bright band/freezing level; and attenuation, which would decrease the apparent reflectivity of convective regions.

The nature of the areal convective fraction is such that it cannot be reliably defined at a single grid point. Instead, it must be calculated over an area whose scale allows for the discrete nature of radar volume scans and the spatial variability within convective lines. On the other hand, the areal convective fraction must be calculated over a small enough area to remove the radial bias determined in Fig 5.22. Figure 5.23 depicts the essential elements that were used in the analysis of areal convective fraction over the C-POL radar domain. Only a 40-km wide swath is considered in this analysis, chosen such that it bisects the C-POL Doppler radar domain and its orientation is approximately perpendicular to that of the southeastern China coast at the longitude of the radar origin (116.7ºE). Within this swath, calculations are performed over 20 km "averaging intervals". For each 40 km x 20 km averaging interval, the average distance from the radar origin, distance from the China coast, and areal convective fraction are obtained. Then, using Fig. 5.22, the average areal convective fraction for each averaging interval is normalized according to its average distance from the radar origin.

The outcome of the areal connective fraction analysis is shown in Figure 5.24. It is clear, with a high degree of consistency ($R^2 \approx 0.8$), that the areal convective fraction decreases with increasing distance from the southeastern China coast. Assuming that the proximity to land does not fundamentally alter the structure of MCSs, the decrease would suggest that MCSs are more mature the farther they are from the coastline, in that they develop an increasing proportion of stratiform precipitation (e.g. Houze 1977). As stated earlier, this implies a preference for MCS propagation to be in a direction away from the coast.

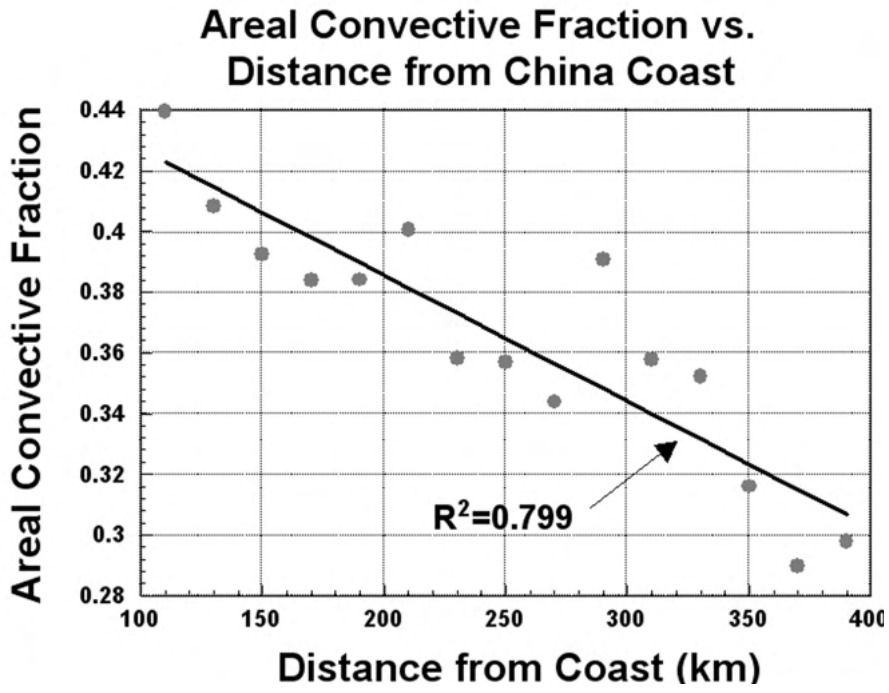

Figure 5.24 Areal convective fraction of averaging intervals in a swath across the radar domain as a function of distance from southeast China coast.

In summary, a propagation signal was clearly evident over the northern SCS during the convectively active time period PD1. This signal was found when considering both brightness temperatures and satellite-estimated precipitation (DCA). Analysis of radar data found the same propagation signal within the confines of the C-POL Doppler radar domain when considering both radar-estimated precipitation and areal convective fraction. Because radar records are complete for only PD1, it is important to note that the results based on radar analyses closely matched the DCA analyses, while brightness temperature analyses showed similar trends with a 1-3 h time lag. This conclusion will give more credibility to DCA analyses in diagnosing the diurnal cycle of convective activity in periods where radar data is not available.

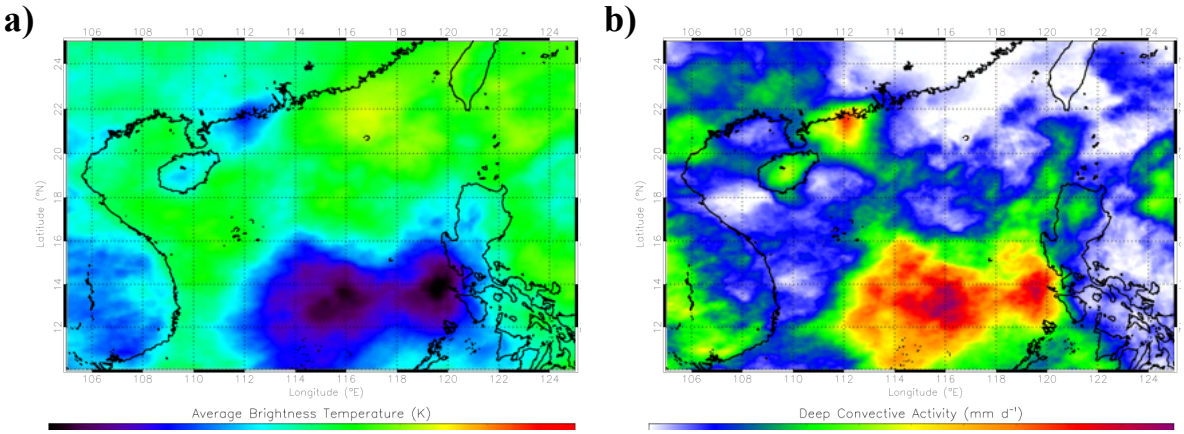

Figure 5.25 Average brightness temperatures (a) and satellite estimated precipitation (b) over the northern and central SCS region during PD2 (21-31 May 1998).

c. The diurnal cycle of convection over the SCS during PD2 (21-31 May 1998)

During the second subperiod (PD2; 21-31 May 1998), there is a notable southward shift of convective activity into the central and southern SCS. On the synoptic scale, it is evident that several factors contributed to this shift. Conditions became more favorable for convective development in the central and southern SCS as the western Pacific subtropical ridge retreated eastward out of the region and was replaced by monsoon westerlies. In the northern SCS, a weak cold frontal passage from the China mainland led to a reduction in CAPE during the period. This was evident in the average 850 mb flow during PD2, as the westerly monsoon current was displaced southward, and low level transport over the northern SCS was more continental in nature. Drier air was also evident throughout the troposphere over the northern SCS during this time, possibly caused by entrainment from higher in the atmosphere or advection from the Asian continent (Johnson and Ciesielski 2002; Ding and Lau 2001).

Figures 5.25a-b show the spatial distribution of the averages of infrared brightness temperature and DCA during PD2. By far, the lowest average brightness temperatures are found

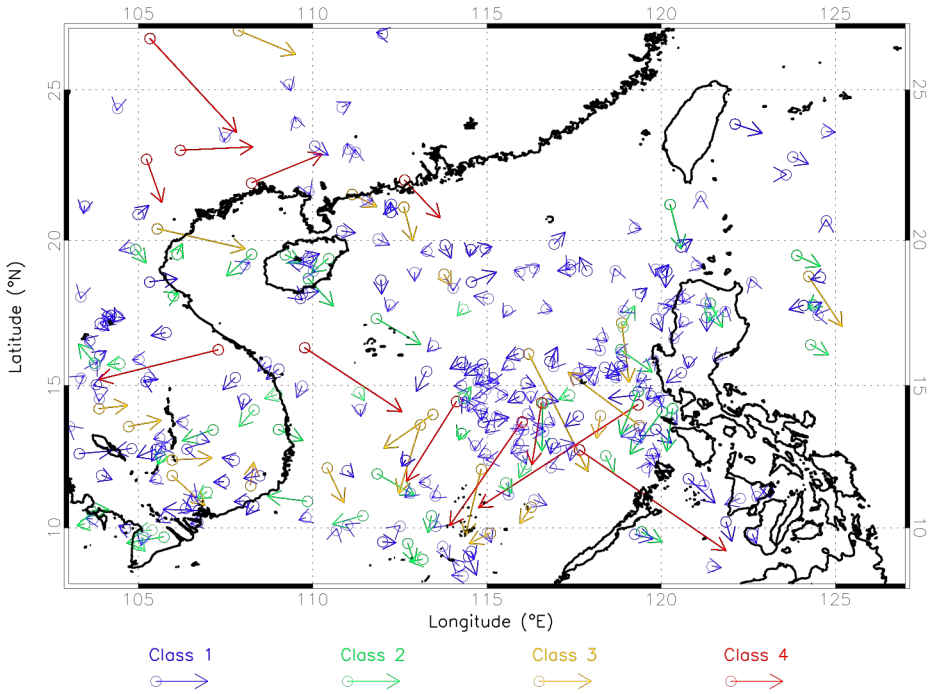

Figure 5.26 Time cluster tracks, which depict the motion of discrete cold convective cloud shields across the northern and central SCS region during PD2 (21-31 May 1998). A circle denotes the location that the tracking algorithm first detects a time cluster, while the arrow points to the last detectable location of said cluster.

in the central SCS, between 10º-16ºN and 112º-120ºE (Fig 5.25a). Other brightness temperature minima are found over southeastern Asia, and along the China coast west of Hong Kong. Intermediate values of average brightness temperature across the northern SCS suggest intermittent cloud activity. Average values of DCA (Fig 5.25b) are again consistent with the brightness temperature representation of convective activity. The most intense satellite-estimated rainfall is found in the central SCS, with a secondary maximum along the China coast. Extreme rainfall is evident in the central SCS during PD2, with estimated averages reaching 50 mm d^{-1} over the 11 day period. Figure 5.25b also suggest that almost no convective activity (with cloud tops < 230 K) is evident in the vicinity of Dongsha Island during this time.

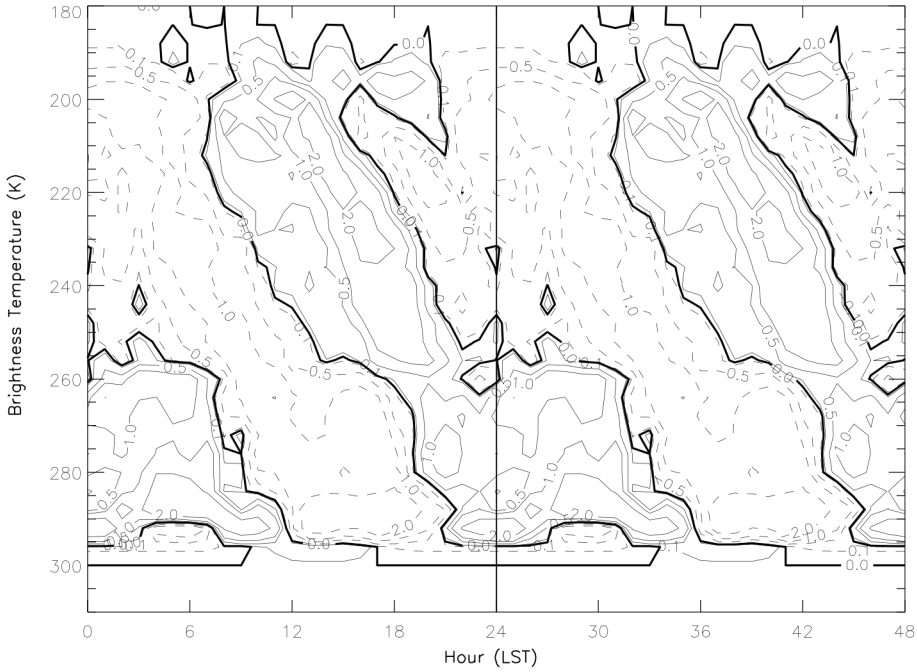

Figure 5.27 Evolution histogram for the PD2 time period and over the region bounded by 13-17ºN, 113-117ºE. The values shown above are percentage anomalies, found by subtracting the daily mean histogram of brightness temperature from hourly histograms. Positive anomalies indicate when cloudiness of a given brightness temperature is more frequent than its average daily occurrence.

Time cluster tracks (Figure 5.26) show many large MCSs (class 3-4) moved across the convectively active central SCS during this period. Interestingly, each one of these large MCSs has a southward component in its motion vector. The central SCS is also the region with the highest concentration of small cloud clusters during this time period. The secondary convective maximum in the vicinity of Hong Kong is denoted by four large southward-moving MCSs in Fig. 5.26. Also notable is the lack of time clusters around and north of Dongsha Island during PD2. As found in PD1, time cluster (Fig 5.26), DCA (Fig 5.25b), and brightness temperature (Fig 5.25a) analyses all paint the same general picture of convective activity across the SCS, agreeing in where convection both did and did not occur.

The evolution histogram of cloudiness (Figure 5.27) over the most convectively active region of the central SCS during PD2 (chosen to be 13º-17ºN, 113º-117ºE) looks quite similar to that of PD1 (Fig. 5.15), with a few notable differences. One considerable difference is that the convection is more intense in PD2, as depicted by the higher frequency of very cold (< 208 K) cloud tops. This could have been caused by several factors, including warmer SSTs or higher CAPE values over the central SCS (as compared to that over the northern SCS during PD1). Secondly, the growth and decay cycle of MCSs is clearer in the PD2 evolution histogram as compared to PD1. PD1 convection is characterized by frontal forcing and an abundance of midlevel (~ 260 K) cloudiness, whereas PD2 is not.

Multiple maxima in extremely cold cloud top frequency (<200 K) in Fig. 5.27 are likely caused by the morphology of individual MCSs, and are an artifact of the relatively short duration of PD2. Thus, only brightness temperatures warmer than 200 K are considered in the diurnal analysis of convection. The maximum frequency of cloudiness at 200 K occurred around noon local time, with roughly agrees with the early afternoon maximum found in PD1. The regular decay of MCSs is evident as cloudiness at increasingly warmer brightness temperatures is most frequent at an increasingly later time. This trend is clear through around 2000 LST.

A Hovmöller diagram of infrared brightness temperatures (Figure 5.28) is again employed to illustrate the variation of the phase of maximum convective activity across the SCS. Figure 5.28 was constructed by averaging values in a 2º longitude band centered on 116ºE to coincide with the maximum DCA in Fig 5.25b. In agreement with the evolution histogram (Fig 5.27), the coldest brightness temperature averages in Fig 5.28 occur between 1100-1400 LST between 12º and 14ºN. Also evident in Fig 5.28 is the southward propagation of systems over several degrees of latitude throughout the composite time series. The southern/leading edge propagated

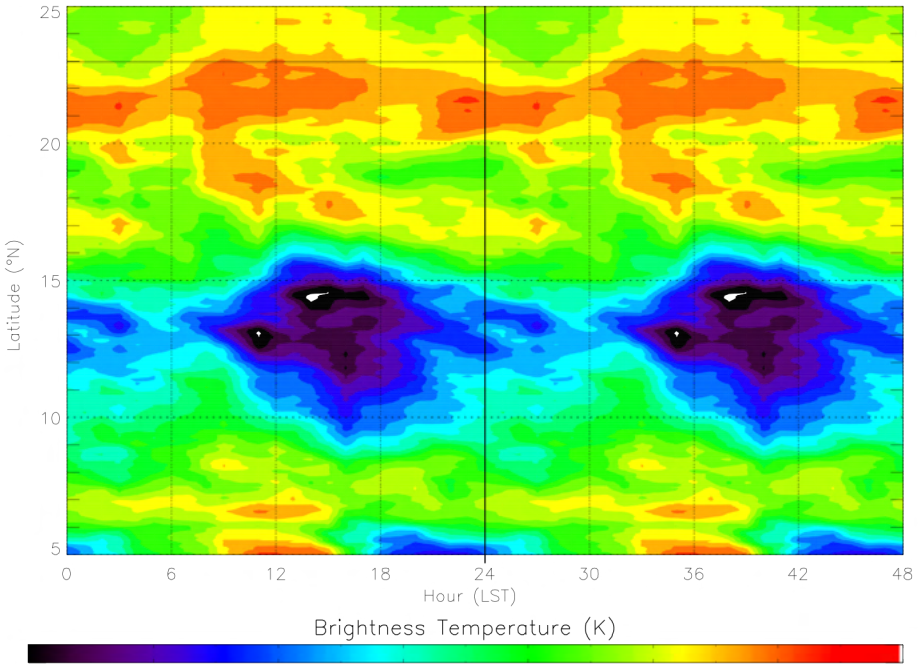

Figure 5.28 Hovmöller diagram depicting the average brightness temperature for PD2 as a function of latitude and time of day. The solid line at 23ºN denotes the location of the China coastline at this longitude. Only the data within a two-degree longitude swath centered on 116ºE was considered in this analysis.

southward at a speed of around 15 m s^{-1}, while the lines following the minima of brightness temperatures suggest a "core" propagation speed of around 10 m s^{-1}.

As in PD1, composite analysis will be used to further study the amplitude and phase of the diurnal cycle of convection over the SCS during PD2. Figures 5.29a-b illustrate the results of composite analysis on brightness temperature time series. Not surprisingly, the highest regressed amplitudes of brightness temperatures (Fig 5.29a) correspond with the regions of maximum convective activity found in Figs. 5.25-5.26; amplitude maxima are evident over the central SCS, southeastern Asia, and over the islands of Hainan and Luzon. Generally insignificant regressed amplitudes are found around Dongsha Island, as convection was found to be lacking there during PD2. The phase of minimum brightness temperatures (Fig 5.29b) suggests a broad region over

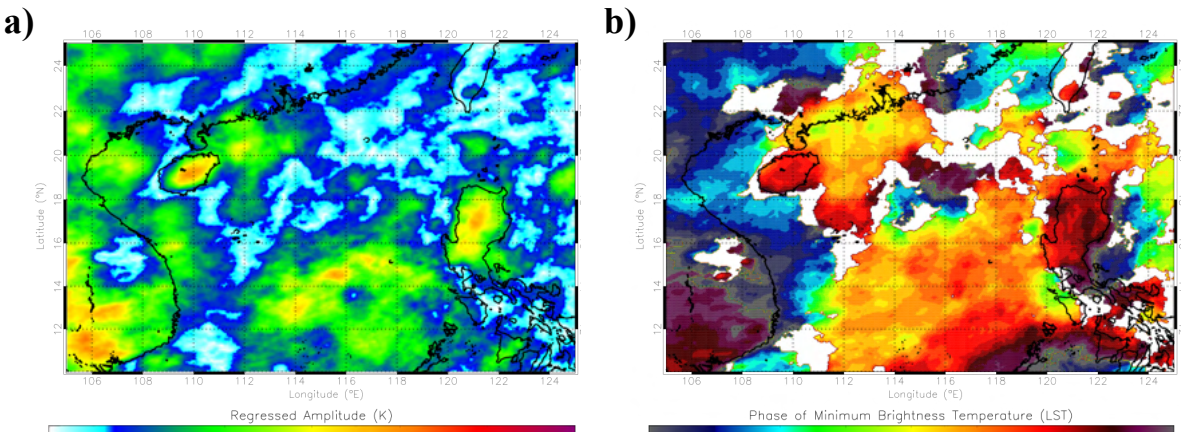

Figure 5.29 Regressed amplitude (a) and phase of minimum (b) in the diurnal composite time series of brightness temperature for PD2. In (a), higher values are indicative of a stronger and more coherent diurnal cycle of brightness temperature. In (b), the times shown correspond to the phase of maximum convective activity as suggested by brightness temperatures, and only data points with significant (> 3 K) regressed amplitudes are displayed.

the central SCS with a convective maximum in the early afternoon (1200-1600 LST). Also evident is a hint of the southward propagation of systems across the region, with a noontime diurnal minimum around 16ºN transitioning to a late evening minim around 10ºN. In the vicinity of the secondary convective maximum near Hong Kong, the earliest phase of the diurnal minimum of brightness temperature is found along the coast in late morning, and as found in PD1, the phase increases in time with increasing distance from the coast. In fact, Fig. 5.29b suggests a 2-day transit of convection from the southern China coast to the central SCS. This was caused by a large convective system that formed west of Hong Kong in the early morning hours of 24 May and propagated southward before losing its identity near 13ºN, 115ºE around midnight on 26 May.

Figures 5.30a depicts the regressed amplitude of DCA using composite analysis. Fig. 5.30a looks remarkably similar to Fig. 5.29a with maxima in the same general locations (central SCS, Southeast Asia, west of Hong Kong, and the island of Hainan), although the regressed amplitudes are greater in Fig. 5.30a. Also similar are the times of convective maxima suggested by the phase

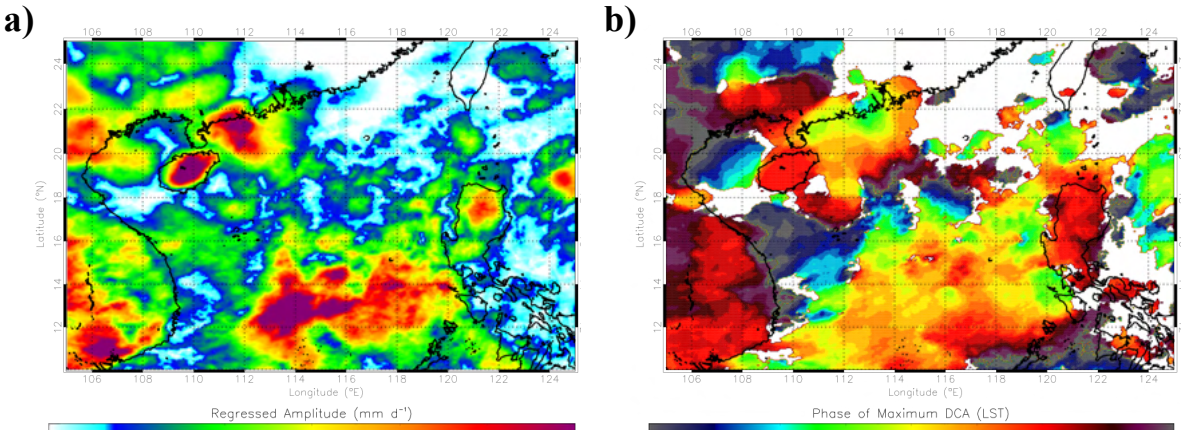

Figure 5.30 Regressed amplitude (a) and phase of maximum (b) in the diurnal composite time series of satellite-estimated precipitation for PD2. In (a), higher values are indicative of a stronger and more coherent diurnal cycle of DCA. In (b), the times shown correspond to the phase of maximum convective activity as suggested by DCA, and only data points with significant (> 3 K) regressed amplitudes are displayed.

of maximum DCA (Fig. 5.30b), as compared to Fig 5.29b. Most of the central SCS has a diurnal DCA maximum between 1000-1400 LST, with hints of southward propagation again evident. Near Hong Kong, the earliest DCA maximum occurs along the China coast around 0900 LST, with later maxima farther from the coast (for example, around 1600 LST at 19ºN, 113ºE). The 2-day transit signal is even clearer in Fig 5.30b.

To better compare the propagation signals evident in PD1 and PD2, regressions based on the distance from the China coast are again utilized using the same methodology as in Figure 5.21. However, an important point must be made when considering the analysis of PD2 data. As previously discussed, only a small expanse of the China coast was frequented by convective activity during PD2. The longitudinal area under consideration during PD2 decreased accordingly to encompass the majority of this activity, thereby decreasing the degrees of freedom and introducing larger errors into the analysis. Considering brightness temperatures (Figure 5.31a), the time of the diurnal minimum increases with increasing distance from the coast for

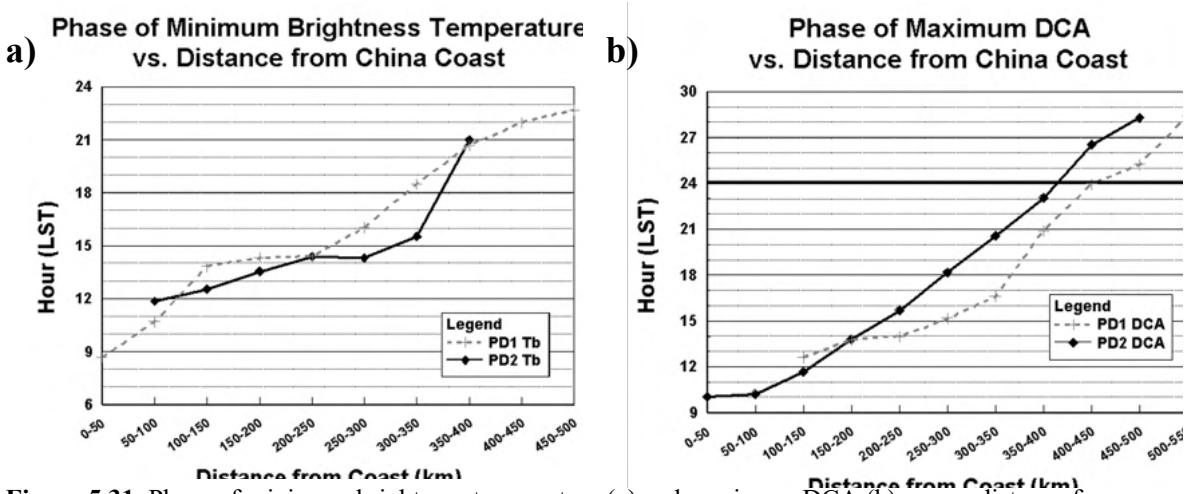

Figure 5.31 Phase of minimum brightness temperature (a) and maximum DCA (b) versus distance from the southeastern China coast for PD1 (15-20 May) and PD2 (21-31 May).

both PD1 and PD2, though the trend in PD2 isn't as linear as in PD1. Even more interestingly, the times match well between PD1 and PD2 within each range bin, with a maximum difference of around 3 hrs. This would imply that the propagation signals evident in PD1 and PD2 are indeed similar in nature.

Figure 5.31b shows the same analysis as in Fig 5.31a, only conducted on DCA instead. As in Fig 5.31a, the time of maximum DCA increases with increasing distance from the coast for both periods. In this instance, however, the PD2 DCA trend is consistently later than that of PD1 by 2-3 hrs beyond 250 km. Even so, the error in the analysis of PD2 is such that the two signals are not different in a statistically significant way. By performing a least-squares regression on the PD1 and PD2 signals, it is evident that they both suggest the same propagation speed (7 m s^{-1} in PD1, 6.5 m s^{-1} in PD2). In this manner, it is suggested that the two signals represent the same tendency for convective systems to propagate away from the coast of China in a coherent diurnal fashion, regardless of the proxy variable under consideration.

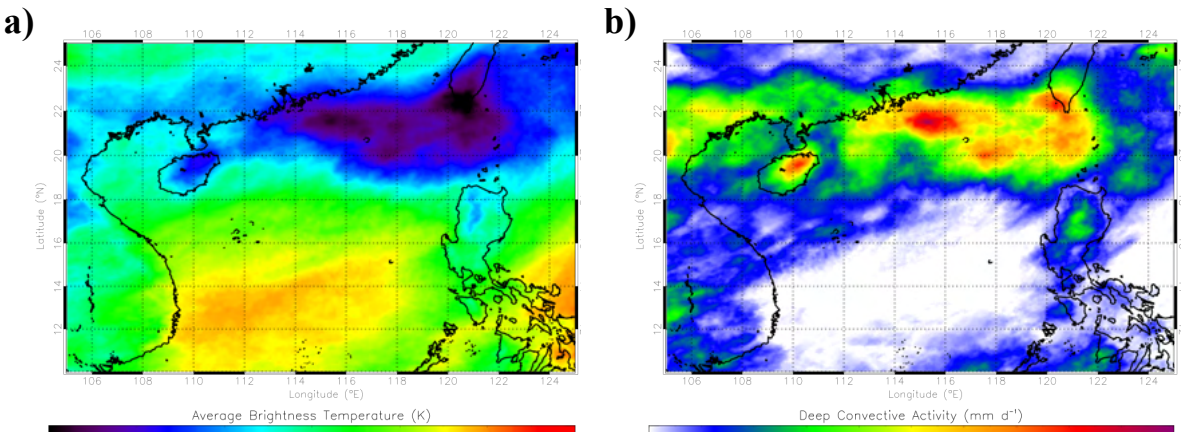

Figure 5.32 Average brightness temperatures (a) and satellite estimated precipitation (b) over the northern and central SCS region during PD3 (1-10 June 1998).

d. The diurnal cycle of convection over the SCS during PD3 (1-10 June 1998)

The third subperiod (PD3; 1-10 June 1998) is marked by another distinct shift in the regional monsoon pattern. PD3 is defined as starting when the westerly monsoon flow strengthened in the northern SCS at the beginning of June, causing a 10-day period of convective development along the southern China coast. PD3 ends as the convective band jumps farther north into southern China after 10 June, marking the start of the Meiyu season and causing extensive flooding in the Yangtze River valley. This northward progression of the monsoon convergence zone and convective band is a natural progression of monsoon development and has been documented by many authors (e.g. Lau and Li 1984, Chang and Chen 1995, Johnson and Ciesielski 2002).

Figures 5.32a-b depict the average brightness temperatures and DCA, respectively, over the region during PD3. Both Figs 5.32a-b suggest that the greatest convective activity was confined to an east-west band between 18º and 23ºN. Although not as intense as PD2, a large swath of satellite estimated precipitation > 20 mm d^{-1} extends across most of the northern SCS in Fig 5.32b. At the same time, almost no cloud activity is evident over the central SCS as the westerly

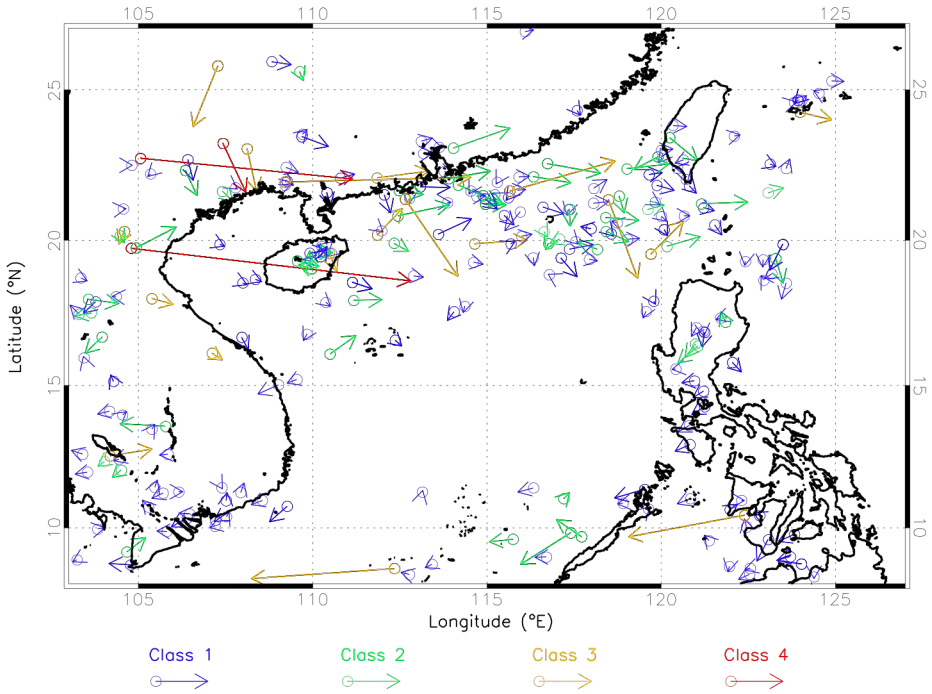

Figure 5.33 Time cluster tracks, which depict the motion of discrete cold convective cloud shields across the northern and central SCS region during PD3. A circle denotes the location that the tracking algorithm first detects a time cluster, while the arrow points to the last detectable location of said cluster.

monsoon current slackened and was replaced with a low-level easterly flow, east of 115ºE, from the western Pacific subtropical high.

Once again, the time cluster analysis (Figure 5.33) agrees well with the insight provided by average brightness temperature and DCA analyses. A distinct band of time clusters extends east-west across southern China and the northern SCS during PD3. Two large (class 4) cloud clusters traversed several hundred kilometers ESE across extreme southern China, the Gulf of Tonkin, and the island of Hainan and likely had a profound influence on the diurnal cycle in this area. Several large (class 3) time clusters are also evident across the northern SCS during this period. About half of these had a noticeable southward component of motion, with the rest moving relatively due east. Not surprisingly, the highest concentration of small cloud clusters, found in the vicinity of Dongsha Island, coincides with the region of maximum convective activity

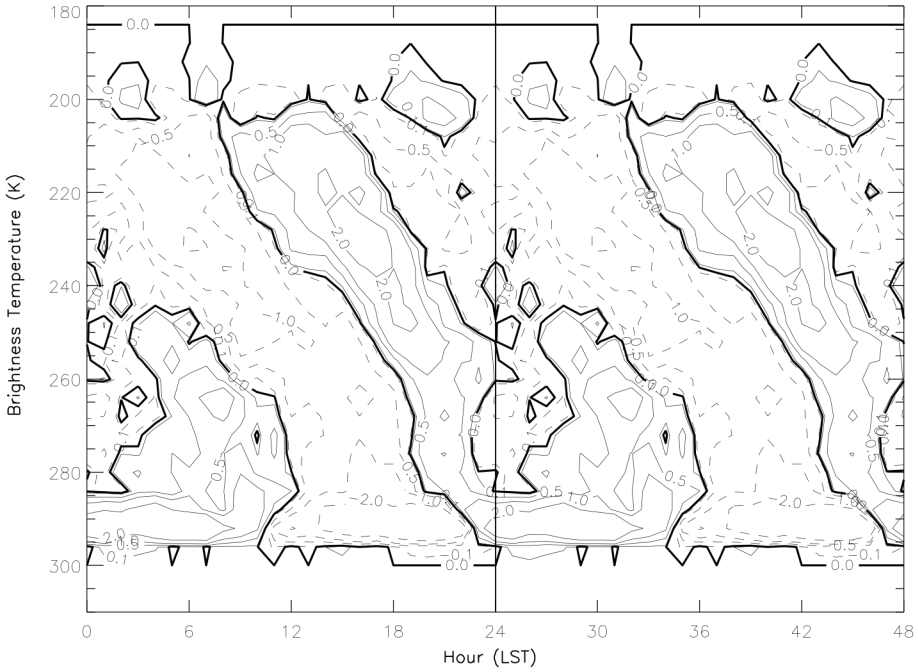

Figure 5.34 Evolution histogram for the PD3 time period and over the region bounded by 18-22ºN, 115-119ºE. The values shown above are percentage anomalies, found by subtracting the daily mean histogram of brightness temperature from hourly histograms. Positive anomalies indicate when cloudiness of a given brightness temperature is more frequent than its average daily occurrence.

indicated in Figs 5.32a-b.

The evolution histogram of cloudiness over the most convectively active region during PD3 (18-22ºN, 115-119ºE) is displayed in Figure 5.34. Fig 5.34 is remarkably similar to the evolution histograms of PD1 (Fig 5.15) and PD2 (Fig 5.27). However, the convection depicted during PD3 in Fig 5.34 is more intense than that in PD1, as indicated by the higher frequencies of the coldest cloud tops. Johnson and Ciesielski (2002) suggest this is consistent with higher surface specific humidities that contributed to higher CAPE values during PD3. Because PD3 is a relatively short time interval, the infrequent occurrence of cloudiness with brightness temperatures < 200 K led to multiple frequency maxima that will not be discussed. The largest coherent structure in Fig 5.34 has a maximum occurrence of cold (~205 K) cloud tops around 1400 LST, in good agreement

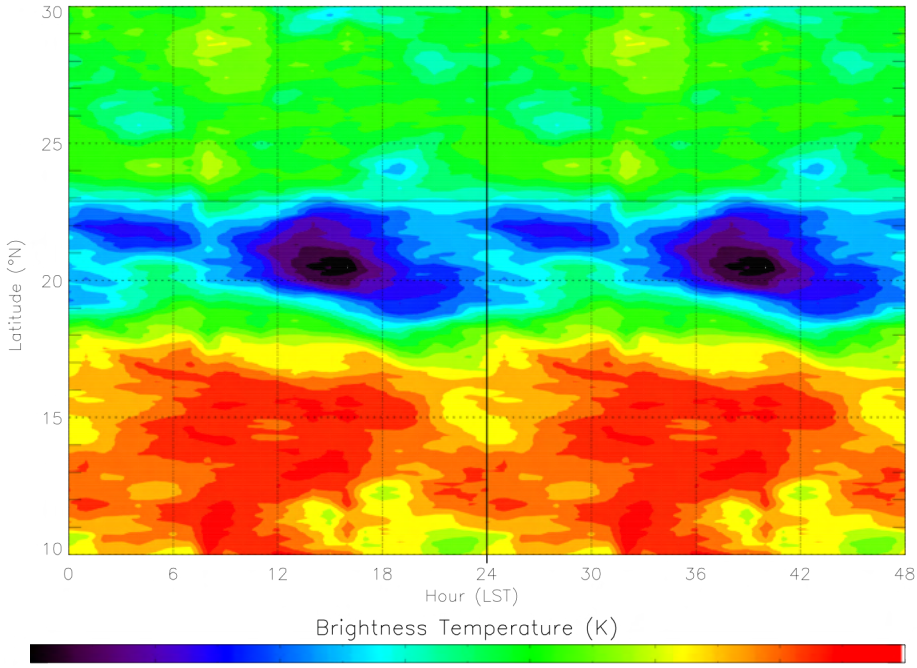

Figure 5.35 Hovmöller diagram depicting the average brightness temperature for PD3 as a function of latitude and time of day. The solid line at 23ºN denotes the location of the China coastline at this longitude. Only the data within a two-degree longitude swath centered on 118ºE was considered in this analysis.

with the other subperiods. Also similar is the depicted life cycle of MCSs, with the pattern of increasing brightness temperatures becoming most frequent at increasingly later times through around 2000 LST.

To examine the north-south variation in the diurnal cycle of convection, a Hovmöller diagram of brightness temperatures is presented in Figure 5.35. To create Fig 5.35, the composite brightness temperature time series are averaged in a two-degree longitude swath centered on 118ºE. The maximum in convective activity suggested by Fig. 5.35, around 1400 LST at 21ºN, is consistent with that found in Fig 5.34. Also evident in Fig. 5.35 is a tendency for southward propagation of convective systems, with the cold brightness temperature anomaly extending

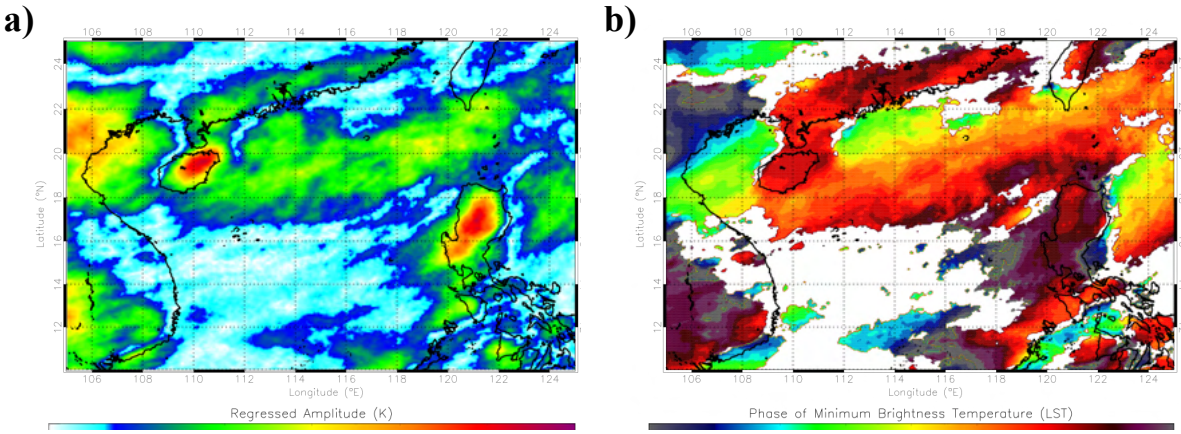

Figure 5.36 Regressed amplitude (a) and phase of minimum (b) in the diurnal composite time series of brightness temperature for PD3. In (a), higher values are indicative of a stronger and more coherent diurnal cycle of brightness temperature. In (b), the times shown correspond to the phase of maximum convective activity as suggested by brightness temperatures, and only data points with significant (> 3 K) regressed amplitudes are displayed.

through about 4º of longitude in 12 hours. This would yield a 10 m s^{-1} propagation speed, which has been a common result among brightness temperature analyses of periods PD1-PD3.

Figures 5.36a-b display the spatial distribution of composite analysis on brightness temperatures during PD3. The regressed amplitude of brightness temperature (Fig 5.36a) is generally consistent with the level of convective activity across the region. An east-west band of maximum regressed amplitudes is evident across the northern SCS; islands exhibit the highest regressed amplitude because the convection there is more driven by the solar heating cycle. One noticeable difference between Fig 5.36a and Figs. 5.32-5.33 is the insignificant amplitudes found in the convectively active region immediately along the southern China coast. This was caused by a few systems that remained locked along the China coast for many hours, instead of propagating southward as a majority of systems did. The phase of the diurnal minimum of brightness temperatures (Fig 5.36b) shows a clear and systematic variation of increasing phase with increasing distance from the coast. This signal is evident across the entire northern SCS, even in the Gulf of Tonkin, and is only interrupted by the island of Hainan and its regular

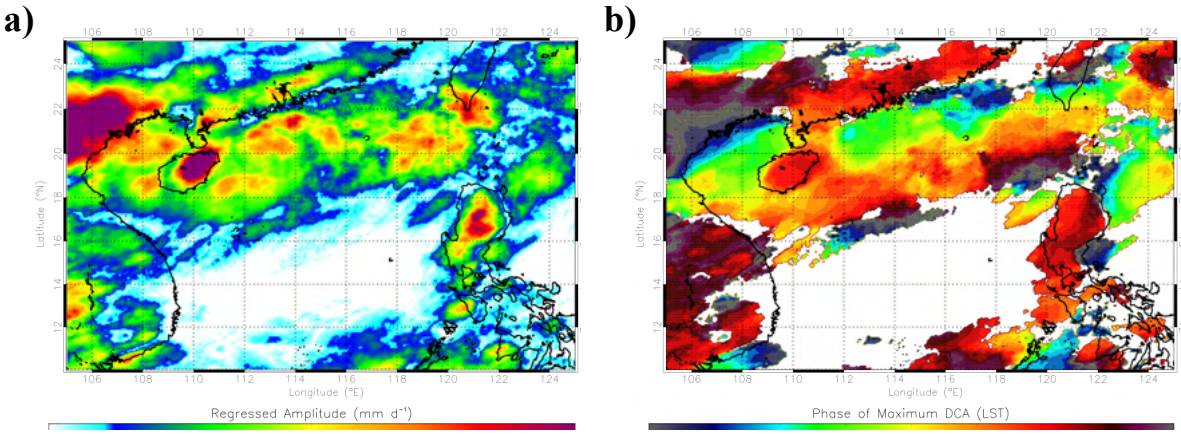

Figure 5.37 Regressed amplitude (a) and phase of maximum (b) in the diurnal composite time series of satellite-estimated precipitation for PD3. In (a), higher values are indicative of a stronger and more coherent diurnal cycle of DCA. In (b), the times shown correspond to the phase of maximum convective activity as suggested by DCA, and only data points with significant (> 3 K) regressed amplitudes are displayed.

afternoon thunderstorms. Early morning minima (0600-0900 LST) are found most commonly along the China coast, with the phase increasing to 2100 LST around 17-18ºN were the signal becomes insignificant.

Composite analysis of DCA during PD3 (Figures 5.37a-b) yields similar results to the brightness temperature analysis. Regressed amplitudes of DCA are highest in an east-west band along the southern coast of China (Fig 5.37a). The islands of Hainan and Luzon exhibit higher regressed amplitudes due to the daily occurrence of afternoon thunderstorms. In addition, the region just inland of the Gulf of Tonkin has a very high regressed amplitude of DCA that is likely caused by the regular formation of large MCSs as depicted in Fig 5.33. As in Fig 5.36b, the spatial pattern of the phase of maximum DCA (Fig 5.37b) exhibits a coherent variation across the entire northern SCS (except for the island of Hainan). Mid-morning maxima are common along the coast, increasing to late afternoon where the signal is lost (approximately 500 km away from the coast).

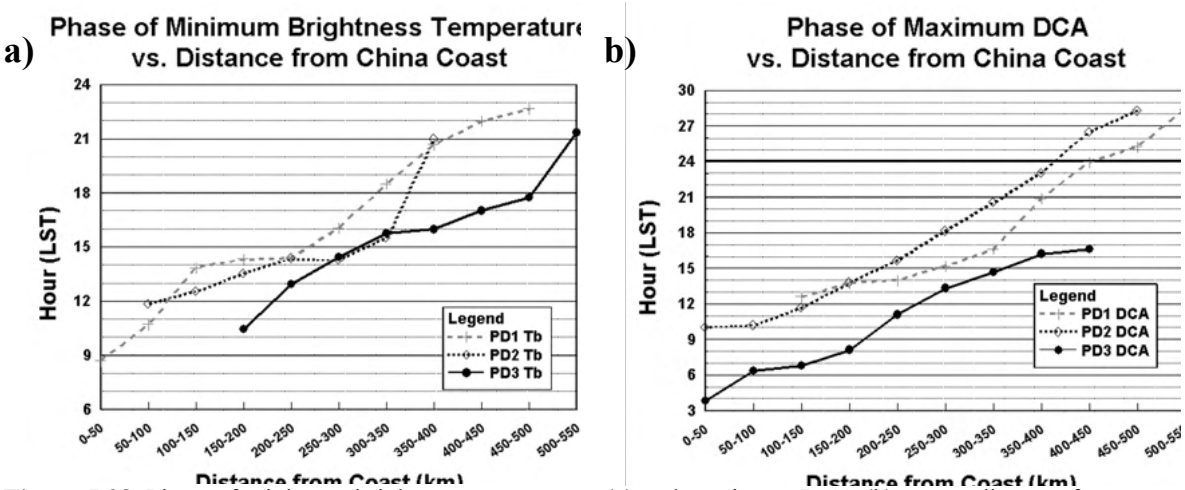

Figure 5.38 Phase of minimum brightness temperature (a) and maximum DCA (b) versus distance from the southeastern China coast for PD1 (15-20 May), PD2 (21-31 May), and PD3 (1-10 June).

Figure 5.38a considers composite analysis of brightness temperatures based on the distance from the China coast. There is generally good agreement of phasing among subperiods PD1, PD2, and PD3 at the range bins where regressed amplitudes were highest (200-400 km from the coast); the variability of phases in this range is only 1-3 hr. Larger variability (3-5 hr) is evident farther from the coast, but regressed amplitudes are less in this region, and thus uncertainties are higher. Propagation speeds suggested by the signals in PD1-PD3 are between 10 and 14 m s^{-1}, while the propagation speed of all periods considered together is 12 m s^{-1}. The phase of maximum DCA with respect to distance from the China coast (Figure 5.38b) is not as consistent among periods PD1-PD3, but it must be repeated that the PD2 analysis contains a relatively high degree of error. Comparing PD1 and PD3, the differences are again quite small in the region of high regressed amplitude (200-400 km), but are higher near the edges of the signal when significance is more questionable. Estimated propagation speeds correspond well among the subperiods PD1-PD3 (7 ± 1 m s^{-1}), as well as by considering all three periods together (8 m s^{-1}).

The physical reasons for the discrepancy in propagation speeds between brightness temperature and DCA analyses are further explored in Chapter 6.

It is clear that there is a high degree of consistency when considering the diurnal cycles of convection across the SCS that are apparent in subperiods PD1-PD3. Even though the large-scale circulations driving the convection are somewhat different among the subperiods, the general diurnal cycle of convection across the entire region is always found to be in the early afternoon hours. Evolution histograms depict similar MCS life cycles in a diurnal sense. Hovmöller diagrams show an afternoon convective maximum as well as a tendency for MCSs to propagate southward through the region. And composite analyses consistently show a tendency for convective systems to propagate away from the China coast with time, in both spatial distributions of phase and in analyses based on distance from the coastline. The high degree of repetition among periods PD1-PD3 strongly suggests that this propagation tendency is significant statistically, within the bounds to be expected by considering a single season of data. The comparison of these results to other published work, as well as the possible causes of this coherent diurnal variation of convection, are considered in the next chapter.

Chapter 6: Discussion

In the previous chapter, the diurnal cycle of convection over the South China Sea during the period 1 May-30 June 1998 was extensively documented, using infrared brightness temperatures, satellite-estimated precipitation, and radar data from the BMRC C-POL Doppler radar located on Dongsha Island. The purpose of this discussion chapter is threefold. First, comparisons to literature will be drawn to determine if the results from 1998 agree with previous studies. Second, other years of available data will be examined to verify that the propagation signal found in 1998 is robust. Third, physical interpretations of the possible causes for the results in 1998 will be discussed.

a. Comparison of results with existing literature

In general, the diurnal maximum of convective activity was found to be during the early afternoon hours over most of the northern and central South China Sea. This was true when considering infrared brightness temperatures, occurrence of cold cloudiness (< 208 K), measures of satellite-estimated rainfall (DCA), and cloud cluster analyses. The afternoon maximum of convection was perhaps most poignant in the EOF analysis of diurnal infrared brightness temperatures (Figs. 5.10-5.12). Using this method, the diurnal cycle was found to be in phase with the leading EOF, which implied a 1600 LST maximum of convective activity, across a large portion of the northern and central SCS domain (10º-25ºN, 110º-120ºE). Even considering the frequency of cold (< 208 K) convective cloudiness, to reduce the documented lag associated with

warmer thresholds (e.g Chen and Houze 1997), a noon maximum of convective activity is suggested.

This afternoon maximum of convective activity matches well with the broad-scale results of Nitta and Sekine (1994). In that study, nine years of infrared satellite data was examined using a DCA-like index, only with a 250 K threshold (as compared to 230 K in the current study). Nitta and Sekine (1994) found a clear early afternoon maximum of convective activity over the South China Sea during the months of May and June. However, it must be noted that the 250 K threshold they chose was low enough to include less desirable weather phenomena, such as decaying cirrus shields and congestus clouds that may not necessarily be precipitating. Regardless, the diurnal cycle found in Nitta and Sekine (1994) lends credibility to the afternoon maximum of convection found in 1998.

Ohsawa et al. (2001) utilized a hybrid satellite technique for discerning convective activity over tropical Asia. The dataset used included four years (1996-1999) of data spanning the months of June, July, and August. To focus on deep convection, Ohsawa et al. (2001) employed a hybrid technique that considered the difference between equivalent black body temperatures in the infrared and water vapor channels. A small difference was found to correlate better with precipitation than infrared thresholds did. Using this technique, Ohsawa et al. (2001) found that 75% of ocean grid points in their domain (0º-30ºN, 80º-120ºE) exhibited a maximum of convective activity between 1100-1700 LST. Specifically, this was found to be true over the South China Sea as well, in agreement with the 1998 results in this study. Nitta and Sekine (2001) attributed this afternoon maximum to the solar radiative heating argument of Chen and Houze (1997).

In addition to the general afternoon maximum of convection, results from 1998 suggest that there was evidence of a propagation signal, or a systematic variation in the phase of the diurnal cycle of convection with a coherent spatial structure. Across the northern SCS, there was a tendency for the maximum of convective activity to be earliest along the southeastern China coast, with the time of diurnal maximum increasing with increasing distance from the coast. More specifically, the maximum of convection was found to be mid-morning in the immediate vicinity of the coastline, increasing to early afternoon around Dongsha Island, and evening by the time the signal was lost sround 500 km from shore. This signal was portrayed in brightness temperature, satellite-derived precipitation, and in the case of subperiod PD1, even radar reflectivity and estimated rain rates. Thus, while brightness temperatures alone may be adversely affected by decaying cirrus cloud shields of MCSs whose precipitation has ceased, the fact that more direct measures of precipitation yield the same conclusion gives confidence to the results from brightness temperature techniques. It is also important to note that the propagation tendency was found in all subperiods. The fact that the signals overlap, considering individual subperiods in conjunction with the entire MYJN period, suggests that the results are robust and not just a mathematical artifact of the analyses.

At the time of writing of this study, there have not been any high-resolution studies of convection over the South China Sea (to the author's knowledge) that can be compared to the 1998 results. It is worth noting, however, that the conclusions of Wai et al. (1996) correspond well with this study. Wai et al. (1996) found a morning maximum in rainfall for coastal stations near Hong Kong, which they suggest is caused by the interaction of a diurnal land breeze/downslope flow and the onshore summer monsoonal flow. They also reference a Chinese technical note, based on a radar climatology of the region (1967-69) which revealed a morning maximum in radar echoes along the southeastern China coast, and an afternoon maximum in

radar echoes in the open ocean to the southeast of Hong Kong. These facts loosely agree with the propagation signal found in the 1998 satellite and radar data.

Although brightness temperature and DCA analyses both showed a propagation signal extending away from the southeastern China coast, the calculated propagation speed differed between the two methods. Speeds calculated from brightness temperature analyses are approximately twice as fast (~12 m s^{-1}) as those from DCA analyses (~7 m s^{-1}). As a reference, Johnson et al. (2005) used radar analyses to note that the typical propagation speed of convective systems during the period 16-25 May was around 6-10 m s^{-1} for systems organized perpendicular to the low level shear vector. Thus, the 7 m s^{-1} propagation speed suggested by DCA analyses is assumed to more accurately capture the propagation of convective systems away from the China coast.

To validate this assumption, it is first noted that brightness temperature analyses can be adversely affected by phenomena such as the decaying cirrus shields of dissipating convective systems, and cloudiness at warmer brightness temperatures. On the other hand, DCA focuses more on deep convective cloudiness by considering brightness temperatures < 230 K, and through a linear emphasis on colder brightness temperatures.

One hypothetical scenario that would produce higher propagation speeds in brightness temperature analyses is that of a decaying convective system in a sheared environment. As the cold cloud shield of the decaying system warms (Churchill and Houze 1984), it would no longer contribute significantly to DCA analyses. If wind speeds at cloud shield level were significantly faster than the system propagation speed, the decaying cloud shield would likely be advected downwind more rapidly than the system propagation speed. In this manner, DCA analyses, which are most affected by the coldest cloud tops, would be more likely to capture the

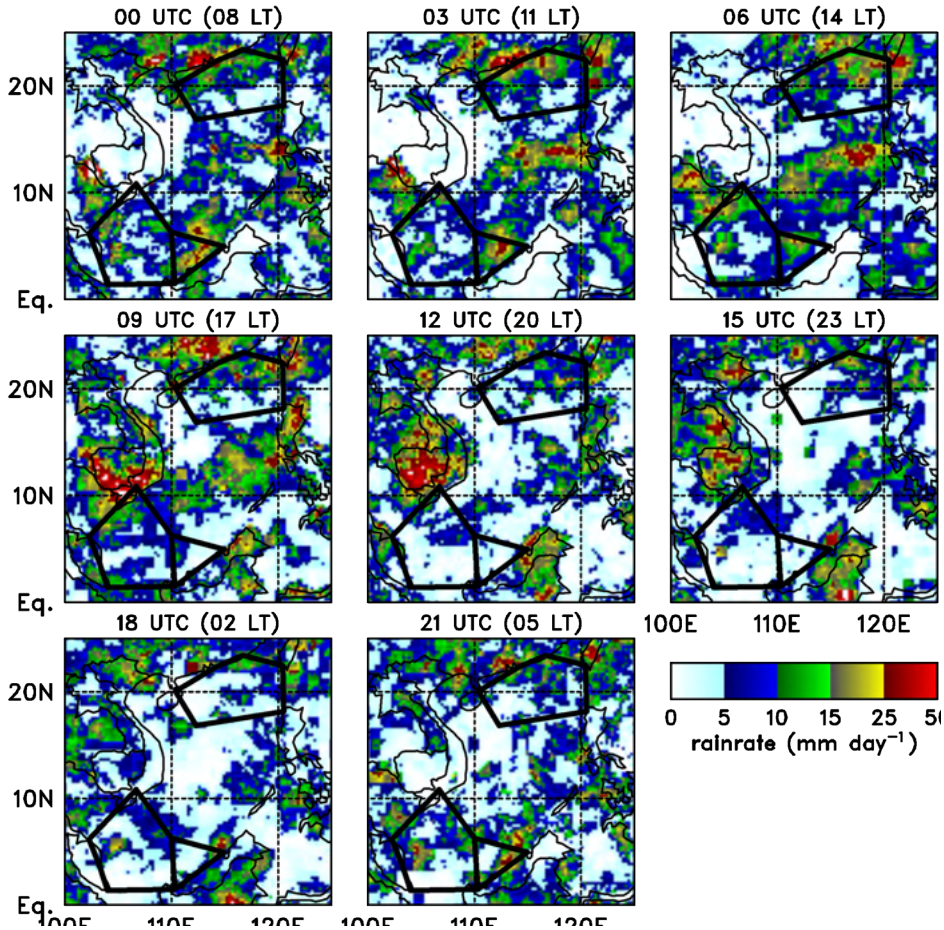

Figure 6.1 Three-hourly TRMM 3B42V6 rainfall maps averaged over May and June of 1998. As a reference, the polygon in the upper portion of each figure encompasses Dongsha Island and most of the northern SCS. (Taken from Ciesielski and Johnson, 2005).

propagation speed of the convective system, while brightness temperature analyses would be undesirably affected by the advection of the decaying cloud shield.

Several facts from the 1998 data suggest that this hypothetical situation may have been causing the discrepancy in propagation speeds. First, the significant brightness temperature propagation signal often extends farther from the coast than the DCA signal. This is true in subperiods PD1 and PD3 as well as the entire MYJN period. Second, Ciesielski and Johnson (2005) indicate that the diurnal cycle over the northern SCS is apparently caused by decaying

convective systems. To reach this conclusion, Ciesielski and Johnson (2005) used rainfall estimates from the 3-h, 0.25º resolution TRMM 3B42 version 6 microwave/IR merged rainfall product (Kummerow et al. 2000; Huffman et al. 2005) over May and June of 1998 (Figure 6.1). It is evident in Fig 6.1 that the diurnal cycle is a dominant feature throughout much of the SCS region. Over the northern SCS, early morning (~0600 LST) convective systems frequently initiated near the coasts, and gradually dissipated during the course of the day as mid-level steering currents pushed them away from the coastline. These decaying systems resulted in an early afternoon (~1500 LST) rainfall peak offshore, around the location of Dongsha Island. This analysis is based in part on direct measurement of hydrometeors, which is more credible than passive measures such as infrared radiances.

Finally, wind speeds perpendicular to the coastline are found to be fastest in the 100-300mb level, where cirrus shields are presumed to exist. Figure 6.2 shows the vertical profile of winds perpendicular to the southeastern China coast during the MYJN period (15 May-14 June) and over the northern SCS region (18-24ºN, 110-120ºE). To formulate this graph, average wind speeds are calculated and projected onto a vector whose orientation is perpendicular to the coast. Positive wind speeds indicate offshore motion, in the direction of system propagation. It is clear in Fig 6.2 that the highest component of wind in the direction of system propagation exists in the upper troposphere, where cloud shields of convective systems reside. However, the maximum speed in Fig. 6.2 (~8 m s^{-1}), while faster than the 7 m s^{-1} DCA propagation speed, is less than the 12 m s^{-1} calculated speed of propagation from brightness temperatures. Thus, the decaying cloud shield theory is not able to describe the discrepancy between DCA and brightness temperature propagation speeds and must be rejected.

With respect to previous literature, the average calculated propagation speeds fall into two categories. Faster speeds, around 15 m s^{-1}, were noted by Yang and Slingo (2001) in the Bay of

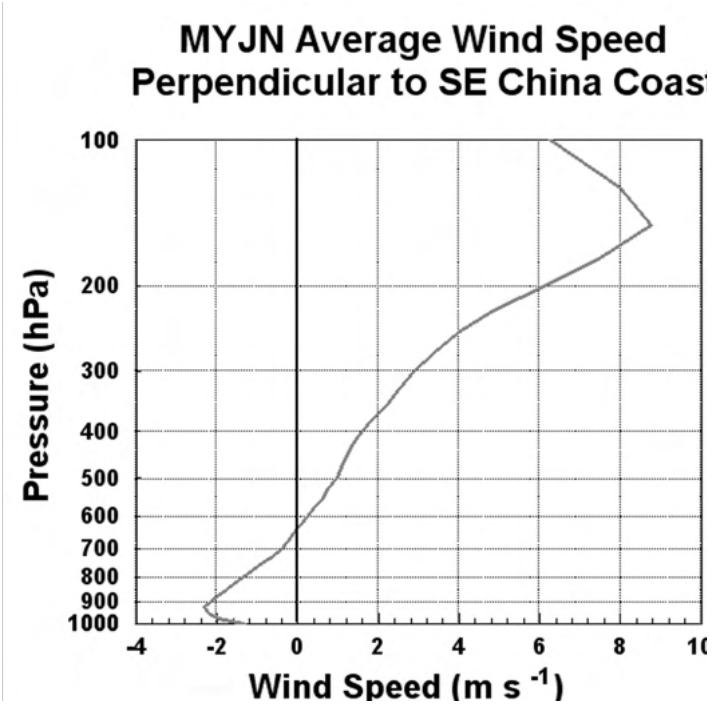

Figure 6.2 Average wind speed during the MYJN period (15 May-14 June 1998), projected onto a vector whose orientation is perpendicular to the southeastern China coast. In the figure above, positive wind speeds indicate offshore motion (from NW to SE).

Bengal (using the DCA index), by Mapes et al. (2003a,b) over the Panama Bight off the northwestern coast of South America (using the GOES Precipitation Index), and by Liberti et al. (2001) off the northern coast of New Guinea (using IR radiance). These fast speeds have been attributed to the motion of gravity waves, especially in the case of Mapes et al. (2003b), where a buoyancy perturbation at ~800 hPa was found to propagate away from raised terrain, preferentially initiating convection in its cold phase. Slower speeds, around 10 m s^{-1} or less, have been noted by Yang and Slingo (2001) in systems around the coast of Mexico and Indonesia, by Houze et al. (1981) off the coast of Borneo, and by Zuidema (2001) in the Bay of Bengal. These speeds are typically attributed to a combination of advection by steering currents and gravity current dynamics of the convective system and its resulting cold pool. Considering the higher propagation speed found in convective systems over the SCS in 1998, it is suggested that

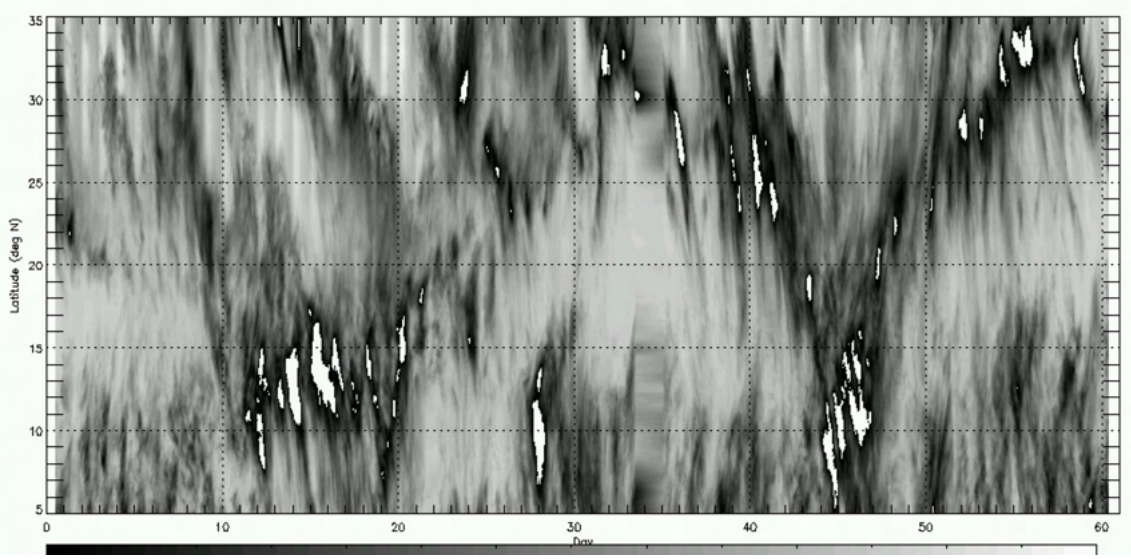

Figure 6.3 Longitude-time Hovmöller diagram of infrared brightness temperatures over the study region for May-June 2000. Values along the abscissa are days after 1 May 2000. Values shown are brightness temperature averaged over 116º-117ºE longitude, coinciding with the location of Dongsha Island.

advection and internal dynamics are too slow to accurately depict the propagation speed, as each predicts a speed of 7-8 m s^{-1}. Thus, gravity waves (similar to the sense of Mapes et al 2003a,b) are a likely candidate to describe the propagation signal in the northern SCS.

Of course, results thus fare are based on a single year of data. Much more confidence could be placed in the results if similar signals appear in multiple years. In addition to 1998 data, infrared satellite data for May and June of 1999 and 2000 were made available for this study. Unfortunately, a large amount (42%) of data were missing in the 1999 data set, especially during the period around monsoon onset which is the most convectively active period over the northern SCS. Analysis of this year was considered unrealistic and the data set was rejected. The data set for the year 2000 was much more consistent (8% missing), so it was examined to determine the diurnal cycle of convection during that year.

b. Comparison of 1998 and 2000 results

The examination of satellite data from the year 2000 is performed in a similar fashion to 1998 (as found in chapters 4 and 5). First, a time-latitude Hovmöller of infrared brightness temperatures (Figure 6.3) is considered to determine the most convectively active period of May-June 2000. As in Fig 4.2, the longitude band 116º-117ºE was used in this analysis to correspond with the location of Dongsha Island. In Fig 6.3, the onset of convection begins between 10º-15ºN around 12 May 2000. Convection remains in this region for around 10 days, with notable southward propagation of individual convective systems. The zone of convection rapidly shifts north of 25ºN (into southern China) in late May, where it remains until about 10 June. At this point, the central SCS becomes convectively active again through 17 June, after which the convective zone advances into China for the remainder of the month. Using Fig 6.3, the "MYJN" period for 2000 is determined to be from 12 May, which is the onset of convection over the SCS, through 17 June, after the final expansion of convection into China. One noticeable difference between the Hovmöllers of 2000 (Fig 6.3) and 1998 (Fig 4.2) is the lack of convection in the northern SCS (~18º-22ºN). Many systems formed around the 22ºN latitude of the southeastern China coast in 1998, but hardly any systems behaved this way in 2000.

To determine the average characteristics of convective activity over the region during MYJN 2000, averages of brightness temperature (Figure 6.4a) were calculated for 12 May-17 June. The general features in Fig 6.4a correspond with those from 1998 (Fig 4.4a), with the lowest brightness temperature averages over the Bay of Bengal, and the highest averages in the vicinity of the western Pacific subtropical high. To facilitate comparisons between Figs 4.4a and 6.4a, the difference between average brightness temperatures in 1998 and 2000 is displayed in Figure 6.4b. In constructing Fig 6.4b, brightness temperature averages during MYJN 2000 are subtracted from averages during MYJN 1998. In this manner, positive values in Fig 6.4b indicate more

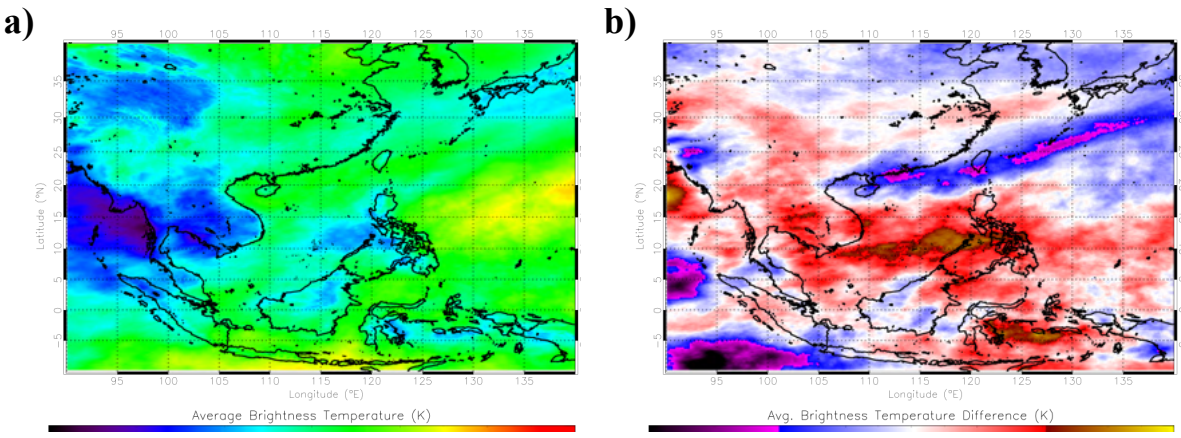

Figure 6.4 Comparison of convective activity between 1998 and 2000 using infrared brightness temperatures. In (a), the average brightness temperatures for the period 12 May-17 June 2000 are displayed. Figure (b) depicts the difference in average brightness temperatures between 1998 and 2000, calculated by subtracting the 2000 averages in (a) from the 1998 averages in Figure 4.4a. In this manner, positive values (red-brown) suggest more convective activity in 2000 than 1998.

convection in the year 2000. It is clear in Fig 6.4b that there is much less convective activity over the northern SCS and extreme southeastern China during MYJN 2000, in a band extending from the island of Hainan and Hong Kong to Taiwan and onward south of the Japanese Islands. Conversely, much more convective activity is suggested over the entire central and southern SCS.

Not surprisingly, variables more directly related to convection, such as the DCA index, paint the same picture of convective activity for MYJN 2000. Fig 6.5a illustrates the average DCA for MYJN 2000 in units of mm dy^{-1}. As compared with Fig 4.4d, much higher rainfall estimations are found over the central SCS, with a maximum exceeding 30 mm dy^{-1}. Lower values are found over the northern SCS in MYJN 2000, and the secondary maximum of DCA along the southeastern China coast in MYJN 1998 is completely missing in MYJN 2000. Similar to Fig 6.4b, the difference between average DCA values in 1998 and 2000 is depicted in Figure 6.5b. In this case, the DCA value from MYJN 2000 is subtracted from that in 1998, such that positive values indicated more satellite-estimated rainfall in 2000. Substantially higher DCA values

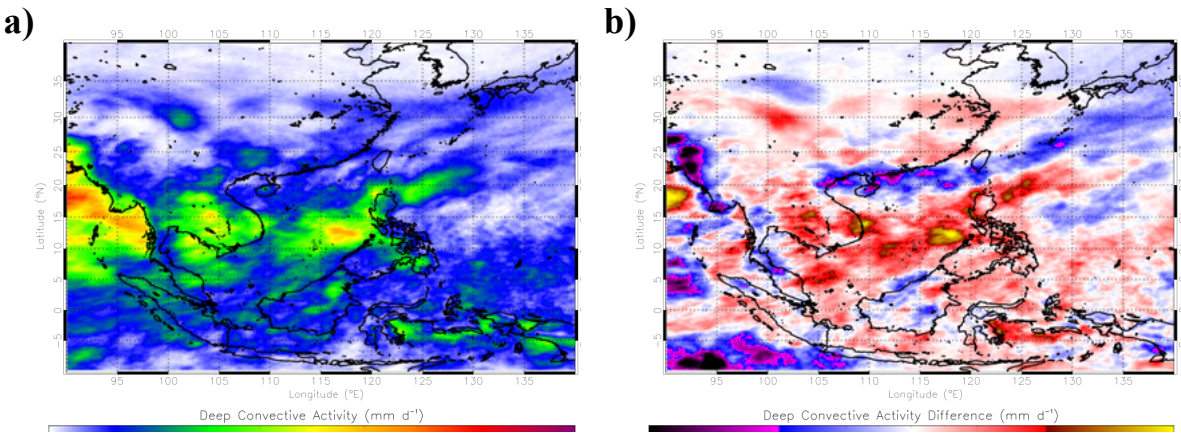

Figure 6.5 Comparison of convective activity between 1998 and 2000 using satellite-estimated precipitation. In (a), the average DCA values for the period 12 May-17 June 2000 are displayed. Figure (b) depicts the difference in average DCA between 1998 and 2000, calculated by subtracting the 1998 averages in Figure 4.4d from the 2000 averages in (a). In this manner, positive values (red-brown) suggest more convective activity in 2000 than 1998.

occurred in MYJN 2000 over nearly the entire central and southern SCS, while lower values extended along the southeastern China coast and the northern SCS.

In considering Figs. 6.4b and 6.5b, it is natural to question the reasons behind the departure in general convective patterns of 1998 and 2000. It appears as if the El Niño/Southern Oscillation is the most likely candidate to explain this difference. The period MYJN 1998 occurred at the end of one of the largest El Niño events in recent history, while MYJN 2000 was in the midst of a La Niña episode. Ciesielski and Johnson (2005) showed that 1998 rainfall, as compared to the 25-year mean (calculated from 1979-2003), was anomalously high over the northern SCS and southern China, and anomalously low elsewhere over the SCS and southeastern Asia. By regressing May/June Global Precipitation Climatology Project monthly rainfall maps (Adler et al. 2003) from 1979-2003 against the Niño 3.4 SST index, Ciesielski and Johnson (2005) found that, in El Niño years, precipitation generally increases in the northern SCS and southern China, and decreases elsewhere across the SCS region (Figure 6.6). Fig 6.6 agrees well with the difference maps of Figs 6.4b and 6.5b, suggesting that El Niño strongly influenced the distribution of

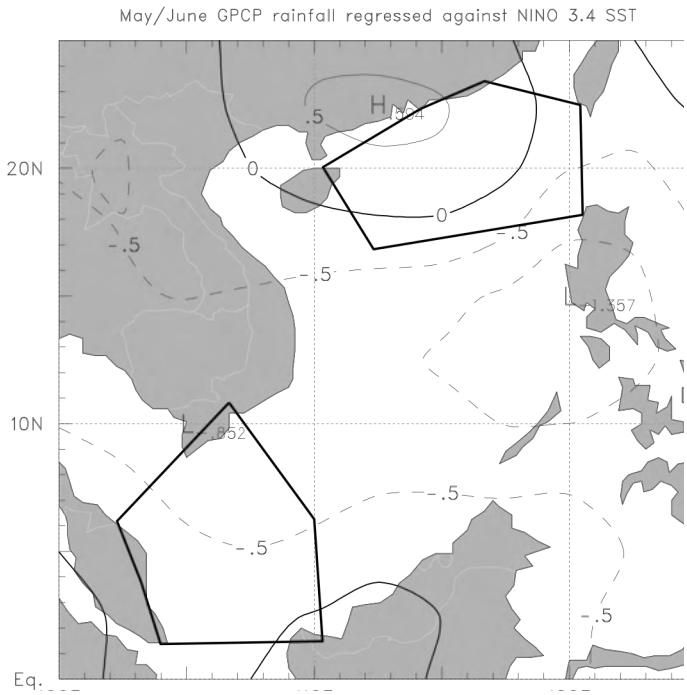

Figure 6.6 May/June GPCP monthly rainfall (mm dy^{-1}) regressed against the Niño 3.4 SST index. Stippled areas indicate regions where the regression coefficients are significant at the 95% confidence level based on a two-tail t-test assuming 25 degrees of freedom. (Taken from Ciesielski and Johnson 2005)

precipitation in 1998. One could infer that the physical reason for this El Niño-related precipitation anomaly includes the anomalous Walker circulation, whose subsident branch would tend to decrease convection over tropical latitudes in the western Pacific. Perhaps in this case, the moist low-level southwesterly monsoon flow can penetrate farther into the northern SCS and southern China, where land/sea breeze and terrain effects can induce convective formation in otherwise suppressed conditions. This speculation can be substantiated by considering the difference between the basin-wide diurnal cycles of convection in 1998 and 2000.

Figure 6.7 illustrates the difference in diurnal cycles by considering the extent of cold cloud coverage (< 208 K) during MYJN 1998 and MYJN 2000. In constructing Fig 6.7, only the satellite data points over water and between 10º-25ºN and 110º-120ºE are considered. It is

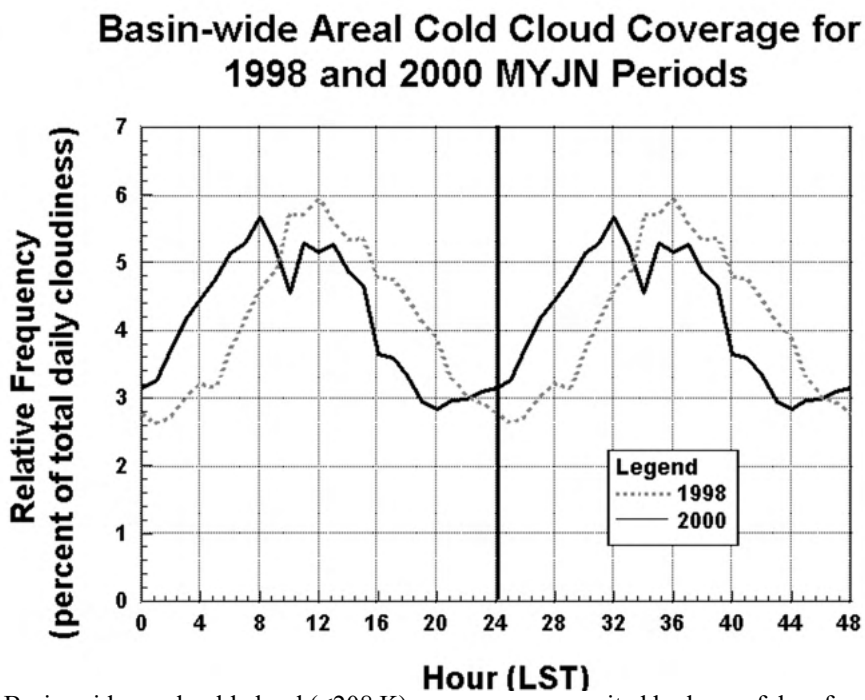

Figure 6.7 Basin-wide areal cold cloud (<208 K) coverage, composited by hour of day, for similar May-June periods in 1998 and 2000. The region considered include satellite data points over water and within the ranges of 10-25ºN and 110-120ºE. Relative frequencies are displayed using local solar time, and are repeated twice for the sake of clarity.

apparent that cold cloud coverage would suggest an earlier maximum of convective activity in 2000 as compared to 1998. The primary maximum of cold cloud coverage in 2000 occurs at 0800 LST, as compared to 1200 LST in 1998. Additionally, the minimum of cold cloud coverage occurs at 2000 LST in 2000, versus 0100 LST in 1998. Thus, it appears that the diurnal convective cycle of 2000 is shifted several hours ahead of that in 1998. It is also notable that a secondary maximum of cold cloud coverage is found around 1200 LST in 2000, coincident with the maximum coverage in 1998. Missing data during 2000 is distributed randomly among the hourly observation time, so the reason for this secondary maximum is not immediately clear.

Analyses of average convective activity differences between 1998 and 2000 over the SCS region were mixed, with more activity indicated over the central SCS, and less activity over the

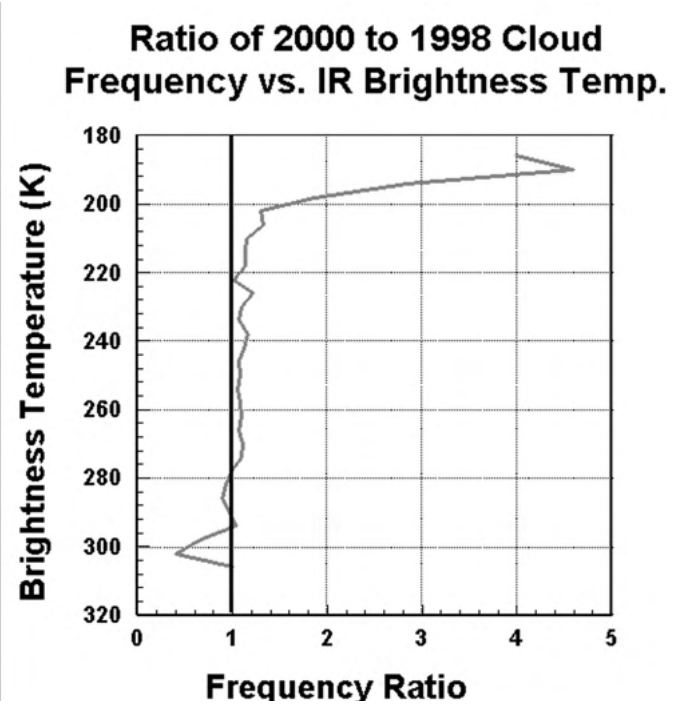

Figure 6.8 Ratio of the occurrence of clouds in 2000 versus 1998, as a function of brightness temperature. To calculate the ratio, the frequency distribution of clouds in 4 K brightness temperature bins for the year 2000 was divided by the distribution for the year 1998. Values greater than unity indicate more cloudiness in 2000 for the given brightness temperature bin.

northern SCS, in 2000 as compared to 1998 (Figs 6.4b-6.5b). Considering these figures alone, the difference in convective vigor between 1998 and 2000 is indeterminate. To better quantify this, a comparison is made between the frequency distributions of cloudiness in 1998 and 2000. Figure 6.8 depicts the ratio of the occurrence in clouds in 2000 versus 1998, as a function of infrared brightness temperature. To calculate the ratios in Fig 6.8, the frequency distribution of cloudiness in 4 K brightness temperature bins for MYJN 2000 was divided by the distribution for MYJN 1998. In this manner, values larger than unity in Fig 6.8 denote more cloudiness in 2000 than 1998, for a given brightness temperature bin.

Three main points can be inferred from Fig 6.8. First, there are generally fewer occurrences of "clear-air returns", with brightness temperatures roughly between 280 and 300K, in the year

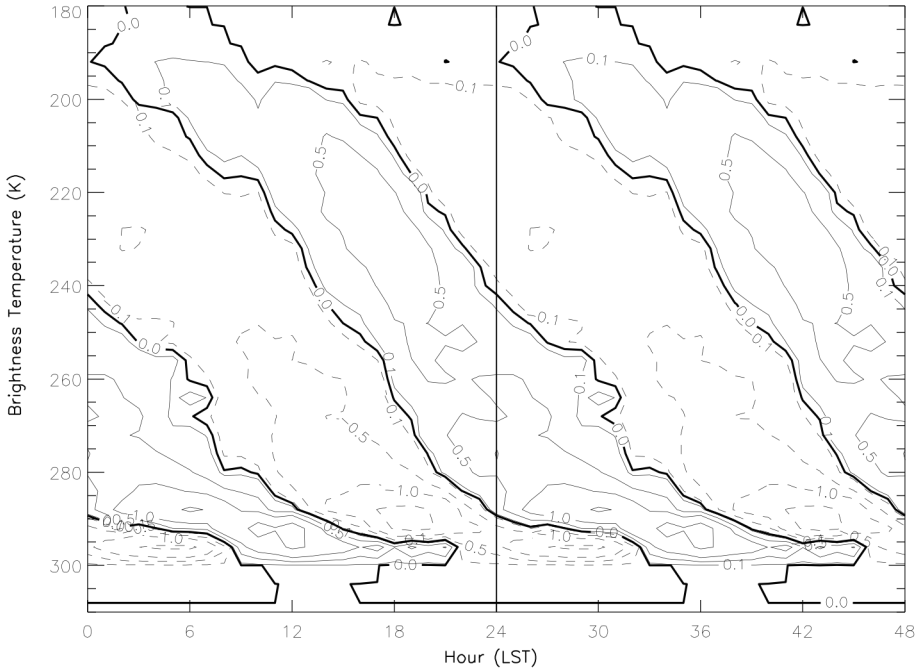

Figure 6.9 Basin-wide evolution histogram for the period 12 May-17 June 2000, calculated using satellite data points over water and within the ranges of 10-25ºN and 110-120ºE. Values shown are percentage anomalies, found by subtracting the daily mean histogram of brightness temperature from hourly composite histograms.

2000. This is particularly true around 300 K, with a frequency ratio of around 0.5, but this seems to be related to lower average values of clear-air returns in 2000 as compared to 1998. Second, there is generally more cloudiness in the year 2000, as the frequency ratio remains above unity for brightness temperatures cooler than 280 K. Third, there appears to be much more cloudiness with brightness temperatures below 200 K in the year 2000. The frequency ratio increases rapidly above this threshold, with over four times the cloudiness at ~190 K indicated in 2000 as compared to 1998. Thus, it appears that convection was more intense in the year 2000, as suggested by the significantly larger amount of extremely cold cloudiness.

While it is obvious that more high cloudiness occurred in MYJN 2000, the evolution histogram in Fig 6.9 demonstrates, in a diurnal sense, when this high cloudiness most frequently

occurred. As in Fig. 5.4, Fig 6.9 is calculated using satellite data points over water and within the ranges of 10-25ºN and 110-120ºE. Values shown are percentage anomalies, which are found by subtracting the daily mean histogram of brightness temperature from hourly composite histograms. In this manner, positive anomalies indicate when cloudiness of a given brightness temperature is more likely to occur, as compared to its daily mean occurrence. Between 1200 and 2400 LST, the evolution histograms of MYJN 1998 (Fig 5.4) and MYJN 2000 (Fig 6.9) look quite similar. Regarded as the decaying MCS signal (e.g. Chen and Houze 1997, Churchill and Houze 1984), clouds of increasingly higher brightness temperatures occur most frequently, in a diurnal sense, at increasingly later times of day. The behavior between 0000 and 1200 LST in Figs 5.4 and 6.9 are quite different, however. First, the contiguous MCS signal extends into colder brightness temperatures in MYJN 2000. The signal in 1998 terminated around 200 K, while the 2000 signal is coherent to 190 K. Second, the signal begins much earlier in the morning in MYJN 2000, with the very coldest of clouds suggesting a 0600 LST maximum of convection.

To punctuate the differences between Figs 5.4 and 6.9, an evolution histogram of the 2000:1998 cloudiness frequency ratio is presented in Figure 6.10. Fig 6.10 is quite similar to Fig 6.8, as values are calculated by dividing the hourly frequency distributions of cloudiness in MYJN 2000 by those for MYJN 1998. Quantities above unity (which are not shaded) indicate more cloudiness in 2000 versus 1998, for a given hour and brightness temperature. As in Fig 6.8, it is clear in Fig 6.10 that in MYJN 2000, there are generally fewer occurrences of "clear-air returns", and slightly more cloudiness, which Fig 6.10 suggest are true during the entire daily cycle. In contrast, Fig 6.10 implies that the greater occurrence in very cold cloudiness (< 200 K) in MYJN 2000 found in Fig 6.8 is confined to the late evening and morning hours, between 2000 and 0900 LST.

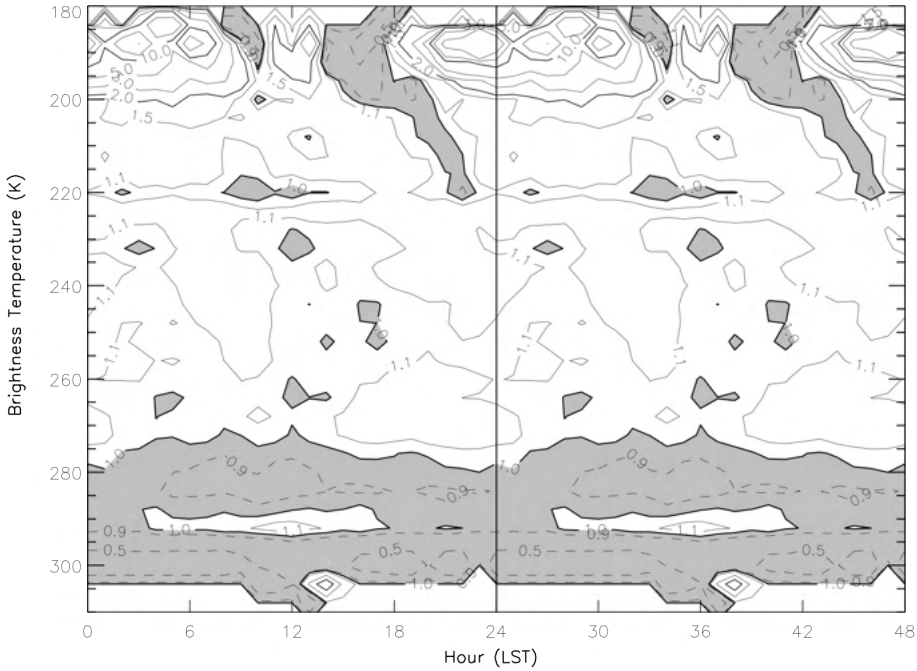

Figure 6.10 Ratio of the occurrence of clouds for similar May-June periods in 2000 versus 1998, as a function of brightness temperature and time of day. Values are calculated by dividing the hourly frequency distributions of cloudiness in 2000 by those for 1998. Quantities above unity are not shaded and indicate more cloudiness in 2000 versus 1998, for a given hour and brightness temperature.

By synthesizing the main points of this subsection, inferences about the nature of convective development in 2000 can be made. First, in Figs 6.4a-6.5a, it was found that there was more activity in the central SCS than the northern SCS in MYJN 2000. Statistics based on this period would therefore be biased towards the characteristics of convective development over the central SCS during that period. The times of maximum and minimum convective activity in MYJN 2000 were found to be around 0800 and 2000 LST, respectively (Fig 6.7). Figs 6.9 and 6.10 indicate that at the time of convective minimum, the occurrence of high cloudiness increases rapidly, both in a diurnal sense and in comparison to MYJN 1998. Considering these points, it is suggested that convective systems in MYJN 2000, which were most frequent over the central SCS, preferentially formed in the evening hours, reaching a maximum areal extent around 0600-0800

LST. This is in stark contrast to convective systems in 1998, which were found to develop more often in the morning hours, peak in size around noon, and dissipate in the late evening (Fig 5.9).

Comparing the characteristics of convection between 1998 and 2000 is much like the comparison between "suppressed" and "active" phases of the intra-seasonal oscillation in Chen and Houze (1997). While their comparison focused on Madden-Julian Oscillations over the western Pacific, it is plausible to infer that convection in 1998 is suppressed due to the negative impact of the strong El Niño and subsequent anomalous Walker circulation over the region. Consequently, convective systems in 1998 are small, less intense (as inferred by a lack of extremely cold cloudiness < 200 K), have a shorter lifespan, and more likely to be forced by land-sea breeze or terrain effects along the southeastern China coast. In 2000, a weak La Niña allowed for convective development over the central SCS that is more similar to that of the western Pacific systems of Chen and Houze (1997), forming through the late afternoon and night and reaching a maximum size in the morning hours.

The analyses of MYJN 2000 convection suggest that, due to the lack of convection over the northern SCS, the year may not be most suitable for the study of a propagation signal off the southern China coast. Indeed, measures of convection over the northern SCS, such as DCA-estimated precipitation and percent occurrence of high cloudiness (< 208 K) both suggest 40% less activity in 2000 as compared to 1998. Thus, most regressions following 1998 methods are not significant, considering amplitudes of the diurnal variations themselves are not that significant. However, regressions based on infrared brightness temperatures, with respect to distance from the China coast, did show some significance (based on larger regressed amplitudes) beyond 200 km from shore. Figure 6.11 shows the results of this analysis for MYJN 2000, superimposed over the results from MYJN 1998. As in Chapter 5, Figure 6.11 was constructed by considering the 115º-118ºE longitude range. Composite time series of brightness temperatures

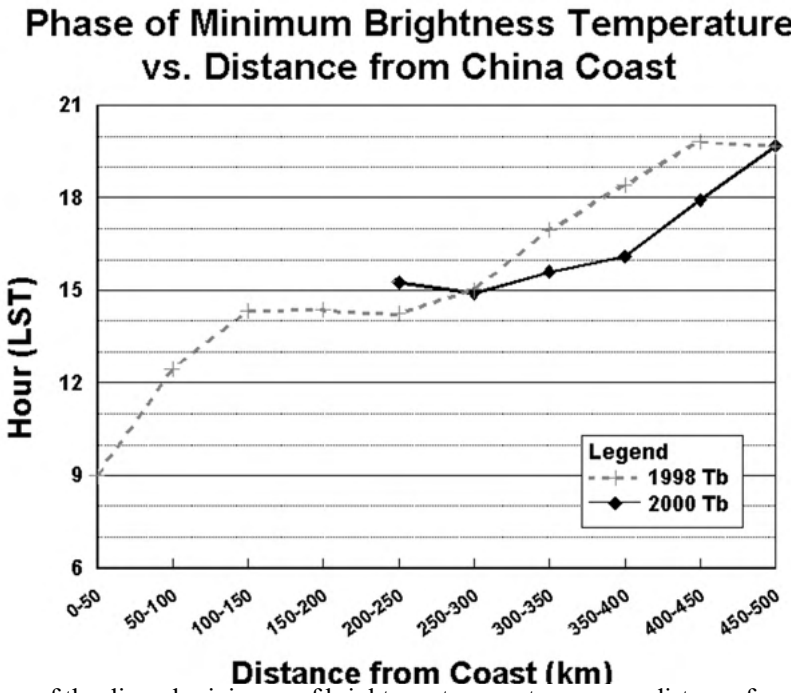

Figure 6.11 Phase of the diurnal minimum of brightness temperature versus distance from the southeastern China coast for similar May-June periods in 1998 and 2000.

for satellite data points in this range are averaged based on their distance from the coast. Regressions are then performed on these averaged time series to obtain information on the amplitude and phase of the diurnal variation. For 2000, the increase in the phase of minimum brightness temperature is almost monotonic with increasing distance, ranging from 1500 LST around the location of Dongsha Island to 2000 LST around 500 km from the coast. It is clear in Fig 6.11 that the propagation signals in 1998 and 2000 do overlap, with a maximum discrepancy of around 2 hr. The suggested propagation speed (13 m s^{-1}) and extrapolated phase of minimum brightness temperature at the coast (0900 LST) in MYJN 2000 also agree well with the values calculated for MYJN 1998.

This result suggests that the propagation signal found in1998 is indeed robust, as it appeared again in 2000, a convectively less favorable year for the northern SCS. Naturally, more years of

satellite data should be studied to lend credibility to the propagation signal analyses. In addition, the TRMM database, which has reached an acceptable size to overcome diurnal statistical shortcomings, provides another opportunity for validating the analyses.

Chapter 7: Conclusions and Future Work

In this study, the high-resolution data sets from GMS-5 satellite, C-POL Doppler radar, and enhanced observational sounding networks were examined to determine the diurnal characteristics of convective development over the South China Sea region during the monsoon onset of 1998. It is clear that a diurnal cycle of cloudiness existed over the SCS region, and a spectral analysis of the time series of cold cloud areal coverage confirmed that the diurnal cycle was significant with greater than 99% confidence.

In a diurnal sense, convective activity peaked in the early afternoon hours during May and June of 1998 over most of the SCS region. This timing was confirmed by various indirect measures of convection, including infrared brightness temperatures, areal extent of cold convective cloudiness, as well as more direct measures like C-POL Doppler radar observations and rainfall observations on Dongsha Island. A majority of satellite data points over the waters of the SCS had a minimum brightness temperature in the afternoon hours, suggesting that the average basin-wide results were not being skewed by one active region of the SCS. These results match well with previous fine-scale studies of the diurnal cycle of convection over the region, including Nitta and Sekine (1994) and Ohsawa et al (2001).

Over the northern SCS, the afternoon maximum of convection is suggested to be caused in part by the regular formation of systems along the southeastern China coast in the morning hours due to convergence of a land breeze and the onshore low-level monsoon flow. These systems preferentially propagated south- and eastward, or away from the coast through the afternoon

hours, greatly influencing the diurnal cycle of convection. This assertion is corroborated by Ciesielski and Johnson (2006), who utilized TRMM data to infer the afternoon maximum of convection over the northern SCS was caused by decaying MCSs. Reasons for the afternoon maximum of convection over the central SCS are less clear, but they could be related to suppressed atmospheric conditions over the region stemming from the strong El Niño during 1997-1998, and/or to the surface layer heating argument of Chen and Houze (1997).

Chen and Houze (1997) found that the diurnal cycle of convection depended on the active or suppressed state of the atmosphere over their TOGA COARE region of study. Convective activity was at a maximum during the morning hours in active phases, and in the afternoon during more suppressed conditions. Parallels can be drawn between the results of Chen and Houze (1997) and this study, as El Niño would act to suppress convection over the central SCS through increased subsidence in the descending branch of the anomalous Walker circulation at lower latitudes. However, caution must be exercised in these analogies. The "active" and "suppressed" phases in Chen and Houze (1997) pertained to the Madden-Julian Oscillation. Also, the suppressed conditions in Chen and Houze (1997) were characterized by smaller convective systems that had a relatively short lifetime, often three hours or less. But several systems in this study during 1998 were indeed large and had lifetimes of half a day or more.

In an average sense, the diurnal cycle of convection over the SCS region in May and June of 2000 peaked several hours earlier than that of 1998. This was attributed to an increase in convection over the central SCS, and a decrease over the northern SCS, in 2000 as compared to 1998. There was also a higher occurrence of very cold cloudiness in 2000, and evolution histograms implied that systems were longer-lived in 2000, with high cloudiness developing through the night to achieve a maximum areal extent in the morning hours. These comparisons between 1998 and 2000 convective trends led to the suggestion that conditions were more

suppressed during May and June of 1998. Cielsieski and Johnson (2006) showed that precipitation tended to be above average in the northern SCS and below average elsewhere in the SCS region during El Niño years, and a similar (implied) precipitation pattern was found in this study between 1998, and El Niño year, and 2000, a La Niña year.

This generalized, basin-wide statistical analysis of the convective diurnal cycle can only be understood within the context of a distinct propagation signal that was noted over the northern SCS in the vicinity of the southeastern China coast. This signal extended up to 500 km from the coast line across most of the northern SCS. The signal was characterized by a sunrise maximum of convective activity in areas immediately adjacent to the coast, steadily increasing to an early afternoon maximum in the vicinity of Dongsha Island, and finally to a late evening maximum where the signal was longer significant. The signal was apparent using both infrared brightness temperatures, as well as DCA indices, which focus more on cold cloud tops more relevant to convective activity. Additionally, the signal was evident within the limit scope of the C-POL Doppler radar located on Dongsha Island. Verification of the propagation signal among independent data sets, including more direct measures of hydrometeors as compared to infrared brightness temperatures, suggests the signal is indeed robust. The propagation signal examined during the period 15 May—14 June 1998 was also evident when dividing said period into three smaller subperiods, further reinforcing the notion that the signal was a robust aspect of the 1998 monsoon onset. Finally, the signal was even modestly apparent in May and June of 2000, a year in which convective development was much less pronounced over the northern SCS. Although marginally significant, this implies that the propagation signal is a robust aspect of convection over the region during the monsoon onset itself. This propagation signal is not unique to the SCS region, as it has been observed over the Bay of Bengal (Yang and Slingo 2001; Webster et al. 2002), the Panama Bight (Mapes et al. 2003a,b), and elsewhere adjacent to continents.

Though both brightness temperature and DCA analyses depicted a propagation signal, the implied phase speed differs between the two methods. Generally, speeds calculated using brightness temperature and radar data (averaging 12 m s^{-1}) are faster than those calculated using DCA data (averaging 7 m s^{-1}). It was suggested that decaying cloud shields could cause the discrepancy in propagation speeds. However, the maximum wind speed in a direction orthogonal to the China coast, around 8 m s^{-1}, are not fast enough to account for the brightness temperature propagation speed, so this explanation was rejected. It is also noted that the phase speed analyses were strongly sensitive to the input data, as variations within confidence intervals resulted in a 30% difference of propagation speeds. Though it is not clear why the speeds should differ, observations of the leading edge of cloud shields during PD3 (1-10 June) suggest a propagation speed of approximately 10 m s^{-1}.

An explanation of the mechanisms responsible for this propagation speed is difficult at best. This is especially true considering the inherently sparse network of sounding observations over the waters of the SCS, which does not lend to high-resolution studies of the diurnal trends of meteorological variables. Considering simple concepts, propagation speeds of 10-12 m s^{-1} could not be caused by advection of clouds in the upper troposphere, as average winds were found to be no greater than 8 m s^{-1} in the direction orthogonal to the coast. Speeds of this magnitude also cannot be caused by gravity current dynamics, as theory would suggest that the relatively weak cold pools observed around Dongsha Island (~ 3 K temperature differences) should propagate at 7 m s^{-1} in the absence of low level flow. The onshore flow associated with the monsoon would only act to reduce this propagation speed. Thus, while propagation speeds are not as fast as the ≥ 15 m s^{-1} speeds found by authors such as Mapes and Houze (2003b) or Yang and Slingo (2001), it is suggested that gravity wave dynamics may be responsible for the propagation signal speed over

the northern SCS, especially considering that more likely candidates for system propagation have been ruled out.

This study lends itself to future work in many different directions. First, it would be advantageous to examine more years of satellite data. The time period under consideration is relatively short, as it is confined by both the onset of convective activity over the region and the northward migration of convection out of the SCS and into southern China. Thus, the best way to increase statistical confidence of the above results is to include more yearly realizations of convective activity. In this manner, the existence of the propagation signal over the northern SCS, as well as the dependence of the diurnal cycle upon the strength of the El Niño oscillation, could be further tested.

Second, it would be useful to incorporate the complete set of TRMM data into the analysis of both the diurnal cycle and the propagation signal over the northern SCS. The precipitation radar onboard TRMM can directly measure hydrometeors, making it a useful tool in measuring the diurnal cycle of precipitation over the region as compared to indirect infrared measures. The global scope of TRMM also allows for analysis over the entire SCS region, as compared to the limited domain of ground-based radars. Finally, the temporal breadth of the data set is becoming sufficient to overcome any statistical difficulties of undersampling the diurnal cycle, as the satellite provides at most two observations at a particular point per day.

Finally, model simulations of the region would be an effective way to better determine the causes behind the diurnal cycle and the propagation signal found in this observational study. The enhanced sounding network from SCSMEX provides a viable initial data set for modeling. Assuming a reasonable output, the extremely high-resolution nature of model data would allow for better development of causality in the mechanisms of convective development. Mapes et al

(2003b) successfully employed a model to develop their gravity wave mechanism explanation of convective trends over the coastal Pacific waters off Panama.

Appendix A: Convective classification scheme

a. Purpose and history

One of the difficulties of using satellite brightness temperature data to diagnose convective activity lies in the extensive cloud shields that are produced by long-lived convective systems. Cirrus shields are typically thick enough to be opaque to infrared radiation, such that the brightness temperature measured by a satellite is approximately the ambient temperature at cloud top level. This opaqueness does not allow information from below cloud top level to be transmitted; a satellite would record the same cold cloud shield regardless of the cloud structure below it. Because of this fact, infrared brightness temperatures can only be used as a proxy for convective activity, through spatial and temporal correlations with accumulated precipitation and radar echoes (e.g. Arkin 1979; Janowiak and Arkin 1991). In addition, cloud shields can be slow to dissipate as compared to the convective updrafts that produce them, so focusing on cold cloud shields alone may give a false impression about the diurnal cycle of convective activity. To remedy these deficiencies, radar data were utilized from both Dongsha Island and Hong Kong radars, as radar reflectivity provides a much more direct measurement of precipitation and convective activity. Of course, not all precipitation in the radar domain was convective in origin. To best examine the nature of convective systems that passed through the radar domain, radar echoes were partitioned into their convective and stratiform contributions. This was beneficial in determining the diurnal cycle of convective cells in the radar domain, as well as the morphology

of convective systems, as more mature systems tend to produce more stratiform precipitation. (Leary and Houze 1979)

The most appropriate method of discriminating stratiform and convective precipitation regimes involves measuring the vertical air motion inside the precipitating cloud region. Houghton (1968) concluded that the distinction between the two regimes lies in the magnitude of the in-cloud vertical air motion and the timescale of the precipitation growth process. The majority of stratiform precipitation falls from clouds that extend above the freezing level, so ice particles must play an important role in the precipitation process. Steiner et al. (1995) define the existence of stratiform precipitation as when the vertical air motion satisfies the condition

$$|w| << |V_t|, \tag{A.1}$$

where V_t is the terminal fall velocity of snow particles, which is on the order of 1-3 m s^{-1}. Satisfying this condition, ice particles must fall, as vertical air motions are incapable of suspending the particles, and subsequent growth (through vapor deposition and aggregation) must also occur as the particles are falling. Eventually the aggregates melt; when viewed by radar, this melting layer appears as a horizontal "bright" band of intense echoes located ~0.5 km below the freezing level (Battan 1973). Convective precipitation processes are typified by vertical air motions that violate the above condition, and thus differ considerably from stratiform processes. Instead, precipitation particles are lofted by the strong updrafts, and precipitation particles grow primarily from the accretion of liquid water (Houze and Churchill 1984). Since updrafts are typically narrow, they are characterized by radar as well-defined vertical cores of maximum reflectivity, which contrast sharply with the horizontal bright band produced at melting level in stratiform precipitation. These differences in radar presentation form the basis of the partitioning algorithm used in this study.

There have been several approaches used to distinguish between convective and stratiform precipitation in radar data. Since the physical difference lies in the vertical velocity condition, data pertaining to vertical air motions would be ideal to distinguish between the two processes. Unfortunately, such data were not available for this study, so the structure of radar echoes outlined in the previous arguments will be used as a proxy for determining if the vertical velocity condition is satisfied. The technique must be refined, however, as the thin bright band signature of stratiform precipitation is not always evident using ground-based, volume scanning radars. Also, the bright band may also not be clearly defined during the early and late stages of stratiform precipitation development, or in regions where stratiform and convective precipitation are intermixed. Thus, observation of a bright band signature is a sufficient but not necessary condition for a precipitation region to be classified as stratiform, and an algorithm based solely on the existence of a bright band signature will tend to overestimate the convective contribution to total precipitation.

To combat this shortcoming, it was found to be more advantageous by some authors to approach the partitioning problem from the other direction. Churchill and Houze (1984) chose to focus on the two dimensional structure of convective cells as a basis for their algorithm. They found that convective cells were represented by a peak value of rain rate as compared to their local surroundings, whereas stratiform precipitation tended to be more horizontally homogeneous. Steiner and Houze (1993) refined this technique to apply to radar reflectivity, but concluded that the technique was overly sensitive to spatial resolution, and often incorrectly identified data points with moderate reflectivities and obvious bright band signatures aloft as convective cells.

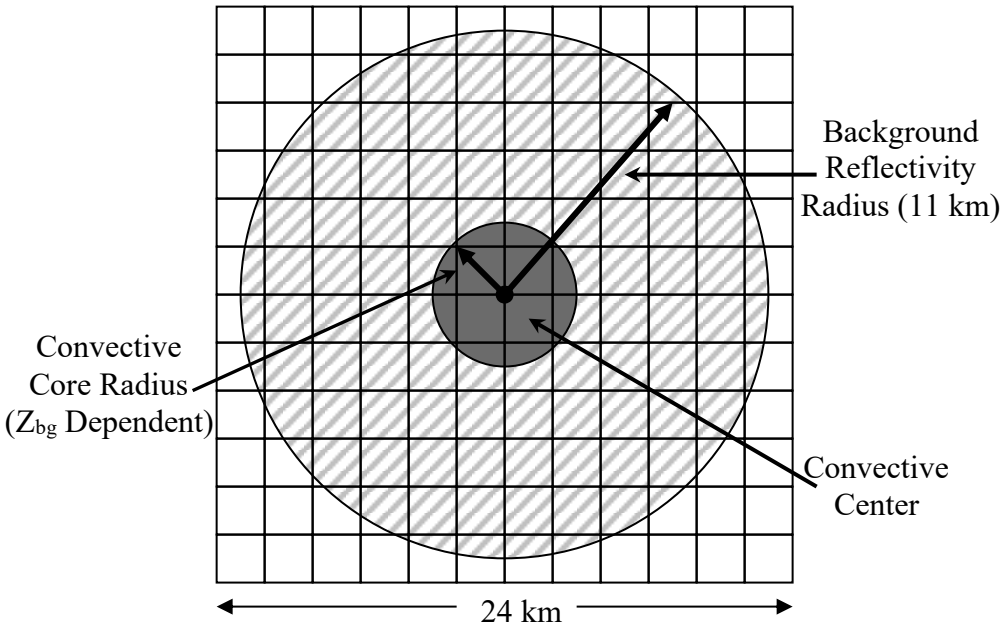

Figure A.1 This schematic diagram depicts the essential elements of a convective classification scheme that is based upon a convective cell's local maximum of reflectivity. The intersection of lines in the grid above represent grid points of reflectivity at the working level with a spacing of 2 x 2 km. The background reflectivity (Z_{bg}) is the linear average of all non-zero reflectivity data points within the background reflectivity radius. Points whose reflectivity exceed Z_{bg} by a given threshold are defined as convective centers, and points within a convective core radius of each convective center in the radar domain receive convective classification.

b. Steiner et al. (1995) algorithm description

Steiner et al. (1995) further refined the technique of Steiner and Houze (1993) to address these issues, and this result was the first-attempt partitioning algorithm utilized in this study. Their technique also searched for the local reflectivity maxima characteristic of convective cells, and points that are not classified as convective are stratiform by default. The algorithm first searched for "convective centers" which met their thresholds of intensity or peakedness, and then assigned all of the points within a background reflectivity-dependent "convective radius" of each convective center as being part of a convective core (Figure A.1). In terms of intensity, any point with a reflectivity that exceeded 40 dBZ was labeled as a convective center, through the argument that rain of such intensity could not be produced through stratiform processes. Any grid point whose reflectivity does not first meet the intensity requirement, but is higher than the background

reflectivity (Z_{bg}) at that point by at least the reflectivity difference ΔZ (defined below), is classified as a convective center because of its peakedness. Here, the background reflectivity is defined as the linear average of non-zero radar reflectivity, in the units of $mm^6\ m^{-3}$, within a radius of 11 km around the grid point. Steiner et al. (1995) used the piecewise function

$$\Delta Z(dB) = \begin{cases} 10, & Z_{bg} < 0 dBZ \\ 10 - Z_{bg}^2/180, & 0 \le Z_{bg} < 42.43 dBZ \\ 0, & Z_{bg} \ge 42.43 dBZ \end{cases} \quad \text{(A.2)}$$

which is itself a function of background reflectivity, to define the reflectivity difference threshold. The threshold function ΔZ has a maximum at low background reflectivity, making it more difficult for a smaller, weaker cell to be classified as convective. ΔZ decreases to zero at higher reflectivities, making it easier for the reflectivity maxima in larger, more intense convective cells and embedded cells in squall lines to be classified as convective centers. The threshold function was determined iteratively to match manual identification as closely as possible, and must be calibrated to each radar data set before it is applied. For each grid point identified as a convective center, all of the surrounding grid points within a "convective radius" of the convective center are also included as convective area. The convective radius is dependent on the background reflectivity, under the relatively intuitive but unreferenced assumption that more intense cells tend to be larger in spatial extent.

The partitioning algorithm operated on Cartesian-gridded reflectivity data at 3 km altitude. This height was chosen because it maximized the range of the radar (approximately 140 km) while still being low enough to avoid contamination from the bright band signature—the freezing level was around 5 km in their study. It was also assumed that the height was not too high above ground, such that evaporation in the tropical environment below 3 km altitude would not significantly change the precipitation pattern at those levels.

Yuter and Houze (1997) applied the algorithm of Steiner et al. (1995) to focus on raindrop size distributions of stratiform and convective precipitation regimes over the Pacific Warm Pool. They used almost exactly the same form of the algorithm, with a minor change to the reflectivity difference threshold function ΔZ

$$\Delta Z(dB) = a\cos\left(\frac{\pi}{2b} Z_{bg}(dBZ)\right), \tag{A.3}$$

and an increase of the reflectivity threshold. The values of a, b, and reflectivity threshold were tuned such that the resulting objective classification of reflectivity maps into stratiform and convective were most consistent with a subjective classification utilizing vertical cross sections. For the purposes of their study, Yuter and Houze (1997) used the values a=8, b=64, and a reflectivity threshold of 46 dBZ. The function ΔZ is similar in shape to that used in Steiner et al. (1995), but the parameters a and b are more intuitive and easily adjusted.

c. Steiner et al. (1995) algorithm performace

Upon utilizing the Steiner et al. (1995) convective partitioning algorithm in this study, with the updates included in Yuter and Houze (1997), it was found that the algorithm had difficulty in discriminating between different modes of convection with subjectively obvious differences in fractional convective contributions to total system precipitation. Johnson et al. (2004) noted a multitude of organizational types for convective systems in SCSMEX, whose structures were dependent upon the magnitude and orientation of the low- and mid-level wind shears and the existence of dry air aloft. One type of convective organization was characterized in reflectivity fields by thin lines of high reflectivity that were almost entirely convective in nature, while other types had more of a classic leading convective-trailing stratiform presentation. Wang and Carey

(2003) also reported the existence of the convective configuration similar to the leading stratiform systems depicted in Parker and Johnson (2000). However, results from the algorithm of Steiner et al. (1995) suggest that these differing organizational archetypes had similar fractional convective contributions, which is easily shown to be inaccurate.

Biggerstaff and Listemaa (2000) also found the Steiner et al. (1995) algorithm to be deficient in their study of convection around Houston, Texas. They concluded that the algorithm did not include enough of a convective cell in its "convective radius", falsely classifying a large number of grid points with weak reflectivities on the fringes of convective cells as stratiform. The algorithm performed particularly poorly when disorganized, isolated convection was present, by underestimating both the convective rain and convective area fractions by a significant amount. The same problem was found to exist in this study, exemplified both through subjective comparisons of radar reflectivity and echo classification fields as described above, and through examining the histogram of reflectivity for all points that are classified as convective. Another observation in Biggerstaff and Listemaa (2000) was that the Steiner et al. (1995) algorithm incorrectly identified enhanced areas of stratiform precipitation as convective. This problem was evident in high reflectivity stratiform regimes, because the peakedness criterion is easily met in regions of high background reflectivity, and the Steiner et al. (1995) algorithm assumes reflectivities greater than 40dBZ to be solely associated with convection. Subjective analyses of vertical cross-sections of reflectivity often revealed the presence of a well-defined bright band over these misclassified points, and even though the algorithm was applied at a data level well below the bright band, the localized regions of enhanced stratiform precipitation at the data level were still able to meet the peakedness criterion.

The case against using the Steiner et al. (1995) algorithm in this study can be strengthened by examining its performance on the available radar data. Because there are not vertical velocity

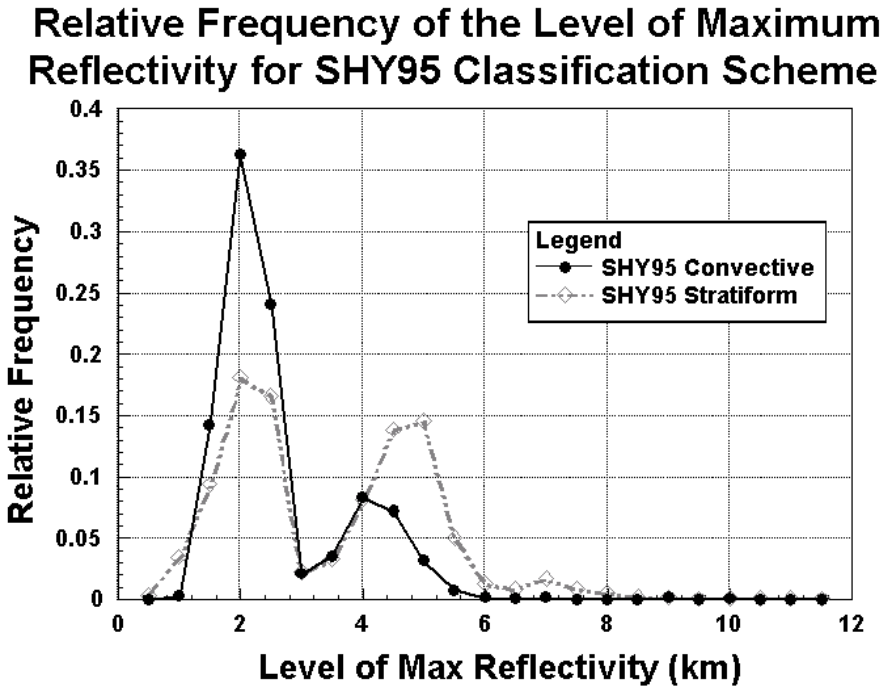

Figure A.2 Relative frequency of the level of maximum reflectivity for points with convective and stratiform classifications using the Steiner et al. (1995, SHY95) algorithm. Note the large frequency of convective classification for points with maximum reflectivities in the bright band region between 3.5 and 6km.

data available to complement the radar reflectivity information, the only real test for error involves the existence of a bright band signature, as this has been shown to be a sufficient condition for stratiform classification. One of the goals in algorithm selection is to minimize the number of convectively classified data points with obvious bright band signatures in their vertical profiles of reflectivity. Figure A.2 shows the distribution of the level of maximum reflectivity for data points labeled convective and stratiform by the Steiner et al. (1995) algorithm. The misclassification of stratiform points as convective is evident, as over 20% of the points receiving convective classification have maximum vertical reflectivities in the 3.5-6.5 km layer (found by integrating under the curve), which was defined as the layer in which the bright band should reside. This would indicate a large number of misclassified points and relatively poor algorithm performance.

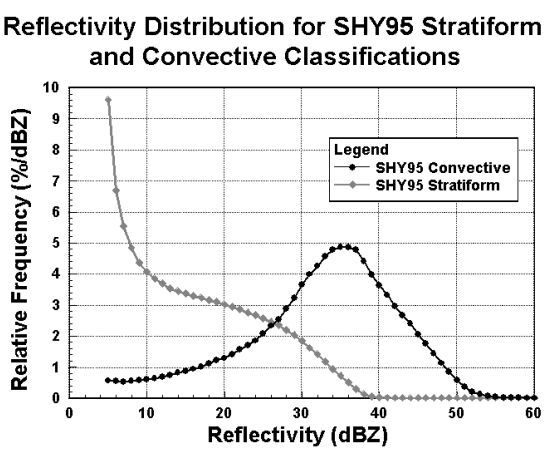

Figure A.3a Distribution of reflectivity, in 1 dBZ increments, at the 2.5km vertical level for data points classified as stratiform and convective by the partitioning algorithm discussed in Steiner et al. (1995, SHY95).

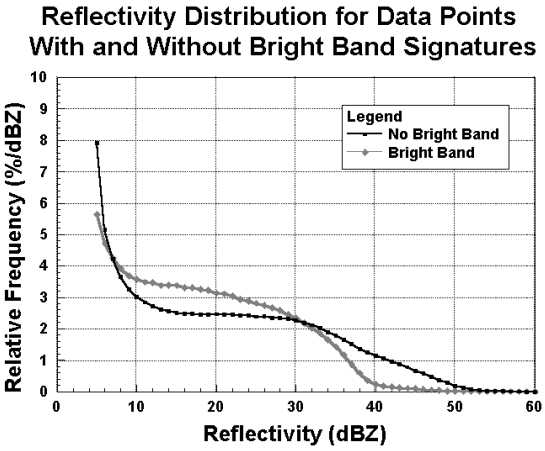

Figure A.3b Distribution of reflectivity, in 1 dBZ increments, at the 2.5km vertical level for points with and without bright band signatures in their vertical reflectivity profiles.

To further investigate the inappropriateness of using the Steiner et al. (1995) partitioning algorithm for this study, it is advantageous to subdivide the data into both stratiform and convective classifications, and into categories based on whether or not data points exhibited bright band signatures. Since the existence of a bright band is the only true test of stratiform classification in the absence of vertical velocity data, it follows that for a properly functioning classification algorithm, the frequency distributions and correlations of key radar parameters (i.e. reflectivity) should be similar for stratiform classifications and points with bright band signatures.

Inferences can also be made about similar comparisons between convective classifications and points without bright band signatures, although caution must be exercised, as points without bright band signatures are not necessarily convective by default. In any event, marked departures from the bright band signature distributions would indicate that the convective partitioning algorithm is not able to capture the essence of the distinction between convective and stratiform precipitation regimes, which would be an undesirable result. Figure A.3a shows the distribution

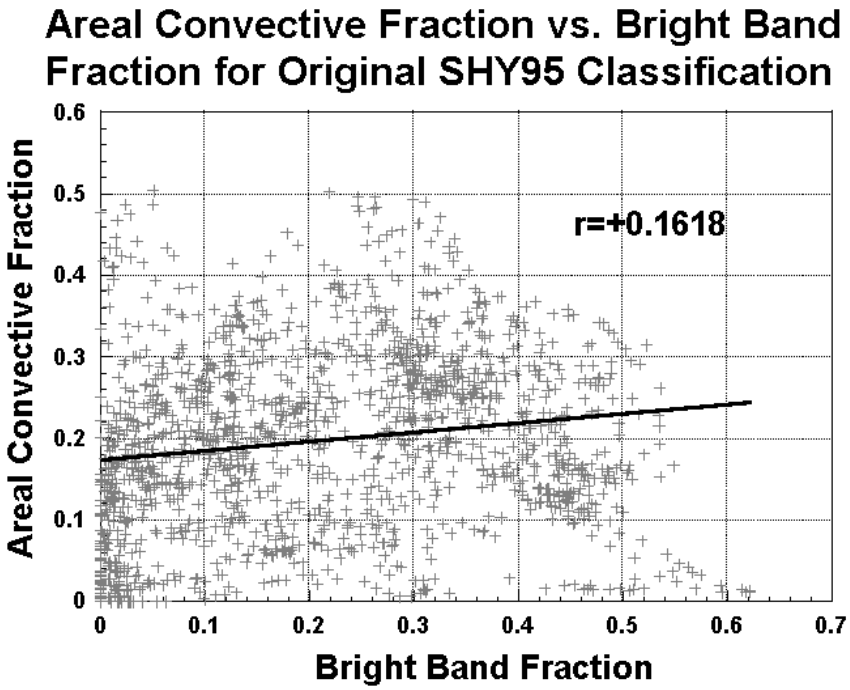

Figure A.4 Correlation between areal convective fraction, as calculated by the Steiner et al. (1995) partitioning algorithm, and the bright band fraction. To indicate good algorithm performance, these two variables should be exactly negatively correlated with each other.

of reflectivity at the 2.5 km level for data points classified as stratiform and convective by the Steiner et al. (1995) partitioning algorithm. For comparison, Fig. A.3b shows the distribution of reflectivity at the same level for data points with and without bright band signatures in their vertical reflectivity profiles. In Fig. A.3b, the frequency distribution of reflectivity exhibits a monotonic decrease with increasing reflectivity for both points with and without bright bands. However, the frequency distribution of reflectivity for data points with a Steiner et al. (1995) convective classification (Fig. A.3a) shows a distinct maximum around 36 dBZ. This exemplifies the fact that the Steiner et al. (1995) partitioning algorithm tends to focus solely on the high-reflectivity inner core of convective cells without including enough of the low-reflectivity data points on the fringe of such cores. Also of note is the lack of stratiform points with reflectivities > 40 dBZ, as compared to the distribution of bright band data points. This would indicate that the

Steiner et al. (1995) algorithm is not adequately capturing the high-reflectivity stratiform regime as discussed earlier.

Another good test for a partitioning algorithm is to examine the correlation between its predicted areal convective fraction (that is, the ratio of convectively classified data points to the total number of classified data points) and the bright band fraction over the entire radar domain. Although the number of points exhibiting a bright band signature is generally lower than the number of points deserving a stratiform classification, these two variables should tend to be negatively correlated with one another. Figure A.4 depicts the correlation between the areal convective fraction calculated by the Steiner et al. (1995) partitioning algorithm and the bright band fraction for each volume scan. Surprisingly, the correlation is weakly positive, which is a very undesirable result. It appears as if the relationship between the two variables in Fig. A.4 is non-linear in nature, with a tendency for negative correlation in high bright band fraction situations, but a strong positive correlation for low bright band fractions. This would indicate that the Steiner et al. (1995) partitioning algorithm has difficulty with low bright band fraction situations, which are likely indicative of a regime of isolated convective cells.

d. The Biggerstaff and Listemaa (2000) algorithm modification

In order to improve algorithm performance, Biggerstaff and Listemaa (2000) proposed modifications to the two-dimensional Steiner et al. (1995) scheme that included vertical information and greatly improved their results over their southern Texas domain. They found that for their particular situation, criteria involving the vertical lapse rate of reflectivity above the maximum level of reflectivity (Toracinta et al. 1996), the bright band fraction (Rosenfeld et al. 1995), the horizontal gradient of reflectivity (Rosenfeld et al. 1995), and the magnitude of reflectivity aloft could be used to modify the initial Steiner et al. (1995) algorithm output, such

that points were reclassified if they met certain combinations of the above criteria. After the original output was reclassified, Biggerstaff and Listemaa (2000) applied a smoothing routine to the reclassified data for the sake of spatial continuity. The results of the modified classification algorithm tended to better match the distinguishing patterns in vertical cross sections of reflectivity, and thus were assumed to be more representative of the precipitation production regimes that the algorithm was attempting to diagnose. Biggerstaff and Listemaa (2000) found that their modified classification algorithm produced higher areal convective fractions for unorganized (isolated) convective events, and similar areal convective fractions for organized events, and this fact was attributed to the inability of the Steiner et al. (1995) algorithm to adequately capture the fringes of convective cores. With respect to convective rain fraction, Biggerstaff and Listemaa (2000) noted that the fraction decreased for organized events, even though the areal convective fraction remained relatively constant. This was caused by the misclassification of strong stratiform precipitation cells as convective, which had more of an influence upon total rainfall than the numerous convective fringe points that were misclassified as stratiform.

Unfortunately, the modifications used by Biggerstaff and Listemaa (2000) cannot be appropriately applied to this study, as they were engineered for midlatitude mesoscale convective systems. For example, Biggerstaff and Listemaa (2000) use the vertical lapse rate of reflectivity above the level of maximum reflectivity as a way to differentiate between stratiform and convective precipitation regimes. However, Steiner et al. (1995) show the average vertical lapse rate of reflectivity for tropical convective and stratiform precipitation regimes to be very similar ($\sim$ -2.5dBZ km^{-1}) above the level of maximum reflectivity. The reflectivity aloft, which is defined as the reflectivity at the level that is roughly twice the height of the level of maximum reflectivity, showed the same inability to differentiate between the two precipitation regimes for this study. Additionally, the horizontal gradient criterion, which Biggerstaff and Listemaa (2000)

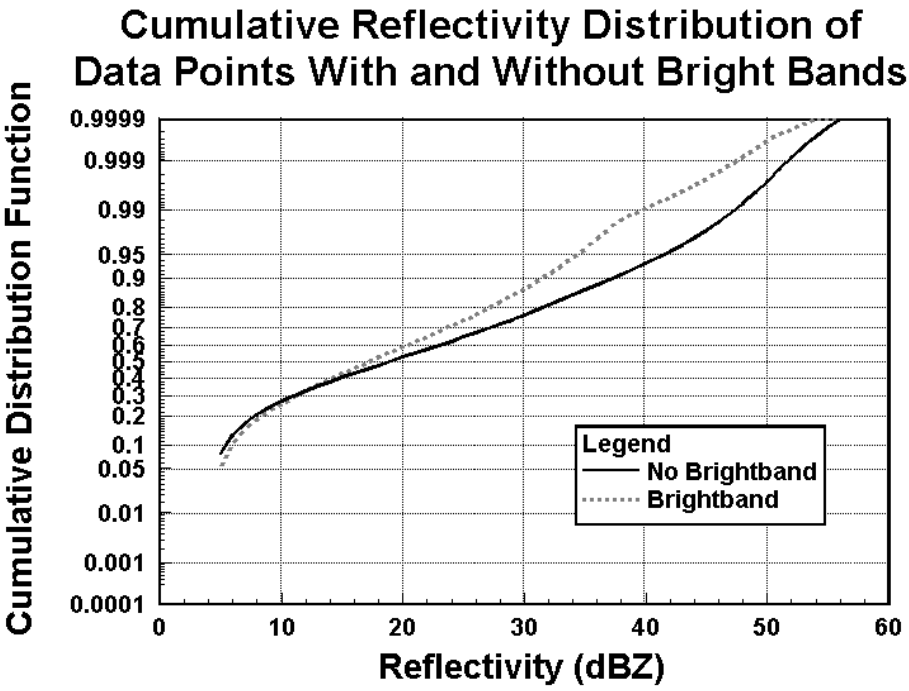

Figure A.5 Cumulative distribution of reflectivity at a vertical level of 2.5 km for data points that exhibit the existence or lack of a bright band signature.

indicated would be higher in the fringes of convective cells than in stratiform precipitation areas, had difficulty distinguishing convective fringe points from the trailing edge of stratiform precipitation, which were often found to be very distinct in this study. Realizing these deficiencies, it was determined that a new partitioning algorithm should be developed for this study.

e. The new convective partitioning algorithm: Design

The new algorithm utilized the most attractive aspect of previous partitioning algorithms: the peakedness requirement. Since convective cells are always depicted by local maxima in low-level horizontal reflectivity fields, it follows that these convective centers, which are easily discovered by objective procedures, should form the basis of stratiform/convective partitioning. The problem, then, is which points should be included as being part of the convective cell, and

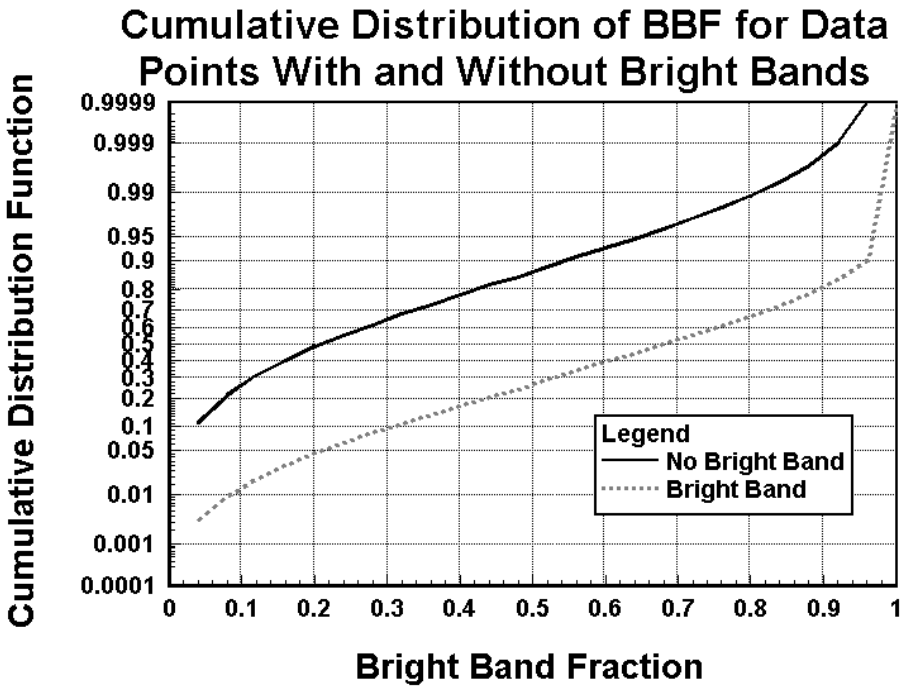

Figure A.6 Cumulative distribution of bright band fraction for data points that exhibit the existence or lack of a bright band signature.

what criteria should be imposed to best differentiate between convective and stratiform precipitation regimes. To solve this, frequency distributions of variables based on local patterns of horizontal and vertical reflectivity are compared for points with and without bright band signatures in their vertical reflectivity profiles. Since the existence of a bright band is the only definitive test for stratiform precipitation, it is intuitive that variables that show skill in discriminating between data points with and without bright bands should also be beneficial in convective classification algorithms. Figures A.5-A.7 show the cumulative frequency distribution of three variables that were found to have the highest differentiation skill. The distribution of reflectivity at the 2.5 km vertical level is shown in Fig. A.5, and while there is not a large amount of separation between points with and without bright band signatures, Fig. A.5 does indicate that 99% of stratiform points have reflectivities below 40 dBZ. This is the same

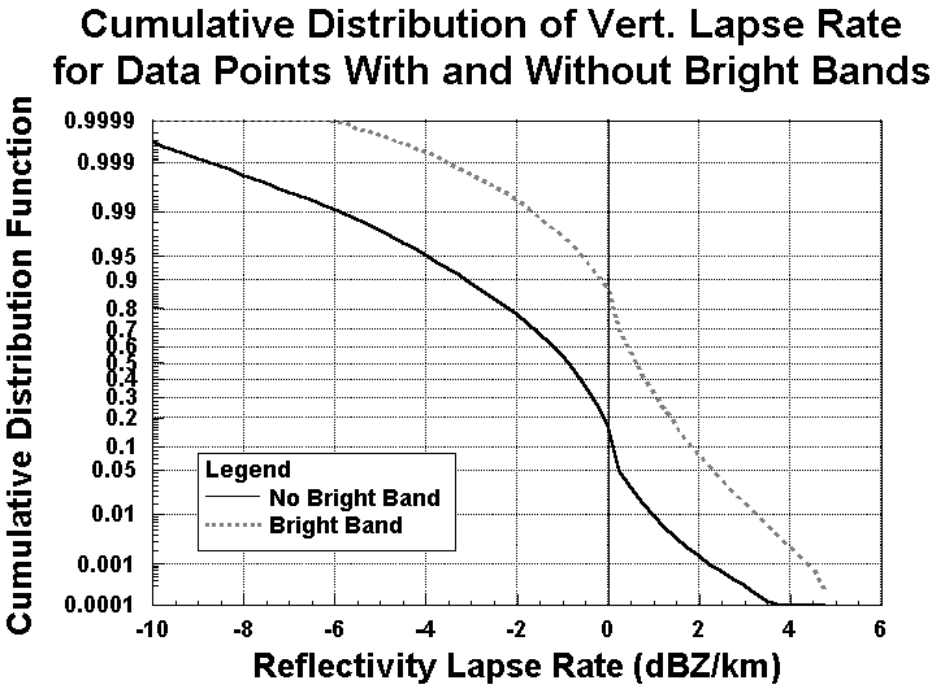

Figure A.7 Cumulative distribution of the vertical reflectivity lapse rate, calculated for the 3km-5km layer, for points that exhibit the existence or lack of a bright band signature.

threshold that was used in Steiner et al. (1995), but its implementation in that study was too strict, as will be discussed later.

Fig. A.6 shows the cumulative distribution of bright band fraction (BBF, Section 3.b.2) for points with and without bright band signatures in their own vertical reflectivity profiles. The BBF of a given data point is calculated in a 7 km x 7 km window surrounding said point, and Fig. A.6 illustrates the correlation between the calculated BBF and the existence (or lack) of a bright band signature at said point. As expected, there is a huge separation in the subdivided data, with a maximum in separation at a BBF value of 0.5. At this threshold, approximately 85% of points with no bright band have a lower value of BBF, and approximately 75% of points with a bright band signature have a higher value of BBF. This result exemplifies the utility of such a threshold in discriminating between convective and stratiform precipitation regimes.

Finally, the cumulative distribution of the vertical lapse rate of reflectivity between 3 km and 5 km is shown in Fig. A.7. This concept is similar to the vertical lapse rate argument of Biggerstaff and Listemaa (2000), but it pertains to fixed vertical levels rather than a variable level of maximum reflectivity. The fixed levels were chosen to coincide with the level of reflectivity used for most calculations in this study as well as average vertical height of the freezing level, which was found to be around 5 km. According to the average vertical profiles of reflectivity calculated by Steiner et al. (1995), the lapse rate should be negative for convective points, whose vertical reflectivity profile decreases monotonically with respect to height. Conversely, the vertical lapse rate should be positive for stratiform points, with a bright band located ~ 5km. Fig A.7 validates this assertion, with 85% of points with no bright band signature having a negative reflectivity lapse rate, and 85% of points with a bright band signature having a positive reflectivity lapse rate. Even so, it was found to be more beneficial to use a criterion of -3 dBZ km^{-1} to define convective areas. This low value was chosen empirically because it was found that data points on the edge of stratiform precipitation areas also possessed slightly negative vertical lapse rates in the 3-5 km layer, but data points on the fringes of convective cores often had even more negative lapse rates.

The final result of these efforts was to construct a convective partitioning algorithm that was based on the strengths of Steiner et al. (1995), but was fine-tuned to the radar data set used in this study by taking advantage of the differences between data points that did or did not exhibit bright band signatures. The new partitioning algorithm begins by finding all of the convective centers in the 2.5 km (working level, Section 3.2.c) horizontal reflectivity field. A convective center is a point whose reflectivity, Z_h, exceeds the background reflectivity by at least ΔZ, where

$$\Delta Z = \begin{cases} 5.0\ dB, & 5 \le Z_h < 40\ dBZ \\ 2.5\ dB, & Z_h \ge 40\ dBZ \end{cases} . \qquad \text{(A.4)}$$

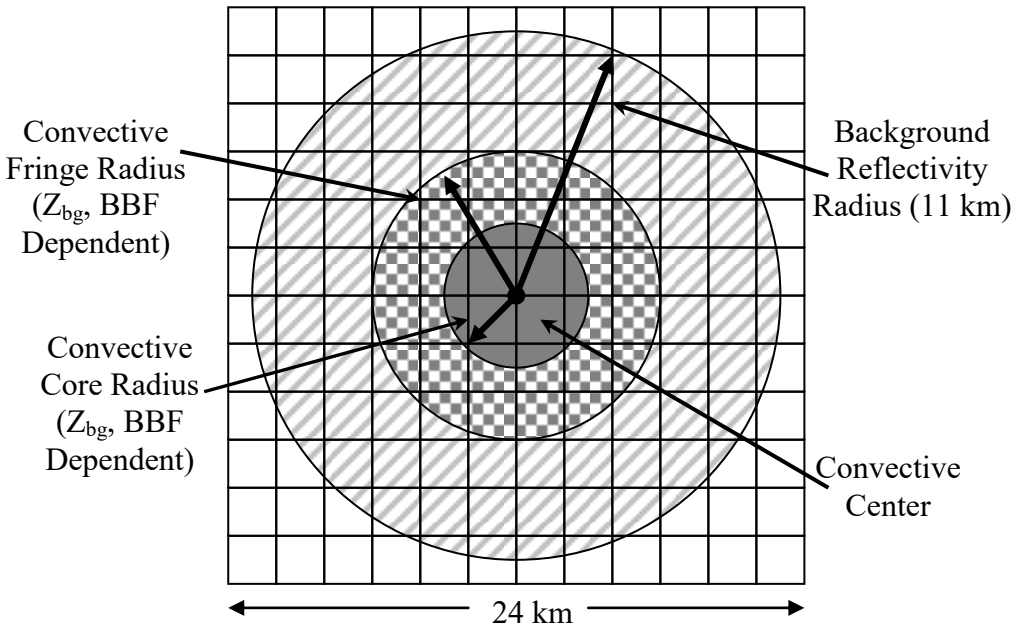

Figure A.8 This schematic diagram depicts the essential elements of the new convective partitioning algorithm designed for this study. In addition to the definitions of Steiner et al. (1995), this algorithm also includes a convective fringe radius, whose length is twice that of the convective core radius.

The function ΔZ deviates from the Steiner et al. (1995) reflectivity difference function (A.2) in two ways: ΔZ is smaller than (A.2) at low reflectivities to include more of the weaker convective cells, and larger at high reflectivities to exclude the areas of enhanced stratiform precipitation. Unlike Steiner et al. (1995), to be considered a convective center, the points that exceed the background reflectivity by at least (A.4) are also required to have a level of maximum reflectivity at or below 3.5 km. This level is specifically chosen because if the level of maximum reflectivity is found to be higher than 3.5 km, it is likely that the point is located in an area of enhanced stratiform precipitation and should not be included as a convective center.

Once all of the convective centers are identified in a horizontal reflectivity field, the data points within two distinct radii, named "convective core radius" and "convective cell radius" for the purposes of this study, are tested for convective classification (Figure A.8). The lengths of these radii are dependent on the reflectivity and BBF at the convective center. Higher values of

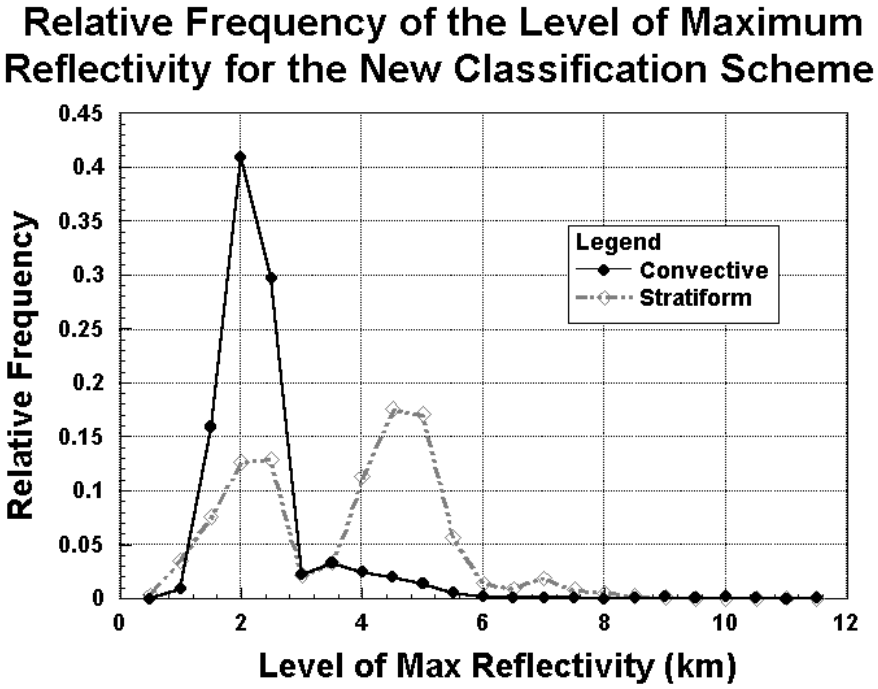

Figure A.9 Relative frequency of the level of maximum reflectivity for points with convective and stratiform classifications using the algorithm developed for this study. Note the reduction in frequency of convective classification for points with maximum reflectivities in the bright band region between 3.5 and 6km as compared to the Steiner et al. (1995) algorithm (Fig. A.2).

reflectivity in the convective center suggest a larger convective radius (Steiner et al. 1995), assuming a relatively constant horizontal reflectivity gradient. Higher values of BBF (> 0.5) at the convective center are chosen to penalize the convective radius slightly, such that there is a diminished chance that stratiform points are considered in the convective assignment process. Additionally, the convective fringe radius is twice the length of the convective core radius. Within the convective core radius, data points with attributes typical of a convective core are given a convective classification. This conditional classification is another fundamental difference between this convective classification scheme and that used by Steiner et al. (1995). Only the points with $Z_h \geq 40$ dBZ, or with $Z_h \geq 5$ dBZ *and* a BBF ≤ 0.5 are given a convective classification. Within the convective fringe radius, data points are given a convective classification if they meet all of the following criteria found to exist along the fringe of convective cells: $Z_h \geq 5$ dBZ, BBF ≤ 0.5, level of maximum reflectivity ≤ 3.5 km, and 3-5 km

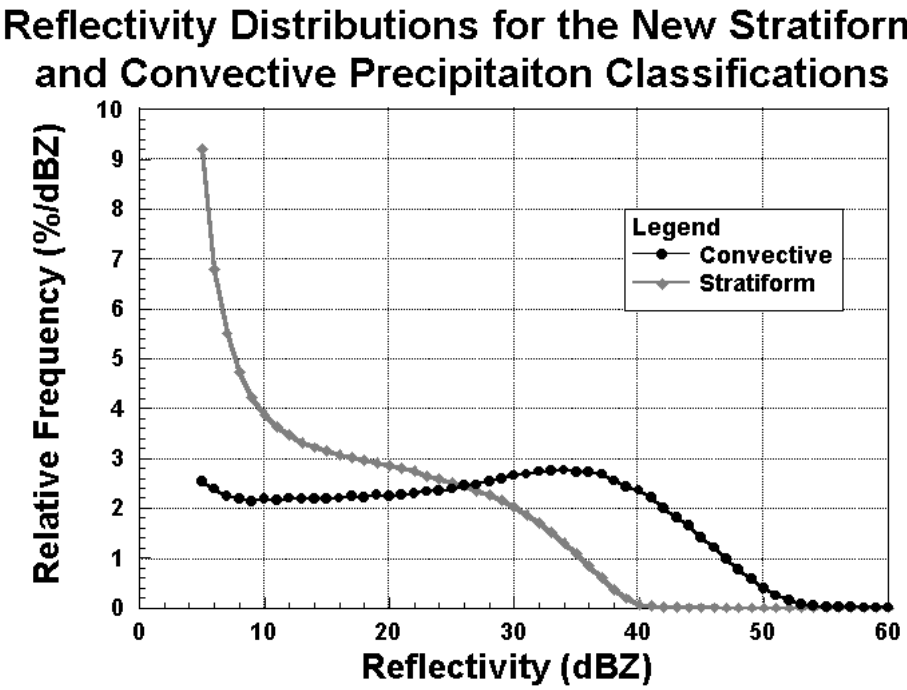

Figure A.10 Distribution of reflectivity at the 2.5 km vertical level for data points classified as stratiform and convective by the partitioning algorithm developed for this study. This figure can be compared to Figs. A.3a-b to determine the new algorithm's performance.

vertical lapse rate $\leq$ -3 dBZ km^{-1}. All points with $Z_h \geq 5$ dBZ that do not receive convective classification are stratiform by default. After the initial classification scheme, a smoothing routine is applied to ensure spatial continuity. The classification of each grid point is tested against the classification of all grid points within a 4 x 4 km window (or, a 3 x 3 grid point box) centered on the grid point under consideration. If the number of grid points sharing the classification of the considered grid point is less than 40%, the grid point is reclassified to match the consensus.

For the sake of comparison and simplicity, a flowchart diagram has been included at the end of this appendix (Figure A.12). The flowchart depicts the procedure of convective classification for the Steiner et al. (1995), Biggerstaff and Listemaa (2000), and newly developed convective partitioning algorithms in a succinct manner. Also included at the end of this chapter is Table

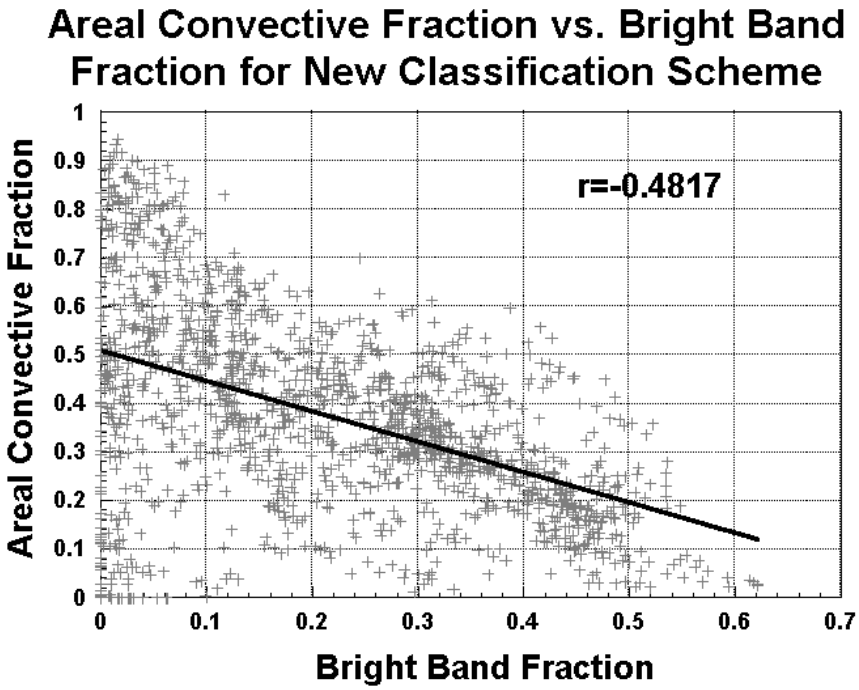

Figure A.11 Correlation between areal convective fraction, as calculated by the partitioning algorithm developed for this study, and the bright band fraction. To indicate good algorithm performance, these two variables should be negatively correlated with each other. This figure can be compared to Fig. A.4 to examine the improvement over the Steiner et al. (1995) partitioning algorithm.

A.1, which compares a list of the constants, thresholds, and methods used in the same three convective partitioning algorithms.

f. The new convective partitioning algorithm: Performance

The performance of the new partitioning algorithm can be determined by the same methods utilized in section A.c. Figure A.9 shows the distribution of the level of maximum reflectivity for the points classified as convective and stratiform by the new algorithm. Fig. A.9 can be compared to Fig. A.2 to examine the improvement of the new algorithm over the Steiner et al. (1995) algorithm. The frequency of convective classification of points with a maximum level of reflectivity in the bright band region, found by integrating the convective curve from 3.5 to 6.5 km, is decreased to only 9%. The frequency distribution of 2.5 km reflectivity is shown in Figure

A.10. Many more points with weak reflectivity are classified as convective as compared to the Steiner et al. (1995) scheme (Fig. A.3a), which indicates that more points on the fringes of convective cells are being included in the convective classification. The resulting reflectivity distribution is much closer to the reference distribution of Fig. A.3b. Finally, the correlation between the areal convective fraction and the BBF of all analyzed radar volumes is shown in Figure A.11. Unlike Fig. A.4, the correlation is robustly negative, which can be attributed to the significant increase of areal convective fraction for many of the radar volumes with low average BBFs. These radar volumes were typically characterized by isolated convective cells, and this result was similar to that of Biggerstaff and Listemaa (2000). Overall, these tests, along with subjective evaluation of the spatial and temporal reliability of the algorithm, would indicate that the new partitioning algorithm is better able to capture the essence of the distinction between stratiform and convective precipitation regimes, and thus is more suitable for use in this study.